

Chapter 1

INTRODUCTION

Inflammation. Acute inflammation describes the primary response of the body to stimuli which it deems harmful and is effected through the amplified movement of plasma and leukocytes (especially granulocytes), normally in the blood, into the wounded tissues⁵. The inflammatory response is propagated and matured through a cascade of biochemical events involving the immune system, the local vascular system, and the various cells within the damaged tissue. However, chronic or prolonged inflammation causes an eventual change in the types of cells present at the location of inflammation and is characterized by concurrent tissue destruction and restoration, resulting in tissue fibrosis⁶. Additionally, in states of chronic inflammation, high levels of circulating immune complexes can accumulate in organs, resulting in additional inflammation and tissue damage.^{7, 8}

Disease-specific targets. Because the etiology of many inflammatory disorders are unknown, broad, non-specific immunosuppressive agents, such as methotrexate, are often used to manage these diseases.⁹ As the mechanisms responsible for disease pathology are discovered, however, disease-specific targets may serve a critical role in treatment. For example, the use of the anti-inflammatory drug propagermanium (3-oxygermylpropionic acid polymer) (**Figure 1.1**) in the treatment of chronic inflammation in hepatitis B patients has illustrated the therapeutic potential of disease-specific

targets^{10,11}. The migration and activation of monocytes, a type of white blood cell and part of the innate immune system of vertebrates, is a key event in the development of chronic inflammation, and the monocyte chemoattractant protein-1 (MCP-1) is essential to the promotion of this state¹². Propagermanium attenuates inflammation through specific inhibition of the *in vitro* chemotactic migration of monocytes by MCP-1¹³. The clinical successes and relatively few adverse effects of propagermanium highlight the potential for increasing therapeutic windows with disease-specific therapeutics¹⁴.

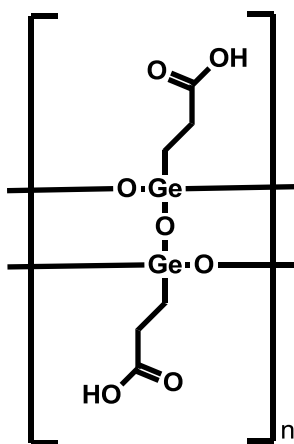


Figure 1.1. Structure of propagermanium (3-oxygermylpropionic acid)¹⁵.

Targeting human protein kinases. Protein kinases comprise one of the most expansive and functionally diverse families of genes and are essential to the regulation of cellular functions. Through transfer of the gamma phosphate of the cosubstrate adenosine triphosphate (ATP) to the hydroxyl acceptor group on the side chains of serine, threonine, or tyrosine residues of their protein substrates, they serve to coordinate nearly every cellular process by directing the activity, localization and general function of numerous proteins^{16,17}, including complex operations, such as signal transduction and the cell cycle. It is evident from the conservation of around 50 distinct

families among yeast, invertebrate, and mammalian kinomes, that protein kinases mediate an array of essential functions. Among the known 518 members of the human kinome, a single superfamily encompasses 478 of these with similar sequences in their catalytic domains. Further distinctions are then made to define groups, families, and sub-families by increasing sequence similarity and biochemical function.

Although these enzymes are critical to normal physiology, several disease states, including cancer, diabetes, and inflammation, have been strongly associated with aberrant regulation of protein kinase activity, leading to an increased interest in their inhibition as a therapeutic strategy¹⁸⁻²². In fact, the potential to control cell proliferation and death through specific inhibition of a target kinase suggests the prospect of targeted therapies in the treatment of inflammatory disorders in which mainly broad, non-specific immunosuppressive agents have previously employed. Kinases have been clinically validated as drug targets by the successes of many small molecule kinase inhibitors such as Iressa and Tarceva (**Figure 1.2**). Specifically, these compounds have been developed to inhibit the epidermal growth factor (EGFR), which is frequently overactive in cancerous cells¹⁶.

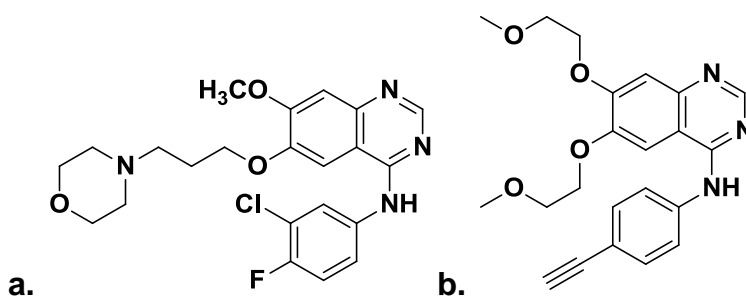


Figure 1.2 The structures of known small molecule kinase inhibitors **a.** Iressa and **b.** Tarceva¹⁶.

Protein kinase structure and function. The discovery of inhibitors of these enzymes has recently been facilitated by the availability of protein crystal structures of nearly 50 different protein kinase catalytic domains. These structures have greatly expanded the comprehension of the catalytic and regulatory functions of this class of enzyme²³. While this information has confirmed the structural conservation of the catalytic core of the protein kinase, it has also illustrated the ways in which these enzymes balance the necessarily high degree of conservation required for catalytic function with need for unique solutions to their individual biological functions. Although it generally follows that sequence conservation points to conservation of spatial structure and function as well, while distinctions consist only of residues, loops, or insertions not conserved in an entire family, exceptions to this rule have been identified²⁴.

The typical protein kinase catalytic domain is bi-lobal, consisting of an amino-terminal lobe and a carboxyl-terminal lobe, connected by a flexible hinge region, with the ATP molecule and a Mg²⁺ ion binding in a deep cleft between the lobes (**Figure 1.3**). The entire ATP molecule is accommodated in this narrow, hydrophobic cleft, with the gamma phosphate oriented toward solvent²⁴. These enzymes are highly flexible so that the binding of substrates, cofactors, auto-inhibitory domains, or interacting proteins during catalysis or regulation stimulates large rotations of the lobes in addition to shifts of flexible loops and domains²⁵⁻²⁷. The active site contains most of the highly conserved residues among kinases as they all must similarly bind ATP for activation.

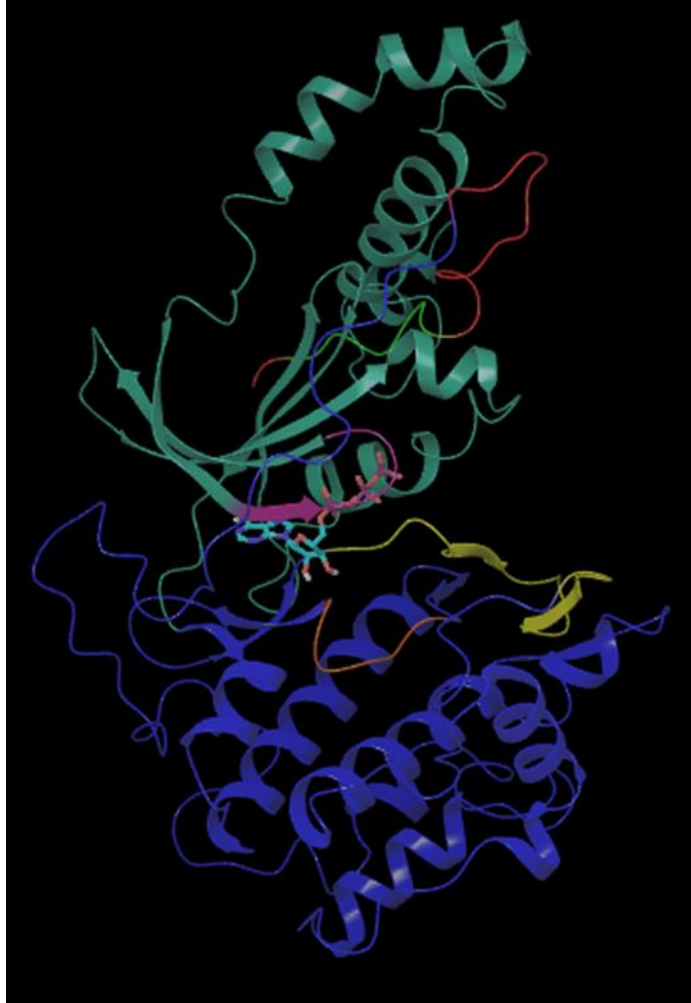


Figure 1.3. Kinase domain of ROCKII (PDB: 2F2U) with ATP modelled into the active site; green: hydrophobic motif (HM), red: carboxy-terminal extension, teal: amino-terminal lobe, blue: carboxy-terminal lobe, purple: P-loop, yellow: A-loop, orange: C-loop.

As shown in **Figure 1.3**, the N-terminal lobe is the smaller of the two conserved lobes, and its structure is dominated by a five stranded antiparallel beta-sheet as well as a long alpha-helix. The first two beta-strands are connected by a turn formed by the central four amino acids of the highly conserved GXGXXGXV motif, known as the glycine-rich loop, the G-loop, or the P-loop^{24,27}. These conserved glycines allow the nucleotide to approach the peptide backbone closely. The larger C-terminal lobe also

contains residues which interact with ATP. Structurally, this lobe harbors seven alpha-helices and four short beta-strands with a central bundle composed of four antiparallel alpha-helices. The beta-strands form the bottom of the cleft beneath the adenosine moiety and also contain the catalytic and metal binding loops. Within the catalytic loop resides a conserved Asp residue, believed to abstract the proton from the hydroxyl group of the substrate amino acid. Additionally, this loop contains a Lys, Arg, or Glu residue which serves to neutralize the negative charge of the gamma phosphate of ATP to stabilize its intermediate state²⁸.

The activation loop of the kinase experiences large structural changes as the enzyme transitions from the inactive conformation to the active conformation and back. This loop contains what is known as the DFG motif since it is comprised of a conserved aspartate (D), phenylalanine (F), and glycine (G) triplet²⁹. In many kinases, the DFG motif adopts the putative “out” conformation in the inactive state of the enzyme, exposing an allosteric site which is obstructed by phenylalanine in the active conformation. The transfer of phosphate from ATP to its substrate is catalyzed by the aspartate residue, causing rotation of the DFG motif such that the active site is revealed and the allosteric site is blocked (**Figures 1.4 and 1.5**)³⁰. Substrate access is often allowed by stabilization of the activation loop in the active conformation through phosphorylation of a residue on this loop.

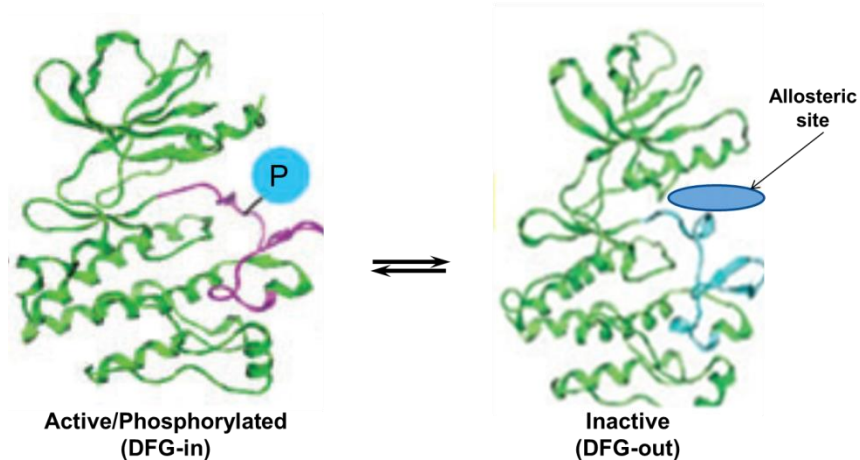


Figure 1.4. The various active and inactive conformations of the activation loop (left=purple, right=blue); P= phosphorylation. Adapted from Liu et al.³⁰.

Type I kinase inhibitors. The initial strategy to develop kinase inhibitors was to mimic the binding interaction of ATP with the kinase. This first generation of small molecule kinase inhibitors, described as type I inhibitors, target the ATP binding site of the enzyme in the active form³⁰. The DFG-out conformation of the DFG motif is therefore not required for these inhibitors to bind (**Figure 1.5**, left). The common feature of the type I inhibitors is the mimicry of ATP in their interactions with the residues of the hinge region²⁵. When an inhibitor scaffold contains functionality that can interact with individual amino acids at the ATP binding site of the target of interest, specificity may be achieved²⁴. The development of inhibitors with selectivity for one kinase of the human kinome has been exceedingly challenging due to the high conservation of their ATP binding sites. Thus, type I inhibitors are often only moderately specific for a unique kinase²⁶. Of course, an optimal inhibitor would possess potent on-target activity while excluding off-target kinases in order to limit the impact of the inhibitor on critical, normal cellular functions^{24,26}.

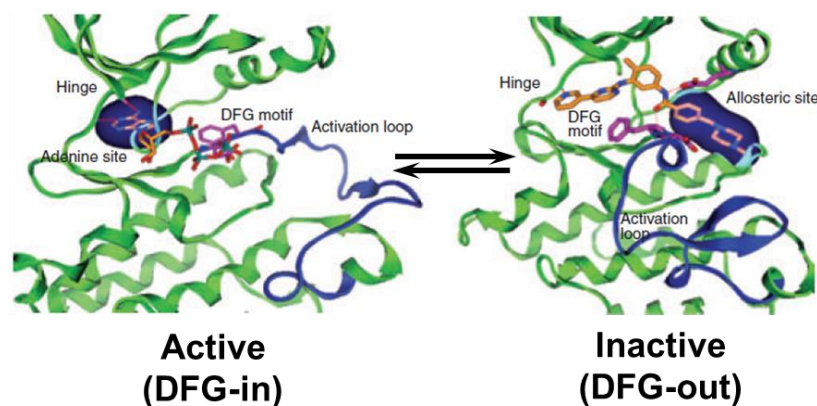


Figure 1.5. A depiction of the active and inactive states of protein kinases. (left) The ATP binding site adopting the DFG-in activation-loop conformation (or active conformation) upon binding of ATP. (right) The ATP binding site adopting the DFG-out activation-loop conformation (or inactive conformation) upon binding of a representative type II inhibitor. Adapted from Liu et al.³⁰.

Type II kinase inhibitors. Although it was not initially designed to do so, the first small molecule kinase inhibitor to reach the market, imatinib or Gleevec, recognized an alternative conformation of a kinase³⁰. Eventually, crystallographic evidence indicated that imatinib, an inhibitor of cKIT, Abl, and PDGFR which is approved for treatment of chronic myeloid leukemia, bound an inactive form of its targets, simultaneously preventing binding of both nucleotide and protein substrates³⁰. The orientation of the DFG motif in the inactive form alters the ATP binding site by exposing the allosteric site. Imatinib and similar inhibitors, classified as type II kinase inhibitors, occupy this additional hydrophobic pocket exposed by this conformation of the activation loop as well as the ATP binding cleft (**Figure 1.5**, right)³¹. Although the novel mode of binding of imatinib was discovered by chance, it inspired the development of a new generation of inhibitors. Examples of other type II inhibitors include BIRB796, the MEK1/2 inhibitor³¹, and sorafenib³², a Raf/MEK/ERK pathway inhibitor.

Type II inhibitors typically consist of two domains known as the head and tail³⁰. The head domain mimics type I inhibitors with functional groups designed to hydrogen bond with the hinge region as well as hydrophobic regions to interact with the ATP binding cleft, while the tail domain includes hydrogen bonding groups and hydrophobic moieties designed to occupy the allosteric site formed by the DFG out conformation³⁰. Additional selectivity is often achieved through binding in the allosteric site since the amino acids surrounding it are less conserved among kinases when compared to the amino acids in the ATP binding pocket. However, the development of type II inhibitors might not be achievable for every kinase since some kinases do not seem to adopt the DFG-out conformation³⁰.

Despite the heightened interest in protein kinases as drug targets, there are currently only 13 ATP-competitive small molecule kinase inhibitors approved by the FDA (**Table 1.1**), which highlights the problems and limitations encountered in the development these compounds. For example, as previously mentioned, due to high conservation of the ATP-binding domain, type I inhibitors are often plagued by poor selectivity among alternate members of the kinase family and thus require intensive optimization campaigns and modifications. Although the potential of type II inhibitors to improve efficacy through selective targeting of unique allosteric sites was initially exciting, it has recently been demonstrated that, through kinase active site amino acid mutations, protein kinases can become insensitive, or resistant, to these small molecule inhibitors³³. One well-characterized example of this is Bcr-abl, the target of Gleevec, which converts a binding site cysteine to a threonine, precluding binding of the inhibitor³⁴. Hence, there remains a need to produce kinase inhibitors which further

explore chemical space in order to circumvent resistance and to selectively target individual kinases.

Table 1.1 FDA-approved ATP-competitive kinase inhibitors^{35,36}.

Inhibitor	Target	Indication
Imatinib	BCR-ABL, PDGFR, and KIT	CML and GIST*
Dasatinib	BCR-ABL	CML
Nilotinib	BCR-ABL	CML
Gefitinib	EGFR	Non-small cell lung cancer
Erlotinib	EGFR	Non-small cell lung cancer and pancreatic cancer
Lapatinib	EGFR and ERBB2	Breast cancer
Sunitinib	VEGFR2, PDGFR, and KIT	Renal cell carcinoma, GIST, pancreatic cancer
Sorafenib	VEGFR2 and PDGFR	Renal cell carcinoma and hepatocellular carcinoma
Pazopanib	VEGFR2, PDGFR, and KIT	Renal cell carcinoma
Crizotinib	ALK/c-MET	Non-small cell lung cancer
Vemurafenib	BRAF	Melanoma
Vandetanib	VEGFR-2, EGFR, RET, and ErB-1	Medullary thyroid cancer
Ruxolitinib	JAK1/JAK2	Myelofibrosis

*CML: chronic myeloid leukemia, GIST: gastrointestinal stromal tumor.

ROCK identification, structure, and regulation. Various aspects of cell shape, motility, proliferation, and apoptosis are regulated by the small GTP-binding Rho family proteins, including Rho, Rac1, and Cdc42³⁷. ROCKs, or Rho-associated coiled-coil containing protein kinases, is the first known downstream effectors of Rho³⁸. Through regulation of myosin light chain (MLC) phosphorylation, ROCKs serve as mediators of

actin cytoskeletal changes induced by RhoA³⁹. ROCKs belong to the serine/threonine (Ser/Thr) family of protein kinases which are most homologous (45-50%) to other actin cytoskeletal kinases, including myotonic dystrophy kinase (DMPK), citron kinase, and myotonic dystrophy-related cdc42-binding kinase (MRCK)^{38,40}. In the mammalian system, two ROCK isoforms have been identified. ROCKI (ROK β or p160ROCK), found on chromosome 18, encodes a protein of 1354 amino acids⁴¹. ROCKII (ROK α or “Rho-kinase”), located on chromosome 12, encodes a 1388-amino acid protein⁴¹. In 1996, an overlay assay utilizing GRP-bound RhoA as a probe for expression screening and a glutathione S-transferase (GST)-bound affinity column first identified ROCKII as a Rho-binding protein^{38,40}. Subsequently, a ligand overlay assay successfully purified ROCKI³⁹.

Rho-kinase consists of an N-terminal extension, a protein kinase domain, a C-terminal extension forming a central coiled-coil region encompassing the Rho binding domain (RBD) at its C terminus, and a C-terminal putative pleckstrin homology (PH) domain which includes a cysteine-rich subdomain (**Figure 1.6**). The coiled-coil region is believed to function by interacting with other alpha-helical proteins while the PH domain participates in protein localization⁴². In the absence of Rho binding, an intramolecular interaction between the kinase domain and the C-terminal PH domain comprises an autoinhibitory mechanism⁴³. The two ROCK isozymes (ROCKI and ROCKII) exhibit 92% sequence identity in their kinase domains and 64% amino acid identity overall⁴⁴. Non-identical residues located specifically in proline-containing regions of the PH domains cause the tertiary structures to differ enough to allow activators to recognize each isoform specifically⁴⁵.

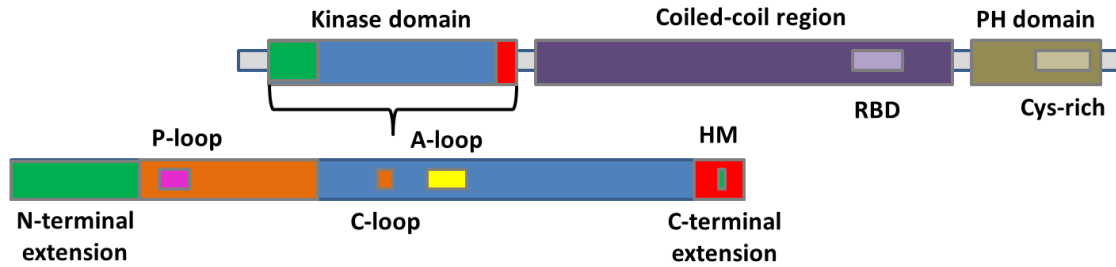


Figure 1.6. ROCK sequence with important regions denoted. Adapted from Yamaguchi et al.⁴⁴.

The N-terminal extension of rho-kinases is required for catalytic activity, as is typical of ACG kinases, and forms an intermolecular helix-bundle fold, known as the capped helix-bundle (CHB) domain⁴⁴. This region functions by bringing two molecules of ROCK together to form a tightly associated head-to-head homodimer (**Figure 1.7**)⁴⁴. It has been observed that the dimerized ROCK kinase domain exists in an active state in the absence of phosphorylation that occurs due to the sandwiching of the C-terminal domain extension between the CHB domain. This causes the “hydrophobic motif,” a conserved sequence of 6 residues (FXXF[T/S][F/Y]) to bind the hydrophobic groove on the kinase domain, thereby stabilizing the active state⁴⁴, allowing the activation loop to adopt an open conformation, permitting nucleotide and substrate binding and subsequent catalysis⁴⁴. Here, X represents any amino acid residue contained within the C-terminal extension.

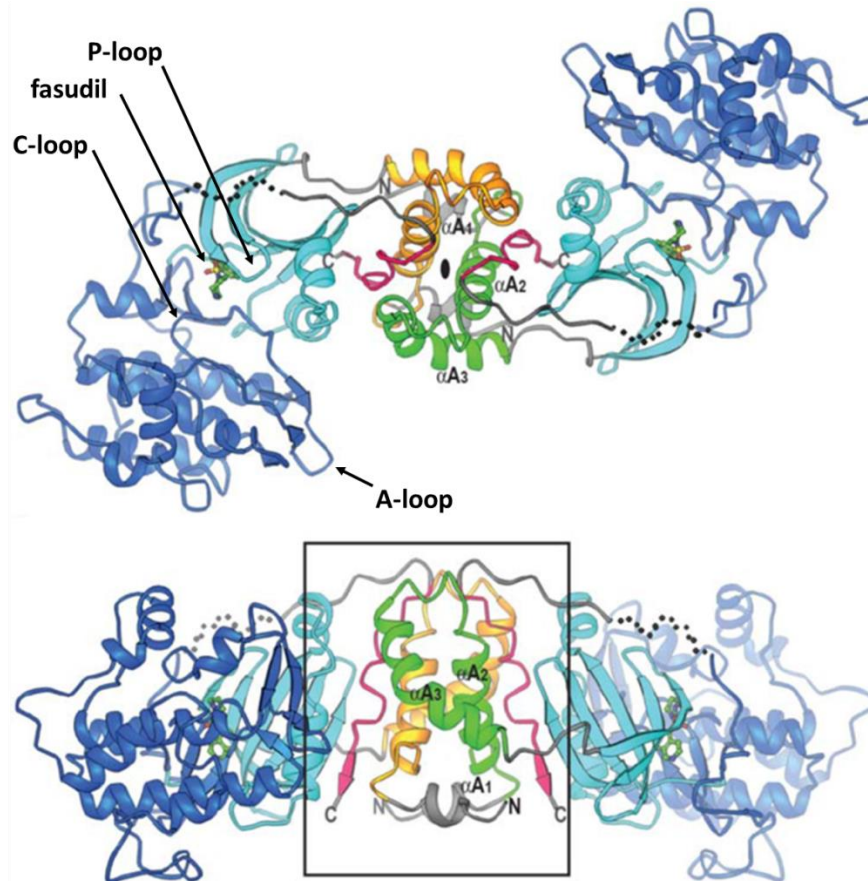


Figure 1.7. The homodimeric structure of the Rho-kinase protein comprised of the kinase domain and the N- and C-terminal extensions. (Top) Looking down the 2-fold axis of the dimer structure. The N-terminal extension is shown in green for one molecule and orange for the other, the kinase domain is shown in cyan for the N-terminal lobe and blue for the C-terminal lobe, and the C-terminal extension is shown in red. Inhibitor molecules are shown as sticks. (Bottom) Looking at the dimer in an orthogonal direction. The N and C termini are denoted. Adapted from Yamaguchi et al.⁴⁴.

As referenced above, the activation loop is crucial in catalysis and defines the disposition of the DFG motif. Rho-kinase undergoes autophosphorylation and thus has a conserved threonine (Thr249) at the central phosphorylation position of its activation loop for this purpose^{46,47}. However, crystals of dimerized ROCK constructs have shown that even in the absence of Thr249 phosphorylation, the activation loop is moved away from the catalytic center in an open and extended conformation permissive to nucleotide

and substrate binding. This observation suggests that ROCK may be incapable of adopting an inactive, DFG-out conformation amenable to inhibition by a type II inhibitor. This hypothesis is supported by the well-documented observations that the closely related kinases protein kinase C (PKC) and cyclin dependent kinase (CDK) are incapable of assuming the DFG-out conformation³⁰. It should be noted, however, that truncated mutants of ROCK, lacking the autoinhibitory carboxy-terminal region, have been observed to be constitutively active. Therefore, it is not surprising that constructs lacking this region adopt active and open conformations, in the absence of phosphorylation. Thus, the conformations observed in the crystal structures of such constructs may not accurately represent the conformations of full-length proteins. To date, there is no crystallographic data for full length ROCK proteins. Therefore, it is unknown whether the development of a type II inhibitor of ROCK may even be possible, but at least without the aid of crystallographic data of an inactive state, it will certainly prove difficult.

As referenced previously, the amino-terminal kinase domain of ROCK is inhibited by the autoregulatory carboxy-terminal region which folds back onto the kinase domain and maintains the enzyme in an inactive state⁴⁸. Binding of the active GTP-bound form of Rho to the RBD of ROCK disrupts this negative regulatory interaction, resulting in an active kinase domain⁴⁸. This conformation might also be effected through the binding of arachidonic acid (AA) or sphingosylphosphorylcholine to the PH domain or by cleavage of the carboxyl-terminus by caspase-3, in the case of ROCKI, or by granzyme B or caspase-2, for ROCKII (**Figure 1.8**). As mentioned, cleavage of the carboxy-terminal region also results in an activated enzyme⁴⁹⁻⁵³. The observed closed-to-open

conformation of Rho kinase activation is comparable to the activation of DMPK and MRCK and agrees with the results of experiments in which several full-length ROCKs with defective kinase domains or constructs of the carboxyl-terminus of ROCK functioned as dominant-negative mutants of ROCK kinase activity⁵⁴⁻⁵⁸. In addition to these regulators, ROCKs are also capable of activation through amino-terminal transphosphorylation^{55,59}.

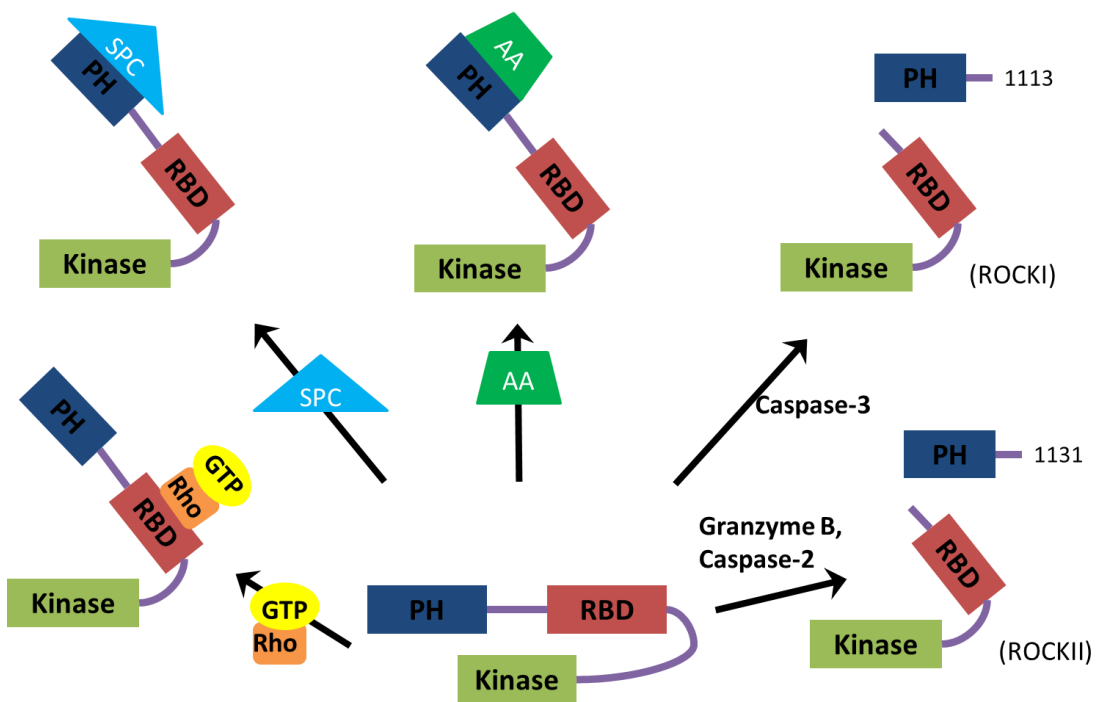


Figure 1.8. Activation mechanisms of ROCK. Adapted from Francis⁶⁰.

Rho kinases may also be inhibited by small GTP-binding proteins^{61,62}. For example, RhoE inhibits ROCKI by interacting with the N-terminal region and preventing Rho from binding to the RBD^{61,63}. Gem and Rad, other small proteins which similarly

bind GTP, also negatively regulate ROCK activity, as well as other enzymes, including Rad, Raf-1, p21(Cip1/WAF1), and aurora-A/serine/threonine kinase 15 (STK15)⁶⁴⁻⁶⁶. It is believed that these inhibitors are involved in actinomyosin contractility regulation, though these mechanisms are yet to be defined⁶⁵. This collection of ROCK regulators which can be activated through GTP binding, phosphorylation, or protein binding, comprise a localized signal-responsive mechanism for ROCK-mediated assembly and contraction of the actin cytoskeleton, a necessary function for cellular polarization, motility, contraction, and adhesion⁶⁷⁻⁶⁹.

Downstream targets of ROCK. Cellular responses mediated by ROCK begin with the activation of Rho by a signaling molecule such as lysophosphatidic acid (LPA) or sphingosine-1 phosphate (S1P). These signals stimulate the Rho guanine nucleotide exchange factor (GEF) and promote the formation of active GTP-bound Rho. ROCK is then stimulated to affect an array of cellular processes, especially those of the actin cytoskeleton³⁹. Specifically, through phosphorylation of a range of different proteins, such as LIM kinases, myosin light chain (MLC) phosphatase, adducin, and ezrin-radixin-moesin (ERM) proteins, ROCKs mediate actin cytoskeleton assembly and cell contractility. However, these proteins may also be phosphorylated by alternate serine/threonine kinases, including protein kinase C, protein kinase A, and G-kinase^{70,71}. ROCK substrates contain one of two consensus sequences: R/KXS/T or R/KXXS/T (R: arginine; K: lysine; S: serine; T: threonine)⁷²⁻⁷⁵. Additionally, the function of ROCKs may be modulated through auto-phosphorylation^{56,76}.

ROCK cellular functions. Presently, over 20 substrates of ROCK have been identified (**Figure 1.9**)⁷⁷. By phosphorylating several downstream effectors including

serine/threonine LIM kinases (LIMKs), ezrin, radixin, moesin, adducin, the myosin light chain (MLC), intermediate filament proteins such as glial fibrillary acidic protein (GFAP), vimentin, and neurofilaments, ROCKs serve to regulate every phase of cellular migration by influencing critical processes such as actin polymerization, focal adhesion formation, and cellular contractility. ROCK also functions as an important mediator of the initiation and execution phases of apoptotic events; here, regulated by a caspase or granzyme B, ROCK controls both the extrinsic and intrinsic apoptotic pathways through manipulations of the cytoskeleton. This is accomplished through activation of proteins such as MLC to drive processes including the formation of membrane blebs containing the nuclear disintegration of DNA. ROCKs have also been shown to control the expression of cell surface markers which target apoptotic bodies for phagocytosis⁶⁰.

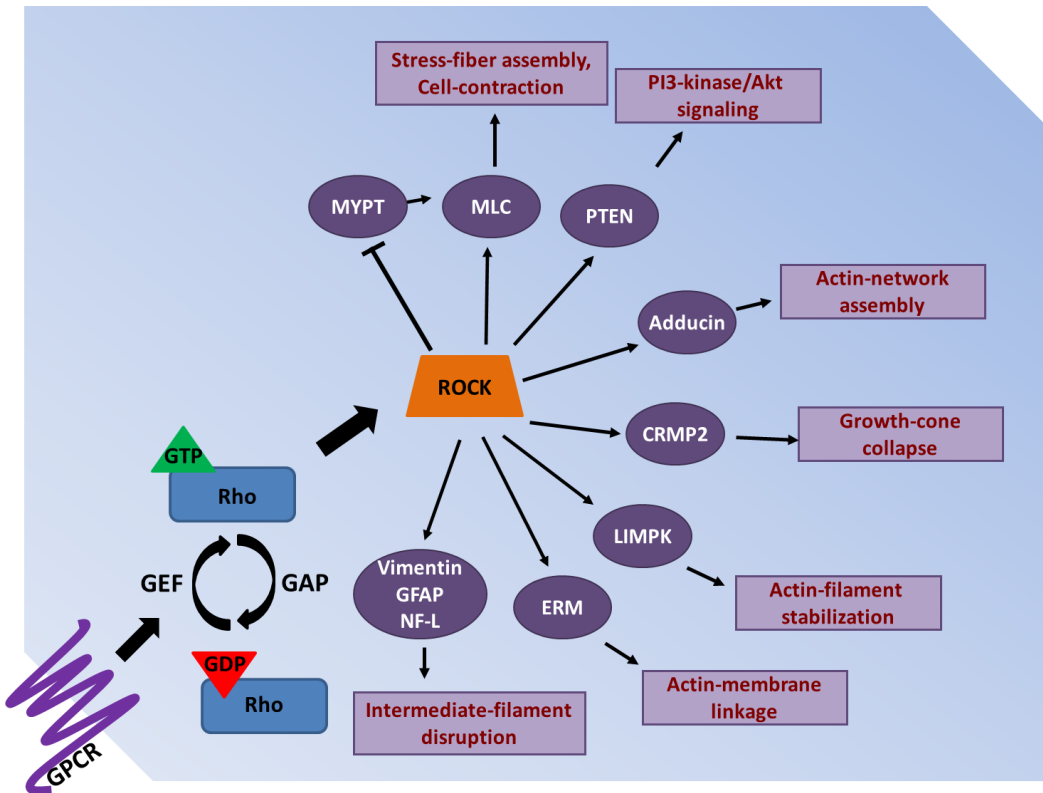


Figure 1.9. A depiction of the various substrates of ROCK phosphorylated after activation of ROCK by GTP-bound Rho⁶⁰.

Role of ROCK/II in inflammation. Multiple studies have observed increases in ROCK activity during the initiation of the inflammatory response and attenuation of inflammation by ROCK inhibitors⁷⁸⁻⁸¹. For example, ROCK phosphorylates IκB kinase (IKK) resulting in the activation of NF-κB. NF-κB then migrates to the nucleus where it initiates the production of cytokines such as IL-1, IL-6, and TNFα by macrophages. The resultant cytokine gradient recruits leukocytes, which must transverse the endothelial barrier from microvessels to the site of inflammation. ROCK has been observed to be activated at inflammatory arteriosclerotic lesions in human, and through inhibition of NF-κB activation, ROCK inhibition has been shown to significantly limit early atherosclerotic

plaque formation in apolipoprotein E-knockout (apoE-KO) mice and low-density lipoprotein receptor knockout (LDLR-KO) mice⁸².

Through phosphorylation of MLC, ROCK also affects the contraction of endothelial cells, enhancing the permeability of the endothelial barrier and allowing transmigration of the leukocytes⁷⁸. Y-27632, a highly selective inhibitor of ROCKs both *in vitro* and *in vivo*, has been observed to prevent human neutrophil migration in response to chemoattractants through suppression of MLC phosphorylation *in vitro*, reestablishing the integrity of the endothelial barrier⁷⁹. Furthermore, the treatment of rats with Y-27632 after implantation of tumor into the peritoneal cavities reduced the rates of dissemination *in vivo*⁷⁹.

Inhibitors of ROCKI/II. Perhaps the most well-known examples of these are the type I inhibitors, notably Y-27632 and Fasudil, which were originally discovered in a high throughput, small molecule screen for inhibition of vasodilatory activity. Neither of these inhibitors is capable of distinguishing between the ROCK isoforms, thus, they are both equipotent in terms of their inhibition.

Fasudil, also known as HA-1077 and AT877, is based on the isoquinoline scaffold and inhibits both ROCK isoforms with an IC₅₀ of 300 nM⁸³. Crystallographic data has shown that Fasudil binds ROCK at the ATP binding site in two distinct modes (**Figure 1.10**). In each, Fasudil occupies the space normally filled by adenine with its isoquinoline ring which binds to the hinge region of ROCK by accepting a hydrogen bond from the amide nitrogen of Met156 (ROCKI) or Met172 (ROCKII), while the homopiperazine ring resides at the cleft entrance⁸⁴⁻⁸⁶. The binding modes differ in that,

in one mode, the homopiperazine ring forms a pair of polar interactions with the side chains of an Asn and an Asp residue, while in the other mode, two bond rotations about the central sulfur atom of the sulfonyl group shift the homopiperazine such that it then forms hydrogen bonds with functionality of alternative residues, specifically the side chain carboxylate of an Asp and the main chain carboxylate of an Asp residue⁴⁴. In 1995, Fasudil was marketed in Japan for the treatment of cerebral vasospasms. Even with its use in over 125,000 patients to date, only minimal side effects have been reported. These data are especially interesting since ROCK is ubiquitously expressed⁵³.

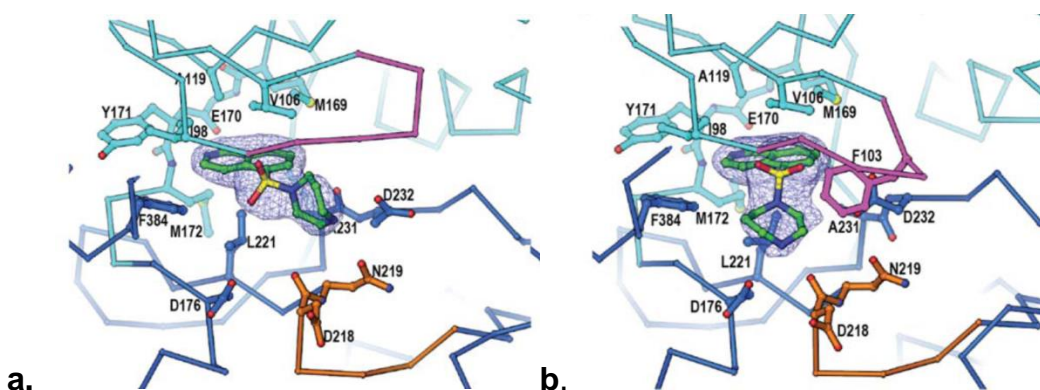


Figure 1.10. The nucleotide binding pockets of Rho-kinase molecules (a) A and (b) B, showing the residues that interact with Fasudil.

Y-27632 is an inhibitor based on an aminopyridine scaffold and is found to affect smooth muscle contraction through binding of ROCKI and ROCKII with a K_i of 220 nM^{53,87}. While crystallographic data shows that Y-27632 adopts a similar binding mode to that of Fasudil, Y-27632 also experiences additional interactions including a critical water bridge between its amide carbonyl and the nitrogen of the main chain of Asp216 as well as interactions between the amine of Y-27632 and the Asn203 and Asp216 side

chains⁸⁶. Efforts to optimize this inhibitor, by substituting the pyridine ring of Y-27632 with a pyrrolo-pyridine moiety which forms an additional interaction with the hinge region of ROCK by donating a hydrogen bond to Glu154 (ROCKI) or Glu170 (ROCKII) (**Figure 1.11**), lead to the development of Y-39983 ($K_i = 50$ nM).

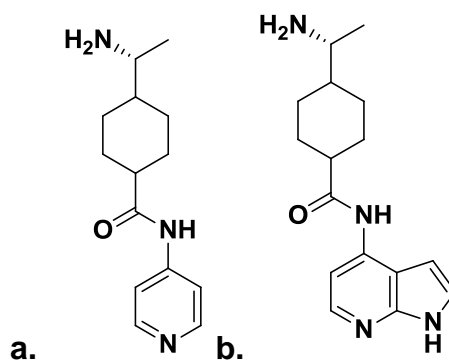


Figure 1.11. Molecular structures of (a) Y-27632 and (b) Y-39983⁹⁰.

Several aminofurazan inhibitors of the kinase domain of recombinant ROCKI were also identified from a high-throughput screen of the GlaxoSmithKline compound collection (**Figure 1.12, c**). The inhibitors SB-772077 and GSK-269962-A were identified through optimization of this series. It has been hypothesized, by Doe et al., that the aminofurazan functionality resides in the adenine binding site where it interacts with hinge region residues, however the crystal structures of these compounds with the enzyme have not yet been solved⁸⁷. These inhibitors are presently being optimized as therapeutics in inflammatory diseases and hypertension⁸⁷.

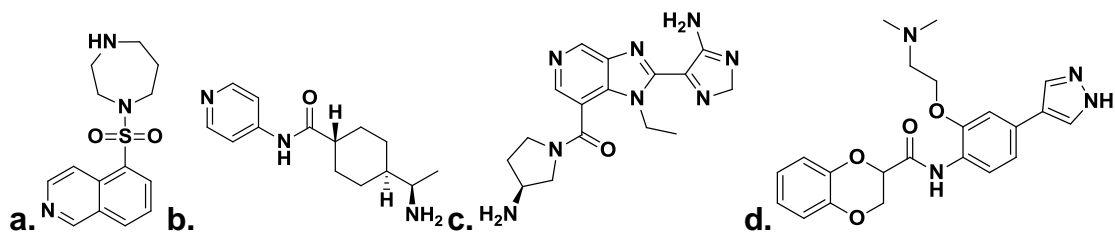


Figure 1.12. The prototypical members of each chemical class of ROCK inhibitors⁶⁰. **a.** Isoquinoline series (Fasudil). **b.** Aminopyridine/Pyrrolopyridine series (Y-27632). **c.** Aminofurazan series (SB-772077). **d.** Amide/Urea series (SR3677).

Due to their drug-likenesses, amides and ureas also serve as the pharmacophores of several inhibitors (**Figure 1.12, d**)³⁹. Notable members of this series include SR3677 and RhoKinase Inhibitor II, a commercially available inhibitor⁹¹. Similarly to the pyrazole functionality of Y-27632, these inhibitors harbor the critical hydrogen-bond donor/acceptor groups which interact with the hinge region. Additionally, molecular modeling studies suggest a critical hydrogen bond is formed between the carboxylate side chain of a nearby aspartate residue and the protonated primary amine of the inhibitor, although the crystal structure is not yet available. This interaction is predicted by Feng et al. to be responsible for the demonstrated ten-fold ROCK inhibition increase when compared to an identical compound lacking this functionality⁹¹.

All known inhibitors are believed to interact with the hinge region residues of the ROCK isoforms, indicating critical ligand-ROCK interactions that account for their observed affinities⁹¹. Firstly, inhibition of ROCKI/II is primarily driven by hydrogen-donor and acceptor bonds between the hinge region and the ligand. A heterocyclic ring is often incorporated for this hydrogen bonding functionality as well as for its ATP binding

site complementarity. Alternative interactions, such as hydrogen bonding between the main chain amide nitrogen and the carboxylate side chain of a proximal aspartate residue, have been suggested to enhance ROCKI/II binding. Taken together, these results combined with computational studies may be used in the optimization of new inhibitors of ROCK.

Inhibitor selectivity among the human kinome. The development of inhibitors selective for ROCK over other kinases has been challenging due to the ATP-binding site homology among kinases and the lack of an observed and reported inactive ROCK state for the development of a type II inhibitor. Due to the latter, all current ROCK inhibitors bind at the ATP-binding site and compete with cellular ATP, making them type I inhibitors⁵³. Although the ability to develop a type II inhibitor is typically advantageous, since several selectivity profiles have shown that type II inhibitors are typically less promiscuous than type I, there have been examples of exceptionally specific type I inhibitors⁹²⁻⁹⁸. The inhibitor of p38 α mitogen-activated protein kinase (p38 α), VX-745, and the inhibitor of epidermal growth factor (EGFR), CI-1033, are both highly selective type I kinase inhibitors and, in fact, both have entered into clinical development⁹⁷. Therefore, despite the highly conserved ATP binding site, such successes demonstrate the feasibility of optimizing type I kinase inhibitors for selectivity.

Recently, Huang et al. conducted a network analysis to assess the selectivity potential of individual kinases of the human kinome⁹⁸. Rather than determining similarity over the entire kinase, they compared specific residues of the ATP binding site. Once the residues of this binding cleft were determined, the available literature referencing the development of selective type I inhibitors was used to determine

important residues (**Figure 1.13**). A 9-bit fingerprint, based on the size of the gatekeeper residue and the resultant accessibility of the hydrophobic pocket, hydrogen bonding ability of the gatekeeper, possible covalent bonds with cysteine side chains, hydrogen bonding ability at specific positions, the intrinsic flexibility of the hinge loop, and the size of the adenine pocket, was then used to encode these residues (**Figure 1.14**). Finally, the resultant fingerprints were used to analyze the network.

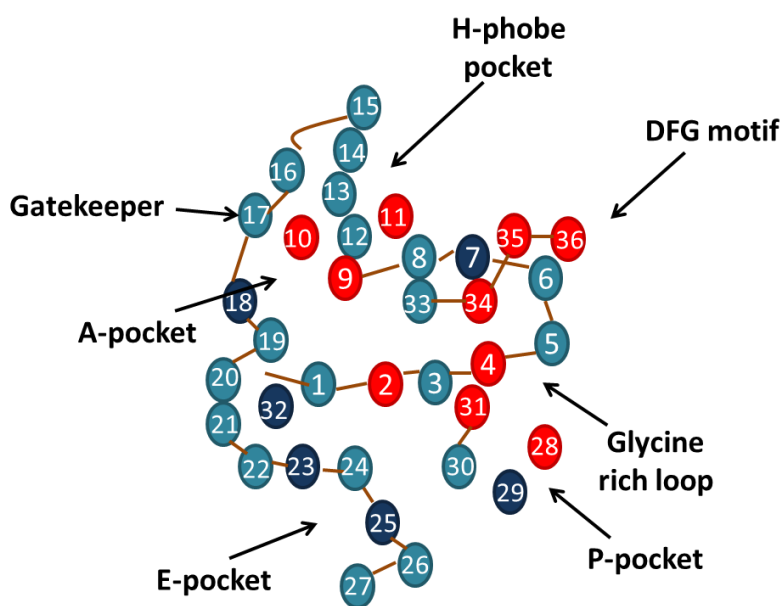


Figure 1.13. A representation of a kinase ATP binding site with residues numbered 1 to 36 according to their occurrence along the sequence. Red circles are most conserved (>90%), blue circles are moderately conserved (70-90%), and cyan circles are not conserved (<70%). Adapted from Huang et al.⁹⁸.

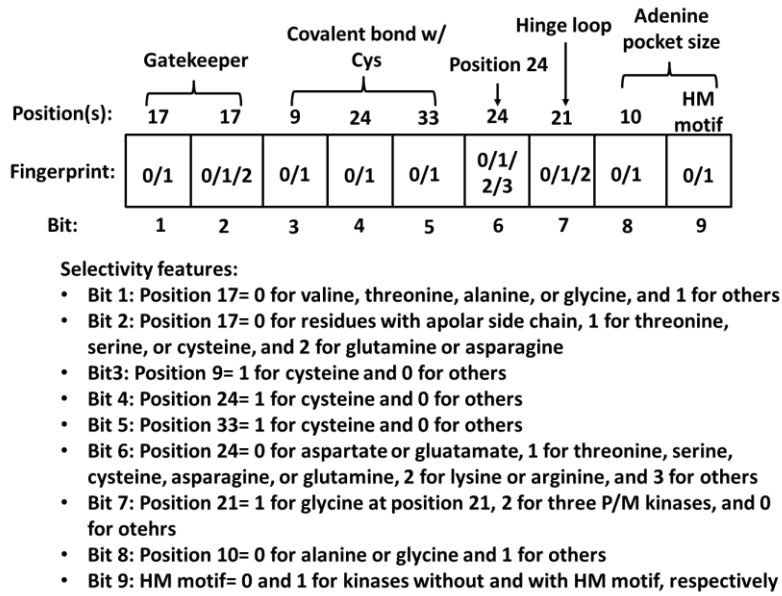


Figure 1.14. 9-bit fingerprint selectivity features. Each bit represents a strategy and is assigned an integer value. Adapted from Huang et al.⁹⁸.

Figure 1.15 represents the network of kinase selectivity potential of the human kinome. As shown, these kinases are divided into sets A (triangles) and B (circles), with set A kinases having large gatekeeper residues while the gatekeeper residues of set B are small.

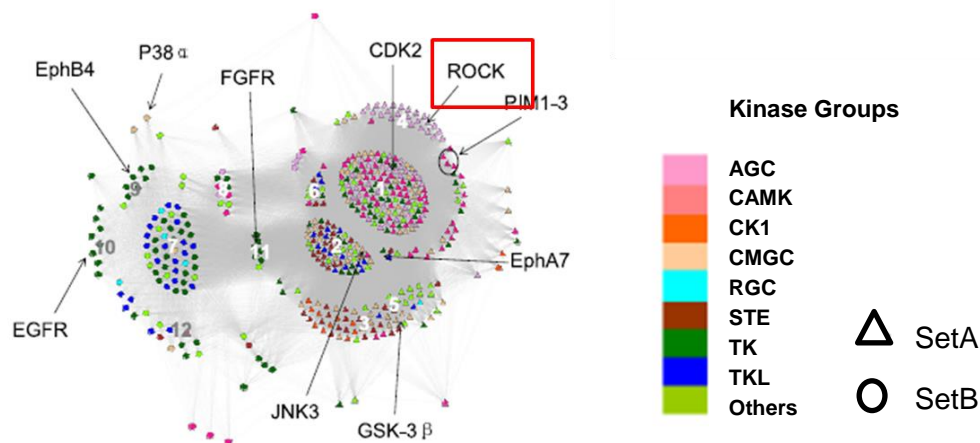


Figure 1.15. The kinase selectivity potential network. Set A represents kinases with bulky gatekeeper residues; B represents those with small gatekeeper residues. ROCK is boxed in red. Adapted from Huang et al.⁹⁸.

With methionine as the gatekeeper of the Rho kinases, it is a member of set A. Other specific attributes then result in the inclusion of the ROCKs in cluster 4 of the network. Kinases in small clusters with few links tend to have a greater potential for development of specific inhibitors, and the occurrence of the ROCKs in cluster 4, which contains only 25 kinases, suggests that the potential for a selective inhibitor is high. This result is mainly due to bit 9, which assesses the existence of a hydrophobic motif (HM) within the adenine binding pocket. Specifically, a carboxy-terminal chain folds back into the amino-terminal lobe, across the catalytic cleft, positioning a phenylalanine residue (Phe368 in ROCKI; Phe384 in ROCKII) on one side of the adenine binding pocket (**Figure 1.16**)²⁴. This residue significantly contributes to the contact between the protein and the ATP molecule, and is a distinguishing characteristic of the AGC subfamily to which ROCKs belong. Therefore, although only moderate selectivity has been achieved to date, these results suggest that the potential to develop a specific inhibitor is great and worth pursuit.

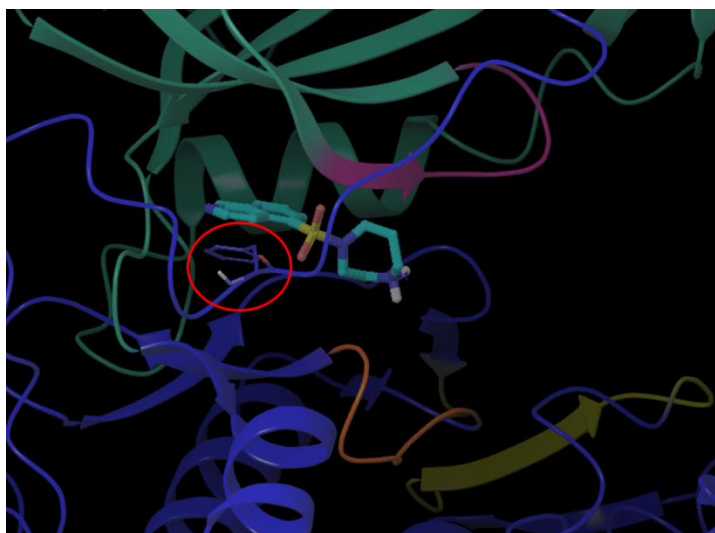


Figure 1.16. Fasudil bound into the ATP binding cleft of ROCKII (PDB: 2F2U). Phe384 is circled.

Y-27632 and Fasudil have been observed to inhibit additional kinases besides ROCK with equal potency, including protein kinase N (PKN, or PRK2). Additionally, both are observed to inhibit mitogen-and stress-induced kinase 1 (MSK1), mitogen-activated protein kinase 1b (MAPKAPK1b), and phosphorylase kinase (PHK) with reduced effectiveness⁹⁹. At present, SR3677 remains the most selective ROCK inhibitor known, acting on only five alternate kinases (Akt, Clk1, Clk2, Clk4, and Lats2) at over 50% inhibition in a profiling screen of 353 kinases⁹¹. Although the clinical validation of Fasudil has demonstrated that its promiscuity is tolerable, the development of inhibitors specific for ROCK is important to avoid off-target binding and to improve efficacy.

ROCK isoform distinctions. In many cases, the biological functions of ROCKI and ROCKII isoforms cannot be separated, likely as a result of the high degree of homology within the kinase domain (92%) of the isoforms and the redundancy in their pathways¹⁰⁰⁻¹⁰³. However, recent evidence has shown that differential expression levels of the ROCK isoforms (ROCKII is highly expressed in the brain and weakly expressed in the lung, while ROCKI is highly expressed in the heart, lung, skeletal muscle, kidney, and pancreas, moderately expressed in the placenta and liver, and very weakly expressed in the brain) and distinct interaction partners in individual tissue types point to a potential therapeutic benefit of selectively inhibiting a unique isoform, thereby improving the efficacy of ROCK inhibitors^{104,105}. Furthermore isoform-specific inhibitors are necessary for validation and further research of cellular ROCKI/II functionality.

Recently, insights into the biology of the ROCK isoforms have been provided by genetic studies, animal disease models, and short interfering RNA (siRNA)-based gene

silencing experiments *in vitro*. Specifically, fibroblasts and vascular smooth muscle cells have shown that ROCKI and ROCKII perform distinct non-redundant functions¹⁰³. In particular, while disassembly of stress fibers in fibroblasts is effected by knockdown of ROCKI but not ROCKII, the same phenotype is mediated by knockdown of only ROCKII in smooth muscle cells^{103,106}. Additionally, only ROCKI is regulated by RhoE or cleaved, and thus activated, by caspase-3 at a conserved sequence in the carboxy-terminal region, which is absent in ROCKII¹⁰⁷⁻¹¹¹. However, granzyme B specifically cleaves and activates ROCKII during granzyme B-induced cell death¹¹². Furthermore, inositol phospholipids, such as PtdIns3,4,5,P3 and PtdIns4,5,P2, selectively activate ROCKII through interaction with the PH domain, suggesting a unique role for ROCKII in signaling events in the phospholipid pathway^{39,49,113,114}.

Aside from upstream modulators, ROCKI and ROCKII also utilize specific downstream effectors to perform their biological functions. For example, the induction of mesoderm is regulated by the degradation of transforming growth factor β type I receptor, which is specifically induced by ROCKII¹¹⁵. Although both isoforms modulate MYPT1 activity in vascular smooth muscle cells, their effects on smooth muscle cell morphology differ. ROCKII alone directly binds and phosphorylates MYPT1, while UV-induced stress stimulates ROCKI to activate c-Jun N-terminal kinase (JNK) and to bind and phosphorylate JNK-interacting protein 3 (JIP-3), thus inducing apoptosis^{106,116}. Additionally, the ROCKI-LIMK2 interaction specifically modulates cell spreading of breast cancer cells during the mesenchymal-mode of 3D-migration¹¹⁷.

Role of ROCK isoforms in disease. Pathological conditions have also identified the significance of the ROCK isoforms in function and regulation. For example,

pressure overload cardiac hypertrophy in mice, induced by aortic banding, has shown that after 3 weeks in a state of stable hypertrophy, levels of ROCKI expression are increased and ERM phosphorylation was observed. However, no alteration of ROCKII expression levels were detected. Cardiac hypertrophy was not affected by disruption of ROCKI, but in ROCKI^{-/-} and ROCKI^{+/-} mice, a significant reduction in the development of fibrosis in the myocardium was observed^{118,107}.

Distinct contributions have also been identified for the ROCK isoforms in cancer. ROCKII levels have been reported to be increased in colon, hepatocellular, and bladder cancers, and short-hairpin RNA reduces lung metastasis by silencing ROCKII¹⁰⁸⁻¹¹⁰. High expression levels of ROCKI occur in human mammary tumors and are predictive of poor clinical outcomes and patient survival rates¹¹¹. The transformation of hormone-refractory prostate cancer has also recently been associated with elevated levels of ROCKI¹¹⁹. In such cases, progression of disease may either be caused by the result of overexpression of a ROCK isoform or it may in fact be the cause.

In another study of the pathological distinctions between the isoforms, ROCKII specific substrates in the brain were probed to understand the differences in expression of the isoforms, and a unique phosphorylation of the collapsing response mediator protein-2 (CRMP2) by ROCKII was observed. Disregulation of the phosphorylation of CRMP2, a neuronal protein involved in lysophosphatidic acid (LPA)-induced growth cone collapse in axon growth, plays a role in neural progression disorders¹²⁰. This observation implicates ROCKII in the abnormal neurological condition progression, and confirms that distinct physiological roles exist for the ROCK isozymes¹²¹.

The observation of a specific substrate of ROCKII in neural tissue motivated the use of small interfering RNA (siRNA) to reduce the expression of each of the isoforms of ROCK in different types of tissues. From this, a number of isoform-specific functions have been identified *in vitro*⁴⁵. For example, Yoneda et al. reportedly observed distinct cellular morphologies upon selective ROCKI or ROCKII reduction⁸⁸. When ROCKI was reduced in embryonic fibroblast cells, long thin processes were extended from cells, while small disc-like extensions were induced upon reduction of ROCKII^{45,88}. Additionally, ROCKII-depleted cells displayed strongly down-regulated phagocytic function in comparison to ROCKI-depleted cells as a result of these morphological changes⁴⁵. It is suspected that this is due to the lipid-binding preferences of the PH domains of the ROCK isoforms, specifically only ROCKII binds PtdIns3,4,5P, since phosphoinositol signaling initiates phagocytic function⁴⁵. Together, these results imply that actin dynamics are regulated by ROCKI and ROCKII through the coordination of distinct signaling pathways under specific cellular conditions.

Isoform knockout mice. To further study the role of the isoforms of ROCK in disease, ROCKI (ROCKI^{-/-}) and ROCKII (ROCKII^{-/-}) knockout mice have been generated^{122,123}. Births of the ROCKI (ROCKI^{-/-}) knockout mice are observed in the expected Mendelian ratios, however, births of ROCKII (ROCKII^{-/-}) knockout mice are sub-Mendelian since 90% experienced placental dysfunction and subsequently died *in utero*^{123,124}. Reduced blood flow caused by problems in the placental labyrinth layer as well as intrauterine growth retardation stemming from the formation of a thrombus in the labyrinth layer of the placenta resulted in this observed embryonic lethality of ROCKII^{-/-} mice¹²³. Both ROCKI and ROCKII knockout mice experienced eyes open at birth (EOB)

and omphalocele, a failure to close the wall of the ventral body during ontogenetic development, leading to the protrusion of intestinal organs¹²³. Those ROCKII knockout mice which survive the above intrauterine and prenatal problems, however, appear to develop normally into healthy, fertile adults showing no bodily or functional abnormalities, as is seen in the ROCKI knockout mice^{122,123,125,126}. These results show that ROCKII knockout mice do not experience a compensatory up-regulation of ROCKI expression, implying each isoform has an independent cellular function.

The contributions of ROCKI to pathological conditions have also been studied in ROCK knockout mice. For example, it has been observed that partial or full deletion of ROCKI served to reduce cardiac fibrosis in models of chronic high blood pressure, while cardiomyocyte hypertrophy remained unaffected^{125,126}. Cardiomyocyte apoptosis, an important contributor to the progression of heart failure, has also proven to be dependent on ROCKI through ROCKI knockout studies¹²⁵. Together, these studies indicate that the pathophysiological responses to high blood pressure require ROCKI and support the targeting of ROCK in the development of therapeutics of specific cardiovascular diseases^{125,127}. In another example, ROCKI deletion has been shown to be insufficient, in preventing renal fibrosis in a ureteral obstruction model¹²⁸. This result may suggest compensatory action by ROCKII or that, in this specific tissue, ROCKII is dominant¹²⁸. In further studies, altered spine length and deficits in basal synaptic function were observed in ROCKII knockout mice, indicating a critical role for ROCKII in neurological function and normal brain anatomy¹²¹.

Isoform selectivity of ROCK inhibitors. Even with this increasing evidence of distinct ROCK isoform function in normal and pathological conditions, isoform selectivity

is rarely addressed in recent ROCK inhibitor patents¹²⁹⁻¹³². For example, all publicly accessible ROCK inhibitors before 2008 were equipotent against both ROCK isoforms. Although SR3677 has shown some selectivity for ROCKII over ROCKI (20-fold), the most isoform selective inhibitor identified to date is SLx-2119 (ROCKI $K_i = >10 \mu\text{M}$, ROCKII $K_i = 100 \text{ nM}$), an inhibitor in development as a therapeutic for liver fibrosis and steatosis⁶⁰. An isoform-selective inhibitor is expected to enhance efficacy, due to several factors including differing tissue expression levels of the isoforms, different cellular substrates of each isoform, a lack of compensation of one isoform for the other, and differences in the subcellular localization of the ROCKs. In support of this hypothesis, in apolipoprotein-E-deficient mice, SLx-2119 has also been reported to attenuate arterial plaque formation while avoiding hemodynamic side effects known to be problematic with non-selective ROCK inhibitors¹³³.

Biochemical versus cell-based assays. A primary goal in this research is to discover the molecular attributes of the BZD inhibitor series that confer potency as well as isoform selectivity. Although many biochemical assays have been developed to measure the effects of compounds on ROCKI and ROCKII, they generally utilize constructs of the ROCK enzymes which primarily represent their kinase domains (residues 1-543), rather than the full length proteins (>1300 amino acids). As detailed above, the domains contained in the C-termini of ROCKs serve to regulate the activity of the enzyme through autoinhibition and mediator recognition. Because all known cellular isoform-selectivity is effected through interaction with the C-terminus of ROCK, the absence of these regions in the biochemical assays may result in an inaccurate

representation of the selectivity of an inhibitor. These concerns highlight the need for cell-based ROCK assays incorporating native, full-length enzymes.

Although the development of a ROCK inhibitor which targets the ATP-binding domain of a single isoform in the biochemical assay would nearly guarantee a translation to selectivity among the ROCK enzymes in the cellular environment, the cellular machinery (regulators, etc.) has clearly demonstrated that the regions of ROCK which possess the greatest potential for isoform-selective regulation lie far outside the kinase domain, in the C-terminus. This implies that developing an inhibitor which is specific for the kinase domain of one ROCK isoform may be unnecessarily difficult. It may in fact be advantageous to target regions of the C-terminus which are capable of being selectively recognized by effectors and mediators of ROCK instead. This may be accomplished through either direct binding of these regions or through a conformational change which affects these domains, elicited by the binding of an inhibitor to the kinase domain. In either case, rational design of such inhibitors is hindered by the lack of crystallographic data of full length proteins.

Preliminary studies. **BZD-29** was originally discovered by Glick et al. during lead optimization of a series of inhibitors of the mitochondrial F_1F_0 -ATPase. Instead of inhibiting this target, however, **BZD-29** was found to be a potent and selective inhibitor of ROCKII in cells, and to effectively attenuate disease in the *Shistosoma mansoni* mouse model of chronic pulmonary inflammation, without evoking general toxicity. Furthermore, the IgG IC model of acute inflammation elucidated multiple non-redundant mechanisms of action by which **BZD-29** reduces inflammation in the *S. mansoni* model, including inhibition of neutrophil migration, reduction of cytokine and chemokine levels

released from macrophages, and inhibition of the clustering of FcγRs on macrophages. Out of 353 kinases screened, **BZD-29** inhibited only 3 enzymes, giving it a selectivity score of 0.008 and making it the most selective ROCK inhibitor to date. This score also ranks **BZD-29** among the most selective kinase inhibitors in general.

Summary. The work described herein includes molecular modeling, design, synthesis, and structure activity relationship studies of a series of 1,4-benzodiazepine-2,5-diones. These studies aim to characterize and optimize the structural elements required for potent inhibition of ROCK by these compounds and to better understand the requirements for specificity among the kinome and among the ROCK isoforms themselves. Additionally, the approaches utilized in analog design were also assessed as to their abilities to predict quality analogs.

References

1. Kuby, J.; et al. *Immunology*, 4th ed.; W.H. Freeman & Co.: New York, 2000.
2. Browning, J.L. B-cells move to centre stage: novel opportunities for autoimmune disease treatment. *Nat Rev Drug Discov* **2006**, *5*, 564-576.
3. American Autoimmune Related Diseases Association, Inc. Questions and Answers. https://www.aarda.org/q_and_a.php. (accessed Aug 18, 2013).
4. The Merck Manual Home Health Handbook. Autoimmune Disorders. http://www.merckmanuals.com/home/print/immune_disorders/autoimmune_disorders/autoimmune_disorders.html. (accessed Aug 18, 2013)
5. Kumar, V.; et al. *Robbins and Cotran Pathologic Basis of Disease*, 6th ed. WB Saunders Company: Philadelphia, 1998.
6. Abbas, A; et al. *Basic Immunology. Functions and disorders of the immune system*, 3rd ed. WB Saunders Company: Philadelphia, 2009.
7. Kaplan, M. Apoptosis in systemic lupus erythematosus. *Clin. Immun.* **2004**, *112*, 210-218
8. Munoz, L.E.; et al. SLE—a disease of clearance deficiency? *Rheumatology* **2005**, *44*, 1101-1107.
9. Glocker, M.O. Rheumatoid arthritis, a complex multifactorial disease: on the way toward individualized medicine? *Med Res Rev* **2006**, *26*, 63-87.
10. Yokochi, S.; et al. An anti-inflammatory drug, propagermanium, may target GPI-anchored proteins associated with an MCP-1 receptor, CCR2. *Journal of Interferon and Cytokine Resarch* **2001**, *21*, 389-398.

11. Hiraya, C; et al. The VIIth biennial scientific meeting of the Asian Pacific Association for the study of the liver. Jakarta Indonesia, Trop. *Gastroenterol.* **1990**, *11*, 106-108.
12. Matsushima, K; et al. Purification and characterization of a novel monocyte chemotactic and activating factor produced by a human monocytic cell line. *J Exp Med* **1989**, *167*, 1883-1893.
13. Yoshimura, T.; et al. Purification and amino acid analysis of two human monocyte chemoattractants produced by phytohemagglutinin-stimulated human blood mononuclear cells. *J. Immunol.* **1989**, *142*, 1956-1962.
14. Hirayama, C; et al. Propagermanium: a nonspecific immune modulator for chronic hepatitis B. *J Gastroenterol* **2003**, *38*, 525-32.
15. Egorov, M.P.; Gaspar, P.P. Germanium: Organometallic chemistry. In *Encyclopedia of Inorganic Chemistry*; John Wiley & Sons: Hoboken, 1994.
16. Hubbard, S.R.; et al. Protein tyrosine kinase structure and function. *Annu Rev Biochem* **2000**, *69*, 373-398.
17. Hunter, T. Protein kinase classification. *Methods Enzymol* **1991**, *200*, 3-37.
18. Manning, G.; et al. The protein kinase complement of the human genome. *Science* **2002**, *298*, 1912-1934.
19. Asadullah, K.; et al. Protein Kinase Inhibitors for the treatment of inflammation-an overview. *Anti-inflammatory & Anti-allergy agents in Medicinal Chemistry* **2007**, *6*, 3-4.
20. Gaestel, M.; et al. Targeting innate immunity protein kinase signalling in inflammation. *Nat Rev Drug Discov* **2009**, *8*, 480-499.
21. Grant, S.K. Therapeutic protein kinase inhibitors. *Cell Mol Life Sci* **2009**, *66*, 1163-1177.

22. Force, T.; et al. Inhibitors of protein kinase signaling pathways: emerging therapies for cardiovascular disease. *Circulation* **2004**, *109*, 1196-1205.
23. Scapin, G. Structural biology and drug discovery. *Curr Pharm Des* **2006**, *12*, 2087-2097.
24. Liao, J.J. Molecular recognition of protein kinase binding pockets for design of potent and selective kinase inhibitors. *J Med Chem* **2007**, *50*, 409-424.
25. Cherry, M.; et al. Recent kinase and kinase inhibitor X-ray structures: mechanisms of inhibition and selectivity insights. *Curr Med Chem* **2004**, *11*, 663-673.
26. Buchanan, S. *Protein structure: discovering selective protein kinase inhibitors. Targets* **2003**, *2*, 101-108.
27. Noble, M.E.; et al. Protein kinase inhibitors: insights into drug design from structure. *Science* **2004**, *303*, 1800-1805.
28. Bossemeyer, D.; et al. Phosphotransferase and substrate binding mechanism of the cAMP-dependent protein kinase catalytic subunit from porcine heart as deduced from the 2.0Å structure of the complex with manganese(2+) adenylyl imidophosphate and inhibitor peptide PKI(5-24). *EMBO J.* **1993**, *12*, 849-859.
29. Ghose, A.K.; et al. Knowledge based prediction of ligand binding modes and rational inhibitor design for kinase drug discovery. *J Med Chem* **2008**, *51*, 5149-5171.
30. Liu, Y.; et al. Rational design of inhibitors that bind to inactive kinase conformations. *Nat Chem Biol* **2006**, *2*, 358-364.
31. Pargellis, C.; et al. Inhibition of p38 MAP kinase by utilizing a novel allosteric binding site. *Nat Struct Biol* **2002**, *9*, 268-272.
32. Wan, P.T.; et al. Mechanism of activation of the RAF-ERK signaling pathway by oncogenic mutations of B-RAF. *Cell* **2004**, *116*, 855-867.

33. Bishop, A.C. A hot spot for protein kinase inhibitor sensitivity. *Chem Biol* **2004**, *11*, 587-589.
34. Gorre, M.E.; et al. Clinical resistance to STI-571 cancer therapy caused by BCR-ABL gene mutation or amplification. *Science* **2001**, *293*, 876-880.
35. Mughal, T.I.; et al. Chronic myeloid leukemia: current status and controversies. *Oncology* **2004**, *18*, 837-844.
36. Shayani, S. Dasatinib, a multikinase inhibitor: therapy, safety, and appropriate management of adverse events. *Ther Drug Monit.* **2010**, *32*, 680–687.
37. Riento, K.; Ridley, A. ROCKs: multifunctional kinases in cell behavior. *Nature Rev Mol Cell Bio* **2003**, *4*, 446-456.
38. Matsui, T.; et al. Rho-associated kinase, a novel serine/threonine kinase, as a putative target for small GTP binding protein Rho. *Embo J* **1996**, *15*, 2208-2216.
39. Liao, J.K.; et al. Rho kinase (ROCK) inhibitors. *J Cardiovasc Pharmacol* 2007, *50*, 17-24.
40. Leung, T.; et al. A novel serine/threonine kinase binding the Ras-related RhoA GTPase which translocates the kinase to the peripheral membranes. *J. Biol. Chem.* **1996**, *270*, 29051-29054.
41. Nagawa, O. ROCK-I and ROCK-II, two isoforms of Rho-associated coiled-coil forming protein serine/threonine kinase in mice. *FEBS Lett* **1996**, *392*, 189-193.
42. Chen, X.Q.; et al. Characterization of RhoA-binding kinase ROK α implication of the pleckstrin homology domain in ROK α function using region-specific antibodies. *J. Biol. Chem.* 2002, *277*, 12680-12688.
43. Amano, M.; et al. The COOH terminus of Rho-kinase negatively regulates rho-kinase activity. *J. Biol. Chem.* **1999**, *274*, 32418-32424.
44. Yamaguchi, H.; et al. Molecular mechanism for the regulation of Rho-kinase by dimerization and its inhibition by Fasudil. *Structure* 2006, *14*, 589-600.

45. Yoneda, A.; et al. The Rho kinases I and II regulate different aspects of myosin II activity. *J Cell Biol* **2005**, *170*, 443-453.
46. Ishizaki, T.; et al. The small GTP-binding protein Rho binds to and activates a 160 kDa Ser/Thr protein kinase homologous to myotonic dystrophy kinase. *EMBO J.* **1996**, *15*, 1885-1893.
47. Matsui, T.; et al. Rho-associated kinase, a novel serine/threonine kinase, as a putative target for small GTP binding protein Rho. *EMBO J.* **1996**, *15*, 2208-2216.
48. Amano, M. et al. The COOH terminus of Rho-kinase negatively regulates rho-kinase activity. *J Biol Chem* **1999**, *274*, 32418-32424.
49. Leung, T.; et al. The p160 RhoA-binding kinase ROK alpha is a member of a kinase family and is involved in the reorganization of the cytoskeleton. *Mol Cell Biol* **1996**, *16*, 5313-5327.
50. Ishizaki, T.; et al. p160ROCK, a Rho-associated coiled-coil forming protein kinase, works downstream of Rho and induces focal adhesions. *FEBS Lett* **1997**, *404*, 118-124.
51. Sebbagh, M.; et al. Caspase-3-mediated cleavage of ROCK I induces MLC phosphorylation and apoptotic membrane blebbing. *Nat Cell Biol* **2001**, *3*, 346-352.
52. Coleman, M.L.; et al. Membrane blebbing during apoptosis results from caspase-mediated activation of ROCK I. *Nat Cell Biol* **2001**, *3*, 339-345.
53. Mueller, B.K.; et al. Rho kinase, a promising drug target for neurological disorders. *Nat Rev Drug Discov* **2005**, *4*, 387-398.
54. Amano M.; et al. The COOH terminus of Rho-kinase negatively regulates rho-kinase activity. *J Biol Chem* **1999**, *274*, 32418–32424.

55. Chen X.Q.; et al. Characterization of RhoA-binding kinase ROKalpha implication of the pleckstrin homology domain in ROKalpha function using region-specific antibodies. *J Biol Chem* **2002**, *277*, 12680–12688.
56. Ishizaki T.; et al. The small GTP-binding protein Rho binds to and activates a 160 kDa Ser/Thr protein kinase homologous to myotonic dystrophy kinase. *Embo J* **1996**, *15*, 1885–1893.
57. Leung T.; et al. The p160 RhoA-binding kinase ROK alpha is a member of a kinase family and is involved in the reorganization of the cytoskeleton. *Mol Cell Biol* **1996**, *16*, 5313–5327.
58. Amano M.; et al. Formation of actin stress fibers and focal adhesions enhanced by Rho-kinase. *Science* **1997**, *275*, 1308–1311.
59. Turner M.S.; et al. Characterization and purification of truncated human Rhokinase II expressed in Sf-21 cells. *Arch Biochem Biophys* **2002**, *405*, 13–20.
60. Francis, T.M. Target identification and validation of a novel family of anti-inflammatory 1,4-benzodiazepine-2,5-diones. Ph.D. Dissertation, University of Michigan, Ann Arbor, Michigan, 2010.
61. Riento, K.; et al. RhoE binds to ROCK I and inhibits downstream signaling. *Mol Cell Biol* **2003**, *23*, 4219-4229.
62. Riento, K.; et al. RhoE function is regulated by ROCK I-mediated phosphorylation. *Embo J* **2005**, *24*, 1170-1180.
63. Ongusaha, P.P.; et al. RhoE is a pro-survival p53 target gene that inhibits ROCK I-mediated apoptosis in response to genotoxic stress. *Curr Biol* **2006**, *16*, 2466-2472.
64. Du, J.; et al. Suppression of p160ROCK bypasses cell cycle arrest after Aurora-A/STK15 depletion. *Proc Natl Acad Sci U S A* **2004**, *101*, 8975-8980.
65. Ward, Y. The GTP binding proteins Gem and Rad are negative regulators of the Rho-Rho kinase pathway. *J Cell Biol* **2002**, *157*, 291-302.

66. Manapov, F.; et al. Translocation of p21(Cip1/WAF1) from the nucleus to the cytoplasm correlates with pancreatic myofibroblast to fibroblast cell conversion. *Gut* **2005**, *54*, 814-822.
67. Fischer, R.; et al. Calmodulin binds to and inhibits GTP binding of the ras-like GTPase Kir/Gem. *J Biol Chem* **1996**, *271*, 25067-25070.
68. Moyers, J.S.; et al. Rad and Rad-related GTPases interact with calmodulin and calmodulin-dependent protein kinase II. *J Biol Chem* **1997**, *272*, 11832-11839.
69. Moyers, J.S.; et al. Effects of phosphorylation on function of the Rad GTPase. *Biochem J* **1998**, *333*, 609-614.
70. Hartshorne D.J. Myosin phosphatase: subunits and interactions. *Acta Physiol Scand* **1998**, *164*, 483-493.
71. Rikitake Y.; et al. ROCKs as therapeutic targets in cardiovascular diseases. *Expert Rev Cardiovasc Ther* **2005**, *3*, 441–451.
72. Amano, M.; et al. Phosphorylation and activation of myosin by Rho-associated kinase (Rho-kinase). *J Biol Chem* **1996**, *271*, 20246-20249.
73. Fukata, Y.; et al. Phosphorylation of adducin by Rho-kinase plays a crucial role in cell motility. *J Cell Biol* **1999**, *145*, 347-361.
74. Goto, H.; et al. Phosphorylation of vimentin by Rho-associated kinase at a unique amino-terminal site that is specifically phosphorylated during cytokinesis. *J. Biol. Chem.* **1998**, *273*, 11728-11736.
75. Kawano, T.; et al. Phosphorylation of myosin-binding subunit (MBS) of myosin phosphatase by Rho-kinase in vivo. *J Cell Biol* **1999**, *147*, 1023-1038.
76. Leung, T.; et al. A novel serine/threonine kinase binding the Ras-related RhoA GTPase which translocates the kinase to the peripheral membranes. *J. Biol. Chem.* **1996**, *270*, 29051-29054.

77. Shi, J.; et al. Rho kinase in the regulation of cell death and survival. *Arch Immunol Ther Exp (Warsz)* **2007**, *55*, 61-75.
78. Segain, J.P.; et al. Rho kinase blockade prevents inflammation via nuclear factor kappa B inhibition: evidence in Crohn's disease and experimental colitis. *Gastroenterology* **2003**, *124*, 1180-1187.
79. Shimizu, Y.; et al. Contribution of small GTPase Rho and its target protein rock in a murine model of lung fibrosis. *Am J Respir Crit Care Med* **2001**, *163*, 210-217.
80. Wu, F.Q.; et al. Effects of fasudil on the expression of Rho kinase-1 and airway inflammation in a mouse model of asthma. *Chinese Journal of Tuberculosis and Respiratory Diseases* **2009**, *32*, 847-849.
81. Hashimoto, T.; et al. Lysophosphatidic acid enhances in vivo infiltration and activation of guinea pig eosinophils and neutrophils via a Rho/Rho-associated protein kinase-mediated pathway. *J Pharmacol Sci* **2003**, *91*, 8-14.
82. Zhihong, M; et al. Rho kinase inhibition by Fasudil has anti-inflammatory effects in hypercholesterolemic rats. *Biol Pharm Bull* **2011**, *34*, 1684-1689..
83. Uehata, M.; et al. Calcium sensitization of smooth muscle mediated by a Rho-associated protein kinase in hypertension. *Nature* **1997**, *389*, 990-994.
84. Yamaguchi, H.; et al. Structural basis for induced-fit binding of Rho-kinase to the inhibitor Y-27632. *J Biochem* **2006**, *140*, 305-311.
85. Yamaguchi, H.; et al. Molecular mechanism for the regulation of rho-kinase by dimerization and its inhibition by fasudil. *Structure* **2006**, *14*, 589-600.
86. Jacobs, M.; et al. The structure of dimeric ROCK I reveals the mechanism for ligand selectivity. *J Biol Chem* **2006**, *281*, 260-268.
87. Doe, C.; et al. Novel Rho kinase inhibitors with anti-inflammatory and vasodilatory activities. *J Pharmacol Exp Ther* **2007**, *320*, 89-98.

88. Darenfed, H.; et al. Molecular characterization of the effects of Y-27632. *Cell Motil Cytoskeleton* **2007**, *64*, 97-109.
89. Yarrow, J.C.; et al. Screening for cell migration inhibitors via automated microscopy reveals a Rho-kinase inhibitor. *Chem Biol* **2005**, *12*, 385-395.
90. Tokushige, H.; et al. Effects of topical administration of Y-39983, a selective rho-associated protein kinase inhibitor inhibitor, on ocular tissues in rabbits and monkeys. *IOVS* **2007**, *48*, 3216-3222.
91. Feng, Y.; et al. Discovery of substituted 4-(pyrazol-4-yl)-phenylbenzodioxane-2-carboxamides as potent and highly selective Rho kinase (ROCK-II) inhibitors. *J Med Chem* **2008**, *51*, 6642-6645.
92. Bain, J.; et al. The selectivity of protein kinase inhibitors: a further update. *Biochem J* **2007**, *408*, 297–315.
93. Bamborough, P.; et al. Assessment of chemical coverage of kinome space and its implications for kinase drug discovery. *J Med Chem* **2008**, *51*, 7898–7914.
94. Fabian, M.A.; et al. A small molecule-kinase interaction map for clinical kinase inhibitors. *Nat Biotechnol* **2005**, *23*, 329–336.
95. Fedorov, O.; et al. A systematic interaction map of validated kinase inhibitors with Ser/Thr kinases. *Proc Natl Acad Sci U S A* **2007**, *104*, 20523–20528.
96. Goldstein, D.M.; et al. High-throughput kinase profiling as a platform for drug discovery. *Nat Rev Drug Discov* **2008**, *7*, 391–397.
97. Karaman, M.W.; et al. A quantitative analysis of kinase inhibitor selectivity. *Nature Biotechnology* **2008**, *26*, 127–132.
98. Huang, D.; et al. Kinase selectivity potential for inhibitors targeting the ATP binding site: A network analysis. *Structural Bioinformatics* **2010**, *26*, 198-204.
99. Davies, S.P.; et al. Specificity and mechanism of action of some commonly used protein kinase inhibitors. *Biochem J* **2000**, *351*, 95-105.

100. Shimizu, Y.; et al. ROCK-I regulates closure of the eyelids and ventral body wall by inducing assembly of actomyosin bundles. *J Cell Biol* **2005**, *168*, 941–953.
101. Thumkeo, D.; et al. Targeted disruption of the mouse rho-associated kinase 2 gene results in intrauterine growth retardation and fetal death. *Mol Cell Biol* **2003**, *23*, 5043–5055.
102. Thumkeo, D.; et al. ROCK-I and ROCK-II cooperatively regulate closure of eyelid and ventral body wall in mouse embryo. *Genes Cells* **2005**, *10*, 825–834.
103. Yoneda, A.; et al. The Rho kinases I and II regulate different aspects of myosin II activity. *J Cell Biol* **2005**, *170*, 443–453.
104. Matsui, T.; et al. Rho-associated kinase, a novel serine/threonine kinase, as a putative target for small GTP binding protein Rho. *EMBO J.* **1996**, *15*, 2208–2216.
105. Ishizaki, T.; et al. The small GTP-binding protein Rho binds to and activates a 160 kDa Ser/Thr protein kinase homologous to myotonic dystrophy kinase. *EMBO J.* **1996**, *15*, 1885–1893.
106. Wang, Y.; et al. ROCK isoform regulation of myosin phosphatase and contractility in vascular smooth muscle cells. *Circ Res* **2009**, *104*, 531–540.
107. Rikitake, Y.; et al. Decreased perivascular fibrosis but not cardiac hypertrophy in ROCK1 \pm haploinsufficient mice. *Circulation* **2005**, *112*, 2959–2965.
108. Wong, C.C.; et al. Rhokinase 2 is frequently overexpressed in hepatocellular carcinoma and involved in tumor invasion. *Hepatology* **2009**, *49*, 1583–1594.
109. Vishnubhotla, R.; et al. ROCK-II mediates colon cancer invasion via regulation of MMP-2 and MMP-13 at the site of invadopodia as revealed by multiphoton imaging. *Lab Invest* **2007**, *87*, 1149–1158.
110. Kamai, T.; et al. Significant association of Rho/ROCK pathway with invasion and metastasis of bladder cancer. *Clin Cancer Res* **2003**, *9*, 2632–2641.

111. Lane, J.; et al. The expression and prognostic value of ROCK I and ROCK II and their role in human breast cancer. *Int J Oncol* **2008**, 33, 585–593.
112. Sebbagh, M.; et al. Direct cleavage of ROCK II by granzyme B induces target cell membrane blebbing in a caspase-independent manner. *J Exp Med* **2005**, 201, 465–471.
113. Chen, X.Q.; et al. Characterization of RhoA-binding kinase ROKalpha implication of the pleckstrin homology domain in ROKalpha function using region-specific antibodies. *J Biol Chem* **2002**, 277, 12680-12688.
114. Somlyo, A.V.; et al. Rho-kinase inhibitor retards migration and in vivo dissemination of human prostate cancer cells. *Biochem Biophys Res Commun* **2000**, 269, 652-659.
115. Zhang, Y.; et al. Rock2 controls TGF{beta} signaling and inhibits mesoderm induction in zebrafish embryos. *J Cell Sci* **2009**, 122, 2197–2207.
116. Ongusaha, P.P.; et al. Identification of ROCK1 as an upstream activator of the JIP-3 to JNK signaling axis in response to UVB damage. *Sci Signal* **2008**, 1, ra14.
117. Shea, K.F.; et al. ROCK1 and LIMK2 interact in spread but not blebbing cancer cells. *PLoS ONE* **2008**, 3, e3398.
118. Zhang, Y.M.; et al. Targeted deletion of ROCK1 protects the heart against pressure overload by inhibiting reactive fibrosis. *FASEB J* **2006**, 20, 916–925.
119. Lin, S.L.; et al. Hyaluronan stimulates transformation of androgen-independent prostate cancer. *Carcinogenesis* **2007**, 28, 310–320.
120. Arimura, N.; et al. Phosphorylation of collapsin response mediator protein-2 by Rho-kinase. Evidence for two separate signaling pathways for growth cone collapse. *J Biol Chem* **2000**, 275, 23973-23980.
121. Zhou, Z.; et al. A critical role of Rho-kinase ROCK2 in the regulation of spine and synaptic function. *Neuropharmacology* **2009**, 56, 81-89.

122. Shimizu, Y.; et al. ROCK-I regulates closure of the eyelids and ventral body wall by inducing assembly of actomyosin bundles. *J Cell Biol* **2005**, *168*, 941-953.
123. Thumkeo, D.; et al. Targeted disruption of the mouse rho-associated kinase 2 gene results in intrauterine growth retardation and fetal death. *Mol Cell Biol* **2003**, *23*, 5043-5055.
124. Thumkeo, D.; et al. ROCK-I and ROCK-II cooperatively regulate closure of eyelid and ventral body wall in mouse embryo. *Genes Cells* **2005**, *10*, 825-834.
125. Rikitake, Y.; et al. Decreased perivascular fibrosis but not cardiac hypertrophy in ROCK1+/- haploinsufficient mice. *Circulation* **2005**, *112*, 2959-2965.
126. Zhang, Y.M.; et al. Targeted deletion of ROCK1 protects the heart against pressure overload by inhibiting reactive fibrosis. *Faseb J.* **2006**, *20*, 916-925.
127. Rikitake, Y.; et al. Rho-kinase mediates hyperglycemia-induced plasminogen activator inhibitor-1 expression in vascular endothelial cells. *Circulation* **2005**, *111*, 3261-3268.
128. Fu, P.; et al. Signaling mechanism of renal fibrosis in unilateral ureteral obstructive kidney disease in ROCK1 knockout mice. *J Am Soc Nephrol* **2006**, *17*, 3105-3114.
129. Goodman, K.B.; et al. Development of dihydropyridone indazole amides as selective Rho-kinase inhibitors. *J Med Chem* **2007**, *50*, 6–9.
130. Stavenger, R.A.; et al. Discovery of aminofurazan- azabenzimidazoles as inhibitors of Rho-kinase with high kinase selectivity and antihypertensive activity. *J Med Chem* **2007**, *50*, 2–5.
131. Kast, R.; et al. Cardiovascular effects of a novel potent and highly selective azaindole-based inhibitor of Rho-kinase. *Br J Pharmacol* **2007**, *152*, 1070–1080.
132. Schirok, H.; et al. Design and synthesis of potent and selective azaindole-based Rho kinase (ROCK) inhibitors. *ChemMedChem* **2008**, *3*, 1893–1904.

133. Schueller, O.; et al. Abstract 1216: Selective ROCK 2 inhibition attenuates arterial plaque formation in an ApoE knockout mouse model. *Circulation* **2006**, *114*, II_228-b-.

Chapter 2

CORRELATING MOLECULAR STRUCTURE WITH *IN VITRO* FUNCTION FOR SAR MODEL DEVELOPMENT

Introduction

Assessment of the possible correlations that exist between *in vitro* activity and the physicochemical properties of molecules helps to formulate models describing parallels between specific molecular attributes and molecular function^{1,2}. These models were vital since these inhibitors were targeting a protein where structural information was limited. Specifically, the electronic, hydrophilic, and steric properties of compounds which demonstrated Rho-kinase inhibition were mapped to determine which properties were conducive to potent inhibition of ROCKII and/or ROCKII isoform selectivity.

Chemical descriptors or parameters were used to describe these three features; their values have been experimentally determined for certain substituents and are reported in the literature. Specifically, LogP and π values, both of which are determined through measurements of the partitioning of molecules between water and n-octanol and are used to describe hydrophilicity (lower values signify greater hydrophilicity)^{3,4}. Similarly, electronic characteristics are described by σ , or the Hammett constants, and molecular size and steric properties are described using molecular weight (MW) and molar refraction (MR)^{2,5,6}. Polar surface area (PSA), defined as the sum of the surfaces

of polar atoms of a molecule, including attached hydrogens, is a property used to represent permeability (lower values tend to permeate more efficiently). **Table 2.1** summarizes these descriptors⁷.

Table 2.1. Physicochemical properties and their respective descriptors⁷.

Property	Description
LogP	Describes hydrophilicity. Lower LogP= greater hydrophilicity
π	Describes hydrophobicity. Higher π = more hydrophobic
σ	Describes electronic properties. Lower σ = more electron rich
MR	Molar refraction. Steric descriptor.
MW	Molecular weight. Steric descriptor.
PSA	Polar surface area.

Models of structure activity relationships. The Free-Wilson analysis was one of the first models relating compound substitution to biological activity⁸. In this approach, a statistical model is generated which correlates *in vitro* activity to compound substitution⁹. The Free-Wilson analysis was refined by Corwin Hansch in order to derive a statistical model incorporating multiple substituent descriptors so that correlations may be identified when multiple characteristics are changed simultaneously². Additionally, in order to increase the interpretability of these analyses, Hansch set minimal statistical guidelines¹⁰. The statistical Hansch analysis continues to be one of the most popular methods used in quantitative structure activity relationship (QSAR) campaigns¹¹.

One significant hurdle in the analysis of compound data is the slow pace of synthesis relative to the rapid generation of *in vitro* activity. Although QSAR is a

powerful tool in correlating molecular function with structure, in order to minimize chance correlations, this methodology requires expansive data sets¹². Therefore, when smaller data series are studied, alternative methods are used which qualitatively, rather than quantitatively, identify such associations¹³⁻¹⁵.

One example of a qualitative approach that can be utilized without statistical models is the manual Hansch analysis. First proposed by Topliss, this method examines only the hydrophobic and electronic properties of the substituents, π and σ ¹⁵. This approach allows structure-function correlations with π and σ to be studied independently (**Table 2.2**, columns 2, 3, and 8) using the relationships outlined (**Table 2.2**, Columns 4-7, 9, 10). One advantage of such an analysis over QSAR methods is the ability to analyze data sets limited to as few as five compounds^{13,15}. In the manual Hansch analysis, molecules are ranked by each of their physicochemical relationships and also by potency. When the potency ranking and a physicochemical property ranking match, a likely association between structure and *in vitro activity* is identified. New analogs are then based on the identified correlations.

Table 2.2. Relationships between π and σ used in the manual Hansch analysis⁷.

X	π	σ	$\pi-\sigma$	$2\pi-\sigma$	$\pi-2\sigma$	$\pi-3\sigma$	$-\sigma$	$\pi+\sigma$	$2\pi-\pi^2$
H	0	0	0	0	0	0	0	0	0
4-Cl	0.71	0.23	0.48	1.19	0.25	0.02	-0.23	0.94	0.92
4-CH ₃	0.56	-0.17	0.73	1.29	0.90	1.07	0.17	0.39	0.81
4-CF ₃	0.88	0.54	0.34	1.22	-0.2	-0.74	-0.54	1.42	0.99
4-Br	0.86	0.23	0.57	1.49	0.40	1.55	-0.23	1.09	0.98

The qualitative estimate of correlations in electronic or hydrophobic properties with *in vitro activity* is then used to predict new substituents that are likely to increase

potency. For instance, if potency of a set of compounds increases as π increases but does not change with σ alterations, it is more beneficial to vary the π values of new analogs than to incorporate changes in σ values.

1,4-Benzodiazepines: privileged structures. The term “privileged structure” has emerged as one method of accelerating the drug discovery process, especially in cases in which structural information of the target is limited or even completely unknown. Evans first introduced the term “privileged structure” in 1988, in reference to the 1,4-benzodiazepine-2-one heterocycle, as “a single molecular framework able to provide ligands for diverse receptors¹⁶.” Recently, use of the privileged scaffold terminology has been expanded to include multiple molecules of the same structural nucleus having bioactivity, regardless of their ability to bind multiple targets. These regularly occurring structural motifs are often composed of two or three heterocyclic ring systems connected by a single bond or fusion ring^{17,18}. Due to the recognition of the potential of privileged scaffolds as templates to be derivatized in the discovery of new protein-binding ligands, they often function as the starting point in the development of libraries for the identification of novel bioactive molecules, even when the mechanisms responsible for the activity of these motifs are unclear¹⁹.

Several general aspects of privileged structures combine to make them attractive templates for compound libraries in the discovery of new protein-binding ligands. Specifically, these structures are generally small heterocycles and thus often possess favorable solubility profiles. Next, the non-planarity of the scaffolds tends to avoid promiscuous binding while their robust conformations provide stable template shapes, even as substitutions are varied during lead optimization²⁰. Relevant 3D-

pharmacophores are also addressed by such structures due to their remarkable bond exit vector arrangement, and these entities often possess favorable *a priori* drug-like properties since they represent a balance of polarity as well as metabolic stability. Finally, privileged structures generally provide readily available libraries of compounds due to their facile synthesis²⁰.

Although simple empirical observations have led to the identification of many privileged structures, computational efforts have also been used to highlight the privileged nature of the molecular frameworks of known drugs. These investigations revealed a significant proportion (24%) of drug molecules are based on a small number of molecular skeletons which can be classified as privileged structures, including pyrrolopyridine, benzodiazepine, and quinazoline^{6,17,18}. Specifically, the benzodiazepine nucleus is believed to be privileged due to its structural mimicry of a beta peptide turn (**Figure 2.1**)²¹.

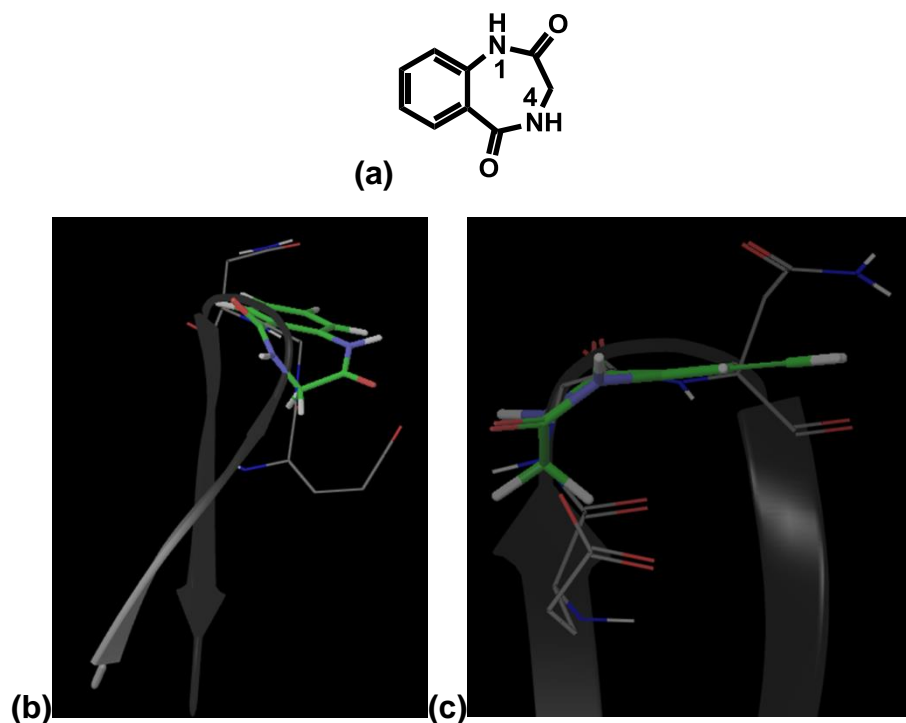


Figure 2.1. (a) The 1,4-benzodiazepine nucleus. (b) & (c) Views of the 1,4-benzodiazepine nucleus (green) aligned with a β -peptide turn (grey) (PDB: 1N09)²².

The central benzodiazepine receptor component of the GABA_A receptor complex is likely the most well-known target of benzodiazepines²¹. The GABA_A receptor is a protein complex located in the synapses of neurons, controlled by the chief central nervous system inhibitory neurotransmitter, γ -aminobutyric acid (GABA)²³. In addition to two GABA binding sites, all GABA_A receptors contain an ion channel which conducts chloride ions across neuronal cell membranes. Benzodiazepines function through the promotion of binding of GABA to the GABA_A receptor by locking the receptor into a specific conformation, resulting in more frequent opening of the associated chloride ion channel and an increase in the total conduction of chloride ions across the membrane of the neuron; this ultimately results in hyperpolarization of the membrane and a subsequent decrease in the excitability of neurons^{24,25}.

As Evans initially acknowledged, benzodiazepines are capable of binding multiple receptors, and thus have been developed as inhibitors of an array of protein targets, including melancortin receptor, potassium channels, Src protein tyrosine kinase, HIV reverse transcriptase, platelet aggregation factor, endothelin receptor, cholecystokinin, AMPA/kainite, phosphodiesterases-4, oxytocin, cMpl, vasopressin V2, HIV type 1 virus TAR-RNA, bradykinin B2, and fibrinogen²⁶⁻⁴⁷.

Mechanism of action studies. When developing inhibitors of kinases, it is important to consider the different mechanisms of kinase regulation which exist and which may be exploited by such inhibitors. Although there are a variety of possibilities of how an inhibitor might bind to a protein kinase, the majority act by competing either for the ATP binding site or for the substrate binding site. Due to the structural similarities between **BZD-29** and other ATP-competitive kinase inhibitors, the observation that all known ROCK inhibitors act by competing for ATP, and the knowledge that the vast majority of all protein kinase inhibitors bind at the ATP cleft, it was hypothesized that **BZD-29** inhibited ROCK through competition for the ATP binding site.

Mechanism of action studies are designed to assign a specific inhibition mode to a compound based on how the rate of the kinase enzymatic reaction is affected by changes in different parameters. The most common types of inhibition are competitive, noncompetitive, and uncompetitive⁶⁴. A competitive inhibitor binds to the target at the same binding site as the endogenous ligand in question (ATP or substrate), preventing activation of the enzyme by competing for the same binding site, and thus reducing its ability to catalyze the transfer of phosphorous from ATP to a substrate. A non-

competitive inhibitor may either bind to the same site as the endogenous ligand or to an allosteric site, and in either case will reduce the maximum reaction velocity of the enzyme. An uncompetitive inhibitor, however, is only capable of binding an enzyme complex between the protein and an endogenous ligand⁶⁴.

Kinase assay selection. Although initially many biochemical assays designed to measure kinase inhibition may appear similar, many factors such as enzyme construct and concentration, substrate selection and concentration, reaction buffer, Mg^{2+} and Mn^{2+} concentration, and the amount of ATP present can have large effects on the resulting data. With regards to ROCK, a 2011 publication cited an experiment in which a series of potential substrates in the presence of increasing ROCKII kinase concentrations were examined to determine the substrate which yielded the highest kinase activity (**Figure 2.2**)⁴⁹. Here, the S6-derived peptide was found to be phosphorylated most efficiently, providing the highest assay signal at low concentrations of kinase enzyme. Because the lowest IC_{50} value which can be determined is defined as half of the kinase concentration in the assay (known as the “assay wall”)⁴⁹, it is important that a biochemical assay be optimized for a low concentration of kinase^{50,51}. Additionally, these experiments highlighted the linear assay region for ROCKII in the presence of the S6-derived peptide, found to exist between ROCK concentrations of 0.5 and 7 nM. Next, the authors determined the optimum composition of the reaction buffer, and concluded that maximum ROCKII activity was observed at 10 mM $MgCl_2$, in the absence of $MnCl_2$, and at pH of approximately 7.5. Considering these results, the protocols of the biochemical assays used to analyze the current inhibitor series met all

of the above criteria for optimized ROCK assays (see Methods and Materials section for details).

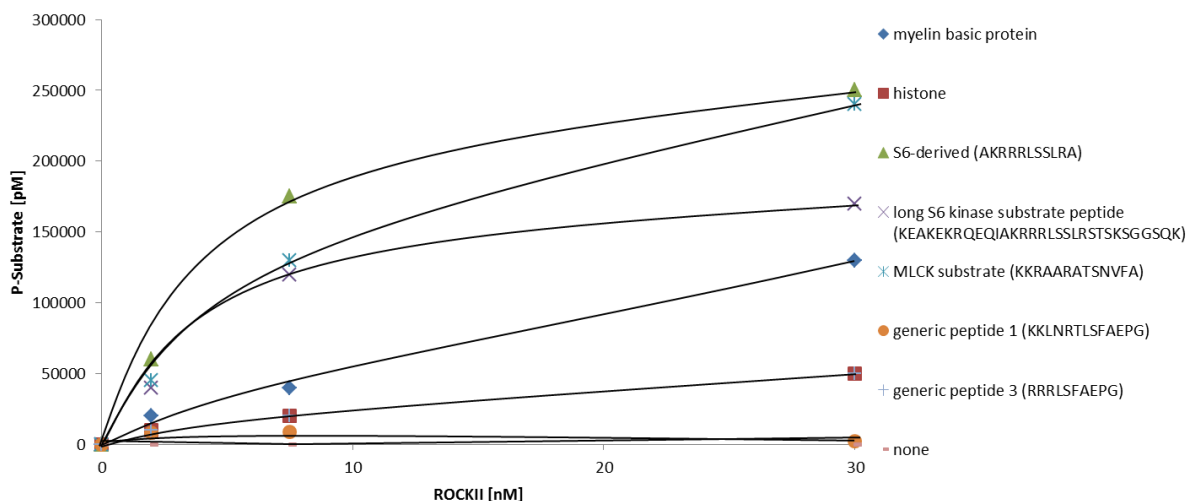


Figure 2.2. Increasing concentrations of ROCKII with various potential substrates⁴⁹.

Another critical factor in conducting kinase assays is the choice of ATP concentration. When inhibition assays are being conducted on more than one kinase to determine inhibitor affinity as well as selectivity among the kinases being analyzed (as was the case in these studies, for ROCKI and ROCKII), the ATP concentrations of the individual assays should equal the K_m values for each enzyme⁴⁹. The K_m , or the Michaelis-Menten constant, approximates the affinity between ATP and the kinase, whereas another constant known as the inhibitor constant (K_i), directly describes the binding affinity of an inhibitor for a kinase; these constants relate to the IC_{50} of the inhibitor by the Cheng-Prusoff equation (**Equation 2.1**)⁵². Since IC_{50} values determined in an assay at an ATP concentration equal to its K_m value reflect $2 \times K_i$ value, the IC_{50} is therefore a direct measurement of the affinity of an inhibitor for a kinase (**Equation 2.1**). This means that the selectivity of an inhibitor amongst multiple kinases can then be

ranked based on its binding affinity for those kinases. Essentially, it allows for direct comparisons of binding affinity between kinases while such comparisons using standard ATP concentrations are arbitrary and meaningless⁵². Therefore, all biochemical assays were conducted at the respective apparent K_m values for the ROCKI and ROCKII kinases.

$$IC_{50} = K_i + \frac{K_i}{K_m} \times [ATP] \xrightarrow{[ATP] = K_m} IC_{50} = K_i + \frac{K_i}{K_m} \times K_m = 2 \times K_i$$

K_m : Michaelis Menten constant

K_i : Inhibitor constant

[ATP]: ATP concentration

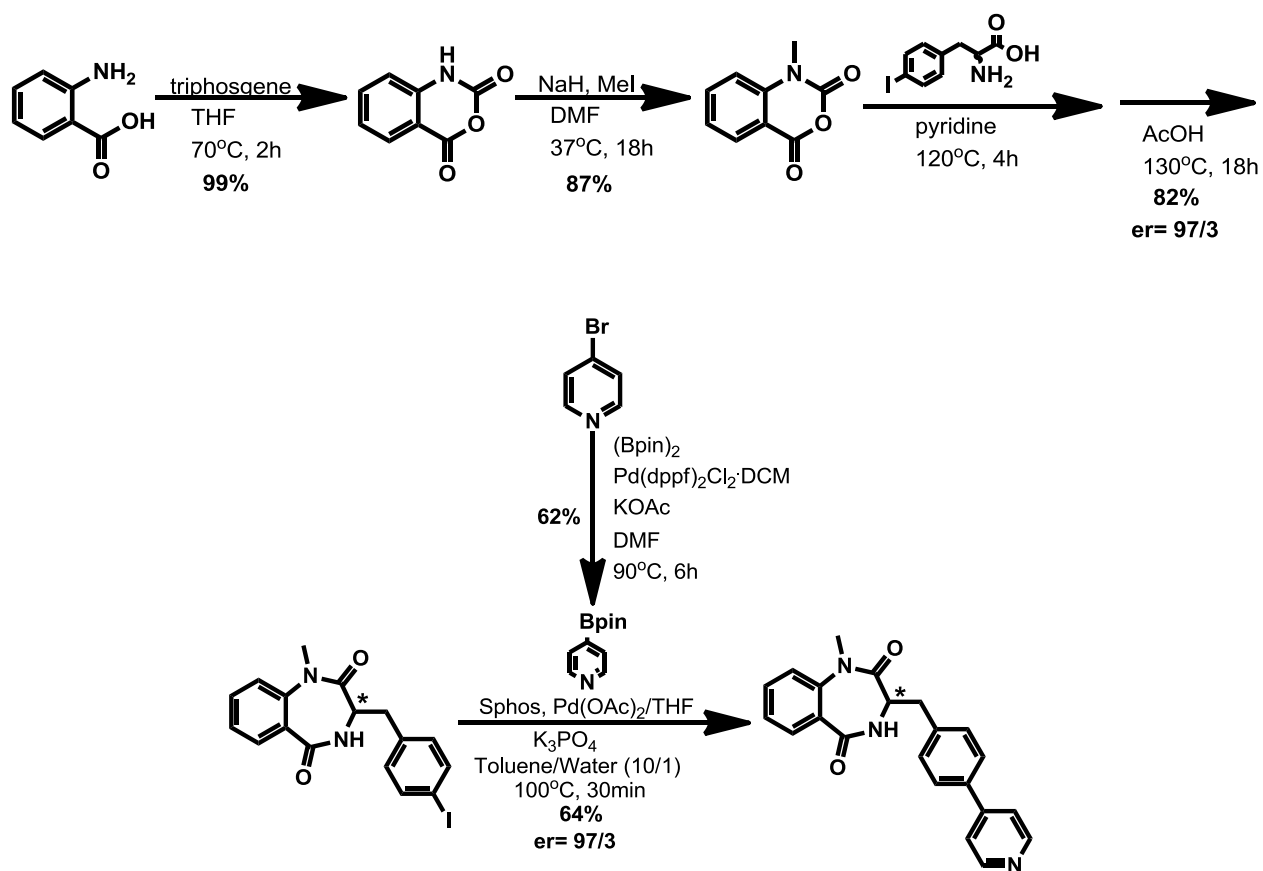
Equation 2.1. The Cheng-Prusoff equation⁵².

Maximizing optimization campaign efficiency. In this research, traditional medicinal chemistry methods of structure activity relationship (SAR) analysis were combined with computational models and docking predictions to thoroughly explore the chemical space while enhancing potency with the production of the fewest analogs possible. For instance, in formulating SAR models describing the physicochemical properties of inhibitors associated with potent inhibition and/or selectivity, although incorporating random substituents of varying electronic, hydrophilic, and steric properties would suffice, if these modifications are instead correlated to those which would provide the most useful information with regards to a computational model, this would greatly improve the efficiency of lead optimization. This computational model in turn might help in avoiding potentially problematic modifications and in rationalizing assay results which may not be easily explained by SAR models alone.

Alternatively, although it may be possible to optimize an inhibitor purely through computational means, however this often results in a haphazard “wreck-and-check” campaign in which highly specialized motifs are introduced to make specific contacts with the target. With such an approach, it is often difficult to interpret the relationships among the biochemical data of the resultant compound library. However, if traditional medicinal chemistry SAR techniques accompany such methodology, the effects of these specialized modifications may be assessed by their relation to the general electronic or steric environment of all or part of the target binding site. This may allow researchers to determine whether the effects of a modification stem from a specific contact with the target, from general electronic or steric complementarity, or from both.

RESULTS AND DISCUSSION

Synthesis of enantiopure **BZD-29** analogs. In planning the synthesis of the **BZD-29** analogs, it was important to optimize a route for high yield, to expedite production and simplify purification, and for tolerance of diverse substituents. Additionally, it was desirable to develop a stereoselective synthesis to produce analogs with a high degree of optical purity for modeling purposes and a thorough understanding of the structure activity relationships at play. Although it is possible to separate benzodiazepine enantiomers with the use of a chiral column, this would result in pure enantiomers of unknown absolute configuration. An example of the initial route utilized is shown below in **Scheme 2.1**.

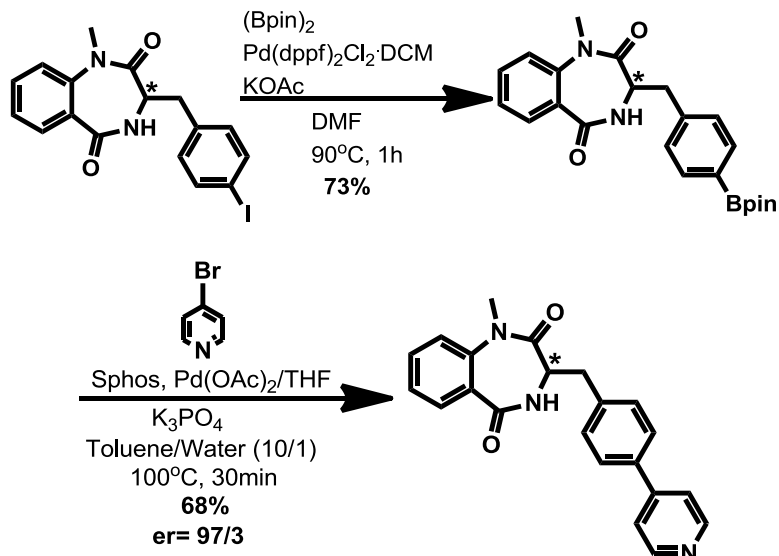


Scheme 2.1. Initial benzodiazepine synthetic route.

Unless the desired isatoic anhydride was readily commercially available, this route began with the cyclization of the necessary anthranilic acid with triphosgene in tetrahydrofuran (THF), resulting in nearly complete conversion. Next, the isatoic anhydride was methylated with methyl iodide in N,N-dimethylformamide (DMF) at excellent yield. The N-methyl isatoic anhydride was then coupled with an optically pure iodophenylalanine in pyridine before cyclization by refluxing in acetic acid, at excellent yield. Next, an efficient Suzuki-Miyaura coupling was carried out with the desired boronated heterocycle, produced in a Miyaura borylation of the halogenated heterocyclic starting material at good yield. Although it was possible to achieve a slight increase in the yield of the Suzuki step (68%) through extended reaction time, this resulted in

racemization of the chiral center so that the benefit of the yield increase was outweighed by the cost of the need for a chiral column to produce final products of optical purity >95% er (enantiomeric ratio) for the desired enantiomer.

Suzuki partner role swapping. One limitation to the route depicted in **Scheme 2.1**, however, was that not all desired heterocyclic boronic acids were commercially available or easily synthesized. It was recognized, however, that in swapping the coupling partners of the Suzuki, it was possible to incorporate greater diversity at the heterocycle while also somewhat improving the yield of the borylation step and still maintaining a good yield of the Suzuki step (**Scheme 2.2**). It has previously been reported by Prieto et al. that partner role swapping from an aryl halide and a heterocyclic boronic acid (or boronic acid pinacol ester, etc.) to the respective halogenated heterocycle and an arylboronic acid can actually improve the yield of the Suzuki reaction⁵⁶. Additionally, it was noted by the same authors that the lack of a protecting group, in the cases of heterocycles with secondary amines (indazoles, azaindoles, etc.), produced equivalent or even improved yields in these reactions. This was found this to be the case when such heterocycles were incorporated in the current analog series. This was significant as it allowed the avoidance of two additional steps, protection and deprotection, in the production of each inhibitor.



Scheme 2.2. Partner role swapping of Suzuki coupling partners.

The mechanism of ROCK inhibition by BZD-29. Mechanism of action studies began with experiments designed to obtain K_m for ATP or substrate in the presence of **BZD-29** (Figure 2.3). Because no specific mode of action of the inhibitor was assumed, first, a 10-dose IC_{50} curve was generated. The reactions were monitored every 5-15 minutes to obtain progress curves with time course. At each time point, radioisotope signal (^{33}P) was converted into “ μM phosphate transferred to substrate,” and was plotted against time. The slope of the linear portion of the progress curve was obtained by linear regression in Excel. The slopes (or velocity; $\mu M/min$) were then plotted against ATP or substrate concentrations for Michaelis-Menten plots, and subsequent Lineweaver-Burk plots (double-reciprocal plots), using the GraphPad Prism software. The results were further analyzed with global fit using GraFit software.

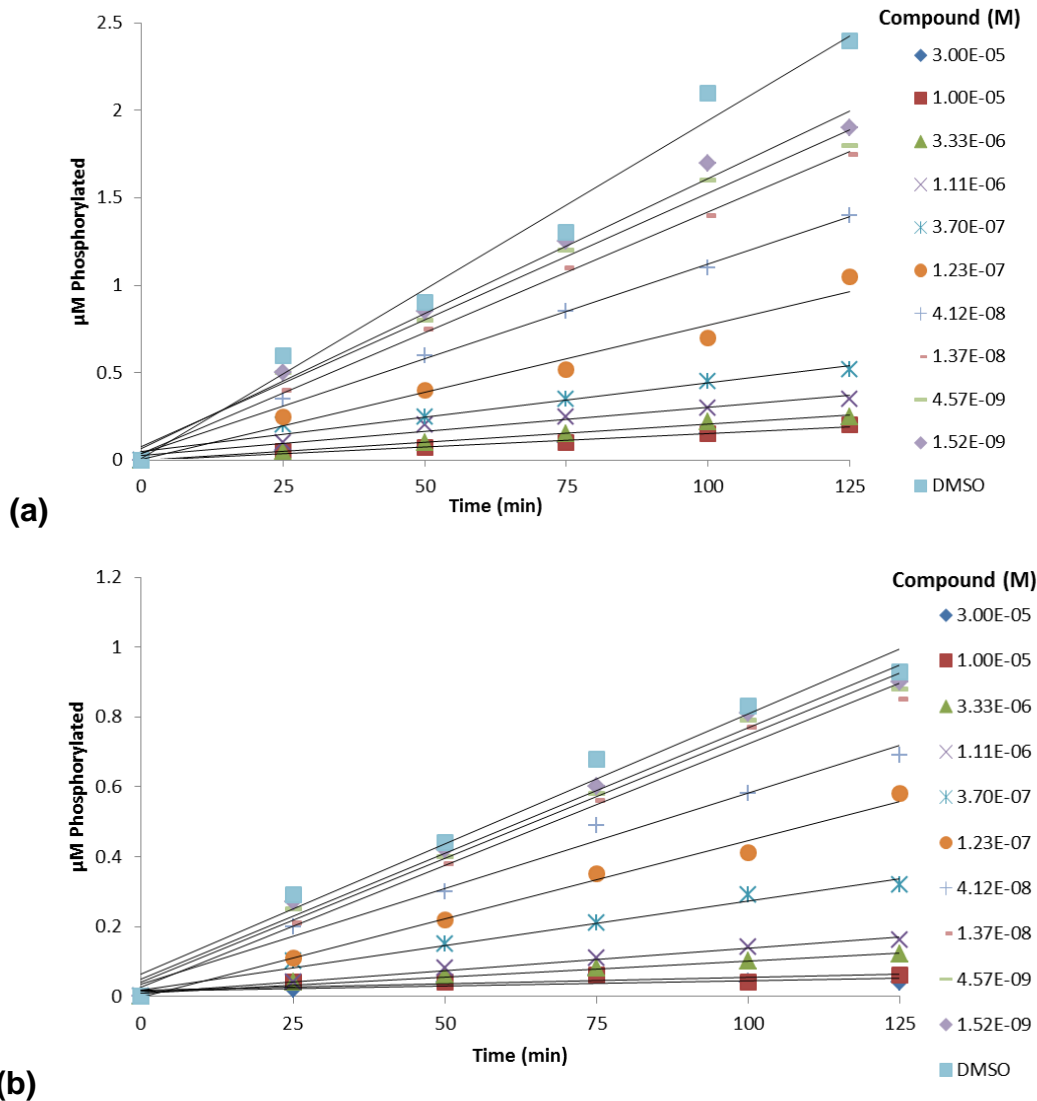


Figure 2.3. Progress curves for ROCKI (a) and ROCKII (b) at 15 μM with **BZD-29**. Experiments performed by Reaction Biology Corp.

The progress curves for ROCKI and ROCKII reactions were linear with time in the absence and presence of **BZD-29** for 120 minutes (**Figure 2.3**), suggesting the inhibition by **BZD-29** was not time-dependent. The velocities ($\mu\text{M phosphorylated}/\text{min} = \text{velocity}$) were obtained by taking the linear portions of these progress curves for further analyses. The slopes obtained from these progress curves were plotted against ATP or substrate concentrations for Michaelis-Menten plots (**Figure 2.4**) and double-reciprocal

plots (**Figure 2.5**) for **BZD-29** at selected concentrations against ROCKI and ROCKII. Due to the redundancy of the ROCKI and ROCKII data in these experiments, only the results for ROCKI are shown.

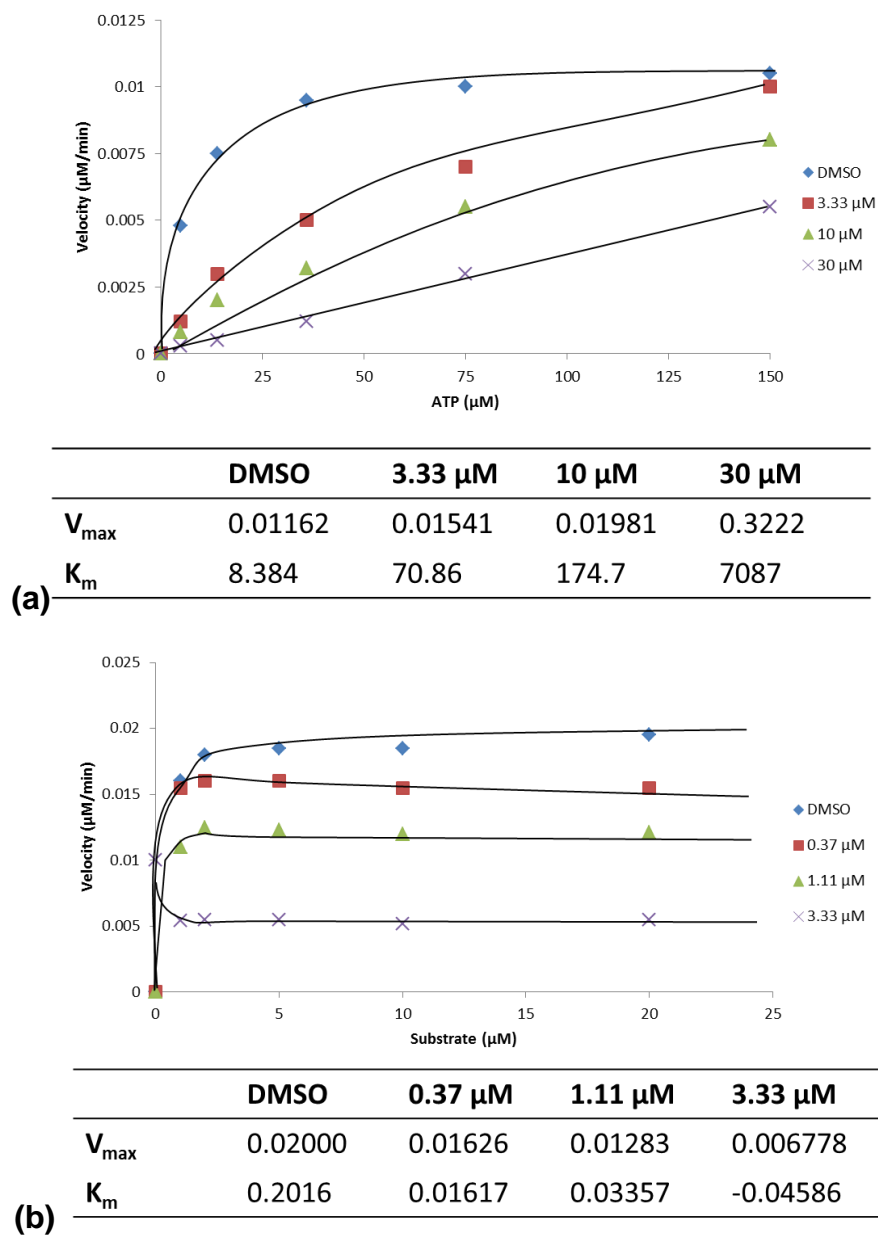


Figure 2.4. Michaelis-Menten plots for ROCKI with **BZD-29** and varying concentrations of ATP (**a**) or substrate (**b**). Experiments performed by Reaction Biology Corp.

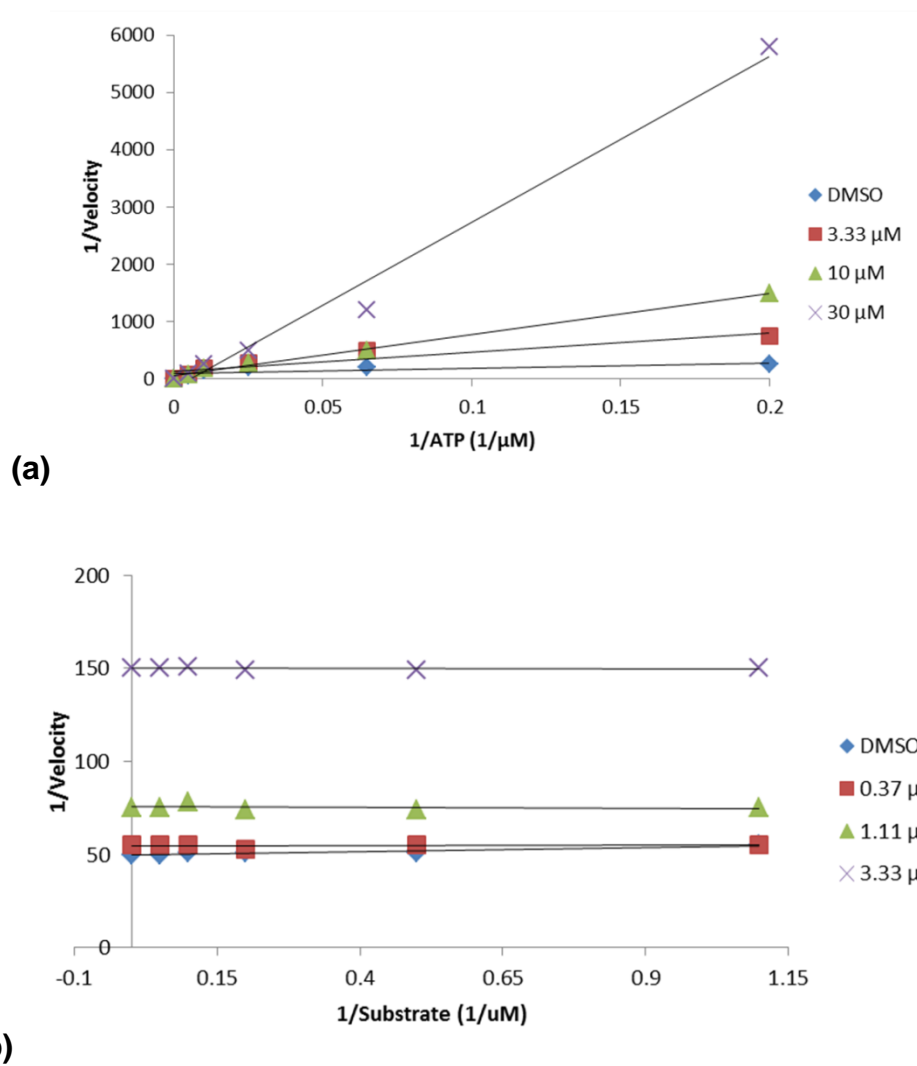


Figure 2.5. Lineweaver-Burk plots for ROCKI with **BZD-29** and varying concentrations of ATP **(a)** or substrate **(b)**. Experiments performed by Reaction Biology Corp.

The apparent K_m values for ATP are increased when the inhibitor concentration is increased in the Michaelis-Menten plot (**Figure 2.4, a**), and all lines are converged on the Y-axis in the double-reciprocal plot (**Figure 2.5, a**), suggesting that **BZD-29** is competitive with respect to ATP against ROCKI and ROCKII. However, the apparent K_m values for the substrate are relatively unchanged when the inhibitor concentration is increased, as shown by the associated Michaelis-Menten plots (**Figure 2.4, b**).

Additionally, a negative K_m value at 3.33 μM inhibitor concentration for ROCKI suggests that the curve fit is hard to perform due to low K_m value. Furthermore, the double-reciprocal plot (**Figure 2.5, b**) shows all lines are nearly parallel, suggesting that the compound is uncompetitive with respect to substrate against ROCKI and ROCKII.

Next, when the percentage of enzyme activity relative to DMSO control at each ATP concentration is plotted against compound concentration and IC_{50} curves are generated, IC_{50} values are shifted higher when ATP concentration is increased (**Figure 2.6, a**). This shift of IC_{50} curves also suggests that the compound is ATP competitive. When similar IC_{50} curves are generated for varying substrate concentrations, however, IC_{50} values are shifted lower when the substrate concentration is increased (**Figure 2.6, b**). These shifts, although minor, also suggest that the compound is substrate uncompetitive. Because an uncompetitive inhibitor can only bind the enzyme:substrate complex, raising the concentration of the substrate in turn increases the concentration of this complex, and this then allows the inhibitor to bind more efficiently.

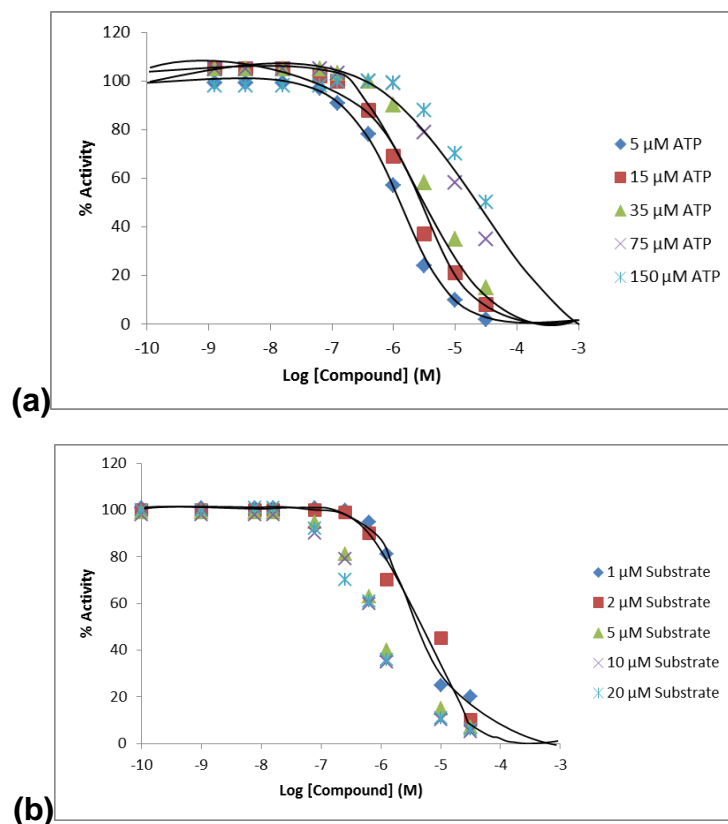


Figure 2.6. IC_{50} curves at different ATP concentrations **(a)** or substrate concentrations **(b)** from plotting slopes (velocities) of progress curves relative to each DMSO control for **BZD-29** against ROCK1. Experiments performed by Reaction Biology Corp.

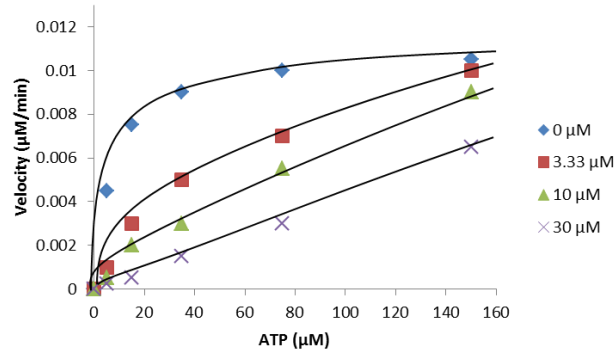
Although K_i values can be obtained by the traditional graphical method, global fit is more accurate. The traditional graphical method puts excessive weight on higher concentrations of inhibitor so that low activities are inaccurate. Global fit, however, puts weight on all data points equally, and is not affected to the same extent by small activities⁶¹. When GraFit performs a global fit, the “Mixed Inhibition” equation (**Equation 2.2**) is used to obtain K_i , so that all variations of competition, including competitive, uncompetitive, noncompetitive, and mixed inhibition, are considered in the analysis⁶¹. All possible mechanisms were fitted to the dependence of ROCK activity with respect to ATP or substrate. The global fitting function then analyzed multiple data sets

simultaneously to generate the one (global) best-fit value of parameters for all of the data sets⁶². Here, v is velocity, $[S]$ is substrate (or ATP) concentration, $[I]$ is inhibitor concentration, K_i is inhibitor affinity for enzyme, and K_i' is inhibitor affinity for the enzyme/ATP complex.

$$v = \frac{V_{\max}[S]}{K_m \left(1 + \frac{[I]}{K_i} \right) + \left(1 + \frac{[I]}{K_i'} \right) [S]}$$

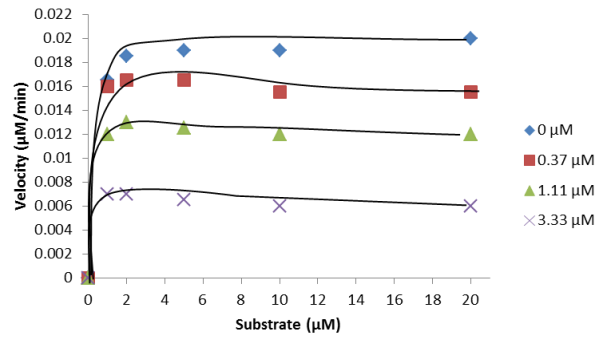
Equation 2.2. The “Mixed Inhibition” equation for global fit⁶¹.

The results of global fit are shown in **Figure 2.7**. For ATP, the high number (infinity) of the K_i' value (**Figure 2.7, a**) means almost no inhibitor affinity for the enzyme/ATP complex, which results in purely competitive inhibition for the ATP binding sites of ROCKI and ROCKII with K_i values of 1.7 μM and 1.4 μM , respectively. In contrast, for substrate, the high K_i value (infinity) means almost no inhibitor affinity for the enzyme alone and the compound prefers to bind the enzyme/substrate complex, which results in uncompetitive inhibition for the substrate binding sites of ROCKI and ROCKII, with K_i' values of 2 μM and 1.5 μM , respectively.



Parameter	Value	Std. Error
V_{max}	0.0123	0.0006
K_m	11.2161	2.3306
K_i	1.6901	0.3408
K_i' value	7.06E18	0.0000

(a)



Parameter	Value	Std. Error
V_{max}	0.0197	0.0003
K_m	0.1188	0.0311
K_i	8.57E23	0.0000
K_i' value	2.0030	0.0932

(b)

Figure 2.7. Global fit of Michaelis-Menten plots for **BZD-29** with ROCK1 in the presence of varying ATP concentrations (a) or substrate concentrations (b). Experiments performed by Reaction Biology.

Taken together, these results show that the inhibition of ROCKI and ROCKII by **BZD-29** is not time-dependent but competitive with respect to their ATP binding sites and uncompetitive with respect to their substrate binding sites.

Lead optimization. Due to the accessibility (synthetically and commercially) of diverse isatoic anhydrides, or anthranilic acid precursors, for A ring modification and various heterocycles for C ring modifications, especially compared to substituted phenylalanines necessary for B ring substitution, the A and C rings were chosen for substitution to probe the physicochemical properties which enhance binding and/or specificity for one ROCK isozyme over the other (**Figure 2.8**).

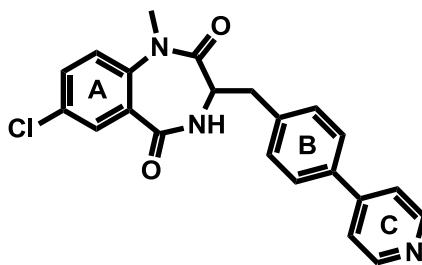
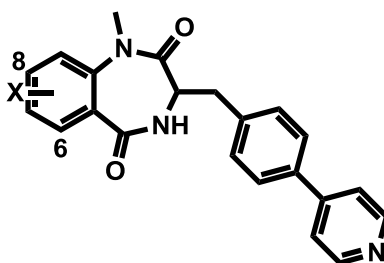


Figure 2.8. Naming scheme of rings of **BZD-29**.

Although some A ring modifications of **BZD-29** have been studied previously (**Tables 2.3** and **2.4**), this data was limited⁵⁵. As shown in **Table 2.3**, the chlorine substituent was previously migrated successively to different positions on the A ring. All compounds, with the exception of (*R*)-**BZD-94**, were similar in potency, indicating that the position of the chlorine does not affect activity due to a lack of close contact with ROCKII. **Table 2.4** represents analogs with varying A7 substituents; all compounds inhibit ROCKII with similar potency, confirming the hypothesis that this ring is not in close contact with ROCKII in the binding pocket and demonstrating the lack of a specific

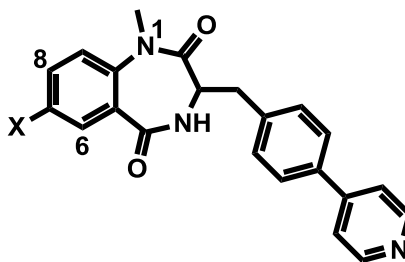
interaction between the A7 chlorine and the enzyme. The results shown in **Table 2.4** do, however, highlight differences in ROCKII selectivity among the molecules. Therefore, although the functional group at A7 did not affect ROCKII activity, it did appear to contribute to isoform selectivity.

Table 2.3. Inhibition data for BZD analogs with varying chlorine locations on the A ring⁵⁵.



R enantiomer			
BZD	X	ROCKI IC ₅₀ (μM)	ROCKII IC ₅₀ (μM)
94	6-Cl	>10	14.4
29	7-Cl	>10	1.1
87	8-Cl	>10	0.8
92	9-Cl	>10	1.0
S enantiomer			
BZD	X	ROCKI IC ₅₀ (μM)	ROCKII IC ₅₀ (μM)
94	6-Cl	>10	0.86
29	7-Cl	>10	0.52
87	8-Cl	>10	2.0
92	9-Cl	>10	2.0

Table 2.4. Inhibition data for BZD analogs with various substituents at position 7 of the A ring⁵⁵.



BZD	X	IC ₅₀ ROCKI (μM)	IC ₅₀ ROCKII (μM)	ROCKII Selectivity*
29	Cl	>30	0.75	>40
103	F	10	0.6	16.7
78	H	3	0.5	6
101	CH ₃	10	0.7	14.3
107	OCH ₃	10	0.5	20

*ROCKII Selectivity: ROCKI IC₅₀/ROCKII IC₅₀

These data were intriguing, since few inhibitors (SLx-2119 and SR3677) to date exhibit selectivity for the ATP-binding site of the kinase domain of a single ROCK isoform due to a high degree of conservation in this region (92% sequence identity). This result was investigated further by analyzing two well-known, equipotent inhibitors of the ROCK enzymes, Fasudil (IC₅₀: ROCKI= 300 nM, ROCKII= 286 nM) and Y-27632 (IC₅₀: ROCKI= 150 nM, ROCKII= 300 nM), in the same assay protocol which had previously reported isoform selectivity by **BZD-29**. The results in **Table 2.5** show levels of inhibition of ROCKII by both compounds which are in agreement with literature values; however, the inhibition of ROCKI by both inhibitors is far less than reported values and, as a result, both appear to be significantly selective (> 50-fold) for ROCKII.

Table 2.5. Inhibition data for known ROCK inhibitors assayed by Millipore protocol.

Compound	ROCKI (nM)	ROCKII (nM)	Selectivity for ROCKII*
Fasudil	14609	214	68.3
Y-27632	6649	129	51.5

*ROCKII Selectivity: ROCKI IC₅₀/ROCKII IC₅₀

These results prompted a closer inspection of the protocol of the assay (conducted by Millipore) as compared to other reported assays of ROCKI and ROCKII.

Table 2.6 lists various parameters of a selection of several such protocols and the vendors which conduct each⁵⁷. Although some variability is to be expected, the observed K_m for ATP for ROCKI is significantly higher (73 μM) in the Millipore protocol than that of other assays (1.9-10 μM), indicating an apparent reduction in the affinity for ATP by the kinase due to diminished catalytic activity.

Table 2.6. Protocols for kinase assays conducted by various vendors⁵⁷.

Vendor	Type of Assay	Assay Separation	Substrate	ROCKI			ROCKII		
				Enzyme	μM ATP K _m	μM Substrate Used	Enzyme	μM ATP K _m	μM Substrate Used
Millipore	³³ P	Filter Bind	S6 substrate	h17-535	73	30	h11-552	15	30
Carna Biosciences	Caliper	Mobility Shift	LIMKtide	h1-477	3.1	1	h1-553	7.4	1
Chem Partners	Caliper	Mobility Shift	ProfilerPro P1	h1-477	3.6	3	h1-553	5.3	3
Reaction Biology	³³ P	Hot Spot, Filter	S6 substrate	h1-535	10	20	h5-554	15	20
Khandekar	³³ P	Filter Bind	Biotin peptide	h3-543	1.9	1	---	---	---

One possible reason for this disparity lies in the ROCKI enzyme construct used by Millipore. As **Table 2.6** shows, the Millipore enzyme begins at residue 17 while all other constructs begin with residue 1 or 3. The region of ROCK between residues 1 and 17 lies proximal to the N-terminal extension and comprises an alpha helix near the

capped helix-bundle (CHB) referenced in Chapter 1 (**Figure 2.9**). By determining the oligomerization states of full-length ROCKII as well as truncated constructs (lacking portions of the N-terminal extension) using light-scattering and analytical ultracentrifugation studies, Doran et al. demonstrated that the CHB is particularly important to the homodimerization of ROCK and that its destabilization leads to a predominance of monomeric ROCK and a resultant 50 to 80-fold increase in ATP K_m as well as a 120-fold increase in the K_i of Y-27632⁵⁸. **Table 2.6** indicates that a region contained in residues 3-17 may be important to the oligomerization state of ROCKI, possibly through stabilization of the CHB, and its absence results in the approximately 24-fold increase in ATP K_m for ROCKI in the Millipore assay protocol compared to the protocols of alternate vendors. The ATP K_m for ROCKII in the Millipore assay, however, is more similar to the K_m values of other vendors, indicating that the enzymes adopt the same oligomeric state. Due to the evidence that dimerization has a significant effect on ROCK kinase activity, in order to accurately compare the effect of an inhibitor against ROCKI to its activity against ROCKII, for a selectivity determination, both enzymes should exist in the same oligomeric state. Because a main focus of this project involved determining the selectivity of the inhibitors for the ROCK isoforms, the Reaction Biology protocol was chosen for all further assays to ensure ROCKI and ROCKII both existed in similar oligomeric states and because this assay also meets the optimal criteria for assessing ROCK activity, addressed in the introduction of this chapter.

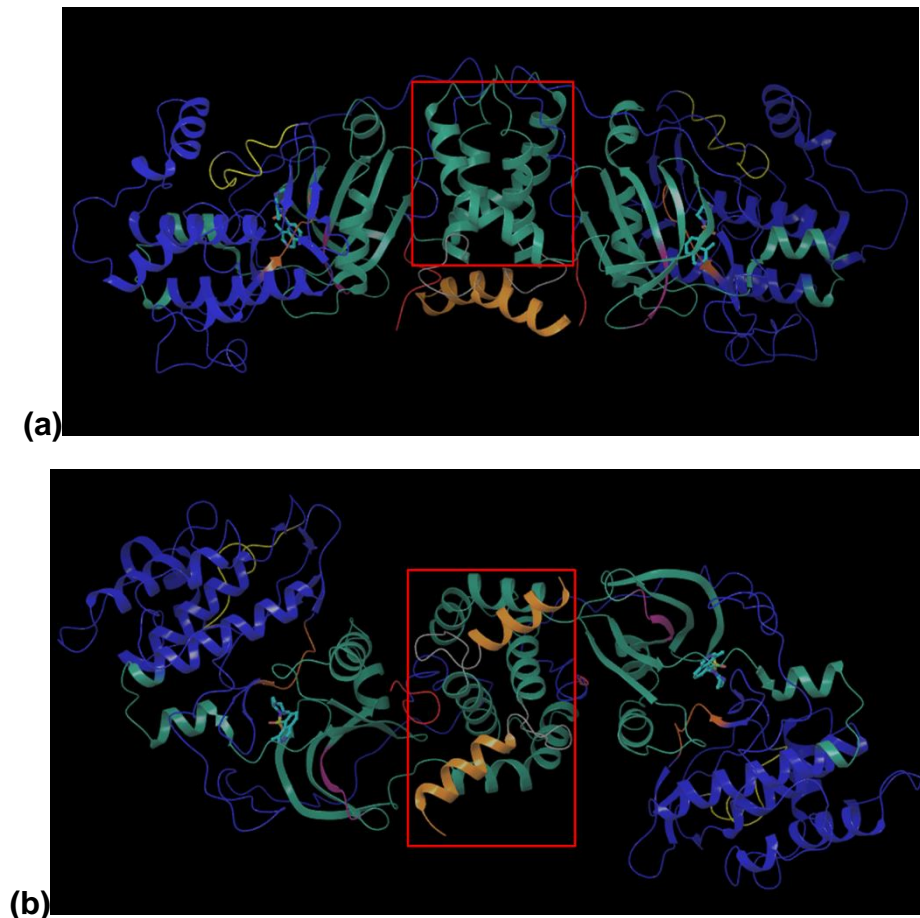


Figure 2.9. Dimeric structure of the Rho-kinase protein consisting of the kinase domain and the N- and C-terminal extensions; bound ATP-competitive inhibitors are shown as sticks (cyan) for reference. **(a)** Ribbon diagram of the dimer structure of Rho-kinase protein looking down the 2-fold axis. The capped helix-bundle (CHB) is boxed in red and residues 1-17 are displayed as an orange α -helix below. **(b)** View of the Rho-kinase dimer in an orthogonal direction with the CHB and residues 1-17 indicated as in **(a)** (PDB: 3D9V)⁶³.

Inhibition results reported in biochemical assays that exclude the C-terminus of ROCK may also not accurately reflect the levels of inhibition which would be experienced with full-length ROCK enzymes, as in the cellular environment. The C-termini of related kinases have been shown to have significant effects on the activity of inhibitors. For instance, in 2005, Barnett et al. reported the identification of an inhibitor of the Akt1 and Akt2 kinases, enzymes belonging to the same kinase family (AGC) as

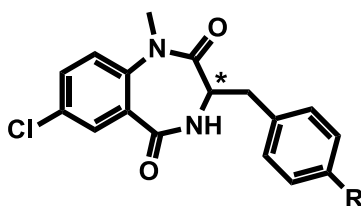
the ROCK proteins, with an IC₅₀ of 58 nM and 210 nM against Akt1 and Akt2, respectively. However, Akt mutants lacking the pleckstrin homology (PH) domain of the C-terminus, were not inhibited⁵⁹.

BZD-29 has been confirmed to selectively inhibit the ROCKII isoform in cells. However, in the biochemical assays utilizing PH-domain lacking ROCK constructs, **BZD-29** is equipotent against both ROCK enzymes. The C-terminus of full-length ROCKI therefore appears to have a significant effect on the selectivity of this inhibitor. In light of this observation, the ROCK isoform selectivity profiles of **BZD-29** analogues, as reported by the biochemical assay, were related to the ROCK enzyme selectivity of **BZD-29** in the same assay and were not interpreted as accurate representations of the levels of selectivity which would be observed with these inhibitors against cellular ROCK kinases. For example, if a hypothetical compound, **X**, were 2-fold more potent against ROCKII versus ROCKI in the biochemical assay, although this would generally not be considered a significant degree of selectivity, because **BZD-29** is equipotent against both isoforms in these experiments, compound **X** would be interpreted as being 2-fold more selective for ROCKII than **BZD-29**. Since **BZD-29** has demonstrated physiologically relevant selectivity for ROCKII in cells, it would be expected that compound **X** should enhance this effect and therefore would be significantly selective in cells.

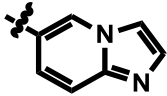
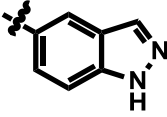
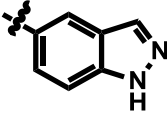
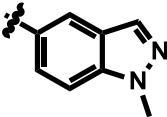
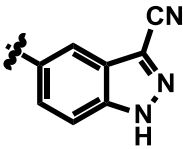
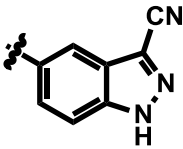
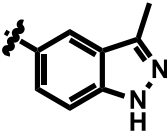
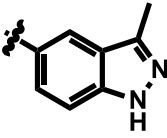
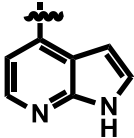
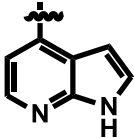
*Modification of the C-ring of **BZD-29***. Production of analogs proceeded with incorporation of both A ring or C ring modifications. As mentioned previously, the C ring was altered to determine the optimal orientation of the hydrogen bond accepting nitrogen, to explore whether a bi-dentate bond might be formed between the C ring and

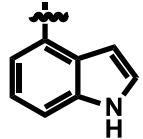
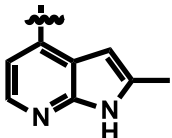
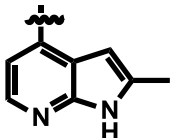
the hinge region, and to avoid the cytochrome P450 inhibition noted to be problematic for pyridine-based inhibitors. To this effect, the inhibition results of a selection of analogs incorporating various C rings is shown in **Table 2.7**.

Table 2.7. Inhibition results for a selection of **BZD-29** analogs with varied C rings.



Compound	R	Rel. IC ₅₀ (R1) ^{a,b}	Rel. IC ₅₀ (R2) ^c	R2 Select. ^d
<i>rac</i> -BZD-29 ^e		1x	1x	1.01
<i>rac</i> -1		0.10x	0.10x	1.0
<i>rac</i> -2		0.10x	0.10x	1.0
<i>rac</i> -3		0.58x	0.47x	0.82
<i>rac</i> -4		0.24x	0.15x	0.63
<i>rac</i> -5		0.10x	0.10x	1.0

<i>rac</i> -6		0.21x	0.18x	0.85
(<i>S</i>)-7 ^f		7.57x	5.15x	0.68
(<i>R</i>)-7 ^g		13.02x	5.59x	0.43
<i>rac</i> -8		0.10x	0.10x	1.0
(<i>S</i>)-9		0.10x	0.10x	1.0
(<i>R</i>)-9		0.10x	0.10x	1.0
(<i>S</i>)-10		3.20x	1.78x	0.56
(<i>R</i>)-10		2.50x	1.93x	0.78
(<i>S</i>)-11		14.0x	16.59x	1.19
(<i>R</i>)-11		27.94x	36.86x	1.33

<i>rac</i> -12		0.10x	0.10x	1.0
(<i>S</i>)-13		0.10x	0.10x	1.0
(<i>R</i>)-13		0.10x	0.10x	1.0

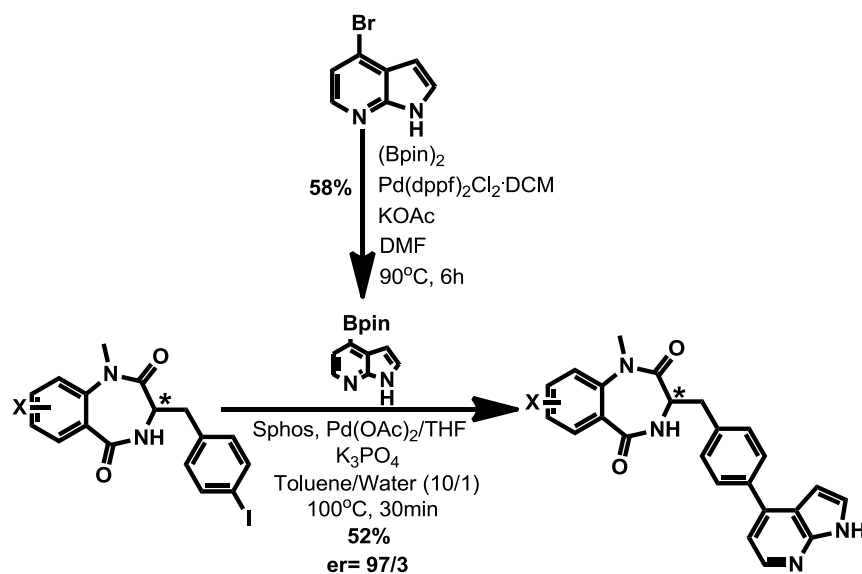
a: rel. IC₅₀= *rac*-**BZD-29** IC₅₀ (ROCKI= 3093.5 nm +/- 139.3, ROCKII= 3075.0 nm +/- 881.1)/ analogue IC₅₀, **b:** R1= ROCKI, **c:** R2= ROCKII, **d:** R2 Select.= Selectivity for ROCKII (=R1/R2) **e:** *rac*= racemate, **f:** (*S*)= >95% (*S*)-enantiomer, **g:** (*R*)= >95% *R*-enantiomer.

The first modification to show improved inhibition over **BZD-29** was the indazole (compounds (**S**)-7 and (**R**)-7). To probe the interactions necessary for its activity, the indazole was then methylated to give analogue *rac*-8. This change completely abolished inhibition, suggesting either that the hydrogen of the this amine was primarily responsible for inhibition or that the methyl group produces as significant steric clash with the region of the binding pocket in which it resides. A size restriction seems to be supported by the complete lack of inhibition by compounds (**S**)-9 and (**R**)-9, however, analogues (**S**)-10 and (**R**)-10 (indazoles methylated at C3) regained activity, albeit at a reduced potency compared to compounds (**S**)-7 and (**R**)-7. Rationalization of these results will be presented in Chapter 3.



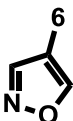
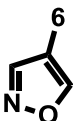
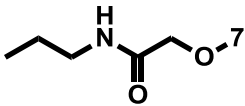
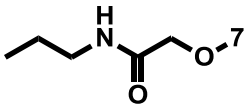
Next, the azaindoles of entries (**S**)-11 and (**R**)-11 showed improved inhibition of both isozymes. *rac*-12 was then assayed to probe the interactions necessary for azaindole inhibition and clearly demonstrated that the pyridine nitrogen makes a critical

contact with the binding pocket. Finally, the hypothesis that a substantial size restriction near the hinge region of the binding pocket is supported by the lack of inhibition by **(S)-13** and **(R)-13**, in which C2 of azaindole is methylated. From analysis of these assay results, the unsubstituted azaindole (**(S)-11** and **(R)-11** in **Table 2.7**) was chosen as the optimal C ring.

Since diversity of the C ring was no longer necessary, to expedite analog production, the Suzuki coupling partners were swapped again to reduce the number of synthetic steps (**Scheme 2.3**). Here, the borylated azaindole could be produced on a multi-gram scale so that benzodiazepines bearing diversity on the A ring could be synthesized rapidly and without additional concern over the lability of the substituent during the borylation step.



Scheme 2.3. Optimized Suzuki conditions for azaindole-substituted 1,4-benzodiazepine analogs.

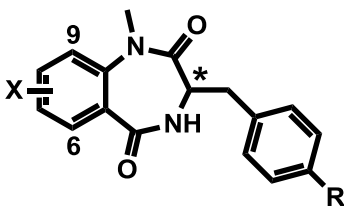
(R)-17		4.8x	13.4x	2.78
(S)-18		19.3x	18.0x	0.94
(R)-18	6-F	10.6x	10.0x	0.95
(S)-19		3.9x	4.1x	1.05
(R)-19		1.9x	1.9x	1.0
<i>rac</i> -20 ^g	8,9-Cl	20.3x	23.0x	1.14
(S)-21		168.7x	110.0x	0.66
(R)-21		3.6x	3.0x	0.84
(S)-22	7-OH	31.1x	63.2x	2.04
(R)-22		2.0x	4.8x	2.39
(S)-23		4.0x	10.1x	2.56
(R)-23		2.8x	7.2x	2.60
(S)-24	8-Br	9.9x	16.4x	1.67
(R)-24		12.1x	15.2x	1.26
(S)-25	H	43.7x	36.5x	0.84
(R)-25		51.0x	48.5x	0.96
(S)-26	9-OCH ₃	31.1x	32.1x	1.04
(R)-26		8.3x	11.2x	1.36

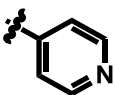
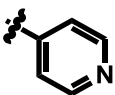
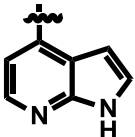
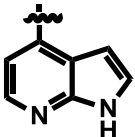
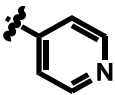
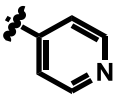
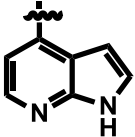
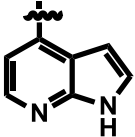
(S)-28		14.7x	10.7x	0.73
	6-Br			
(R)-28		14.7x	11.1x	0.76
(S)-29		94.7x	69.3x	0.74
	9-Br			
(R)-29		20.5x	15.0x	0.73
(S)-30		195.2x	109.2x	0.56
	9-F			
(R)-30		27.9x	19.6x	0.71
(S)-31		6.0x	7.0x	1.17
	7-NO₂			
(R)-31		8.5x	10.2	1.21
(S)-33		11.0x	14.4x	1.32
	9-NO₂			
(R)-33		4.6x	6.5x	1.42

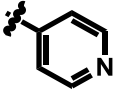
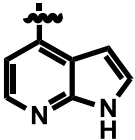
a: rel. IC₅₀= *rac*-**BZD-29** IC₅₀ (ROCKI= 3093.5 nm +/- 139.3, ROCKII= 3075.0 nm +/- 881.1)/ analogue IC₅₀, **b:** R1= ROCKI, **c:** R2= ROCKII, **d:** R2 Select.= Selectivity for ROCKII (=R1/R2) **e:** (S)= >95% (S)-enantiomer, **f:** (R)= >95% R-enantiomer, **g:** rac= racemate.

It was noted with the production of only a few azaindole-based analogs that the SAR of the A ring was different from that of the pyridine-based inhibitors (**Table 2.9**)⁵⁵. This demonstrated that the local environment experienced by the A ring of the azaindole-based inhibitors was somewhat different than that experienced by the A ring of the pyridine-substituted compounds. Essentially, these data show that the inhibitor has reoriented in the ATP binding cleft.

Table 2.9. Comparison of relative IC₅₀'s of a selection of pyridine-based analogs to **BZD-29** and relative IC₅₀'s of azaindole-based analogs to compound **11**.



Compound	R	X	Rel. IC ₅₀ (R1)	Rel. IC ₅₀ (R2)
(S)-BZD-29		7-Cl	1.0x ^a	1.0x
(R)-BZD-29		7-Cl	1.0x ^b	1.0x
(S)-11		7-Cl	1.0x ^c	1.0x
(R)-11		7-Cl	1.0x ^d	1.0x
(S)-BZD-87		8-Cl	1.0x ^a	0.26x
(R)-BZD-87		8-Cl	1.0x ^b	1.4x
(S)-14		8-Cl	1.2x ^c	1.2x
(R)-14		8-Cl	0.6x ^d	0.4x

(S)-BZD-107		7-OCH ₃	3.0x ^a	1.0x
(S)-16		7-OCH ₃	0.9x ^c	0.8x

a: (S)-BZD-29 IC₅₀/ analogue IC₅₀, b: (R)-BZD-29 IC₅₀/ analogue IC₅₀, c: (S)-11 IC₅₀/ analogue IC₅₀, d: (R)-11 IC₅₀/ analogue IC₅₀.

To confirm that the azaindole-based inhibitors still bound to the ATP-binding cleft of ROCK in the same manner as did **BZD-29**, identical mechanism of action studies to those performed with **BZD-29** were repeated for compound **11**. Again, the results showed that inhibition of ROCKI and ROCKII by analog **11** was not time-dependent, but competitive with respect to ATP ($K_i = 134$ nM for ROCKI, 85.5 nM for ROCKII) and uncompetitive with respect to substrate.

Structure Activity Relationship (SAR) models. Next, a manual Hansch analysis was conducted to analyze the data from the biochemical assays shown in **Table 2.8**. In formulating structure activity relationship (SAR) models, it was considered that the enantiomers of the inhibitors may experience different orientations within the binding pocket, that may lead to different recognition patterns between the inhibitor and the enzyme and, subsequently, different overall effects. For example, it has recently been observed that L-ATP actually inhibits mammalian DNA primase, an enzyme activated by D-ATP to synthesize RNA primers on the leading- and the lagging-strands of DNA, in the course of semi-conservative DNA replication⁶⁰. Although this implies that both L- and D-ATP are recognized by the active site of the enzyme, their vastly different effects signify that they experience different interactions.

Therefore, separate SAR models were formulated for each enantiomer of the current analog series, at each position of the A ring. Due to the number of models needed to accomplish this, the manual Hansch analysis was specifically chosen for model preparation, due to its requirement of as few as 5 analogs. Additionally, descriptors such as molecular weight (MW) and calculated molar refractivity (CMR) were also used to evaluate steric effects while polar surface area (PSA) was used to determine the effects of each substitution on permeability. Representative charts of some important associations observed are depicted in **Figure 2.10**. The models developed from these associations are depicted in **Figure 2.11**.

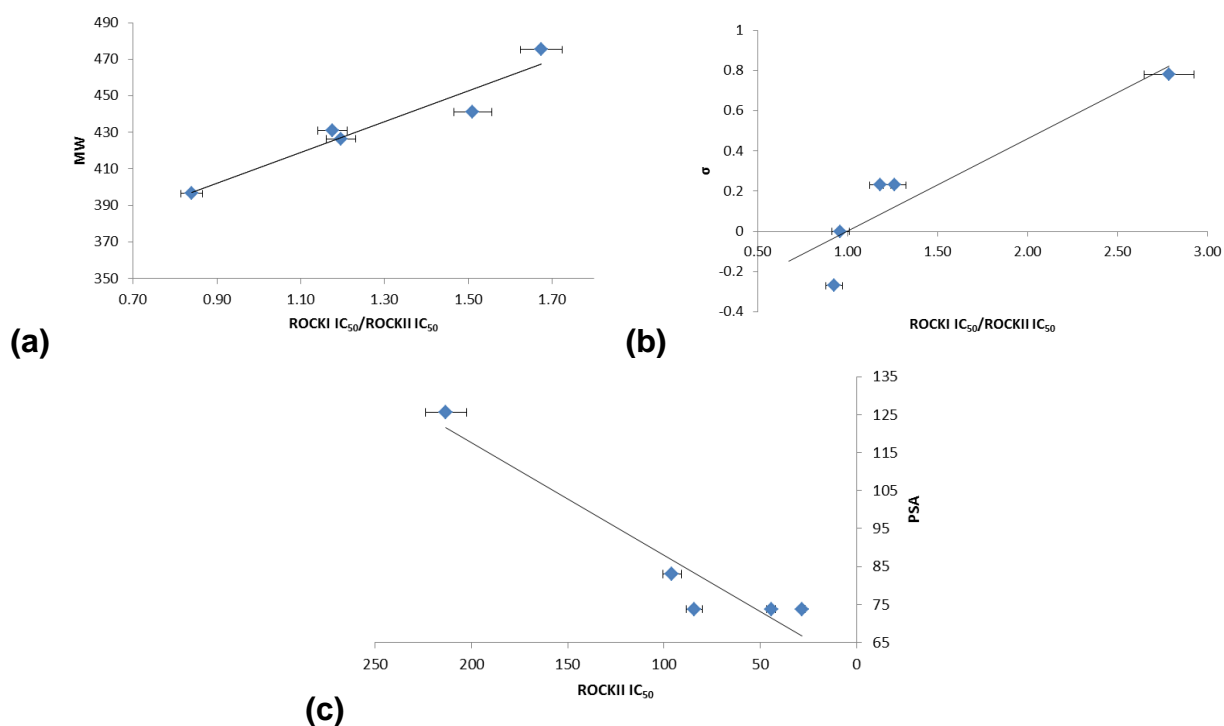


Figure 2.10. Representative associations between physicochemical parameters of substituents of the A ring and inhibitor IC₅₀ values for ROCKII or selectivity for ROCKII (defined as ROCKI IC₅₀/ROCKII IC₅₀). **(a)** Correlation of ROCKII selectivity with (S)-A8 substituent molecular weight (MW). **(b)** Correlation of ROCKII selectivity with (R)-A8 substituent σ values in the manual Hansch analysis. **(c)** Correlation of ROCKII IC₅₀ values with (S)-A9 substituent polar surface area (PSA). Values for R² >0.80 were considered well-correlated data.

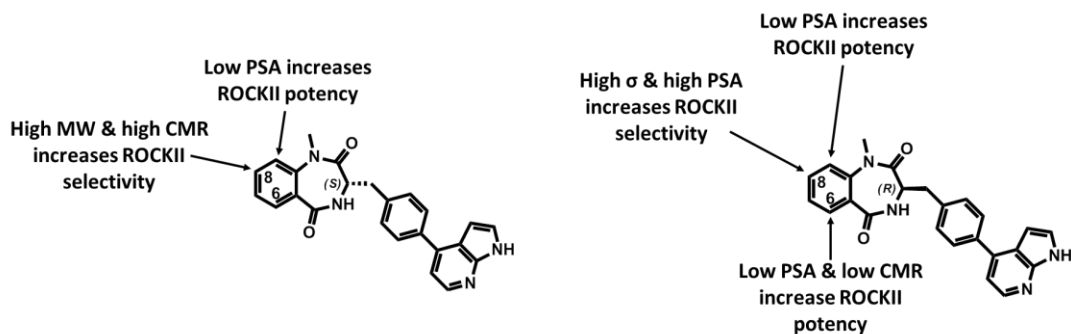


Figure 2.11. Summary of associations between descriptors and enhanced potency or selectivity for ROCKII (defined as $\text{ROCKI IC}_{50}/\text{ROCKII IC}_{50}$) for the enantiomers of azaindole-based analogs.

As shown in **Figure 2.11**, for the *S* enantiomer, raising the molecular weight and molar refractivity at position A8, essentially increasing the size of the substituent, was associated with enhanced selectivity for ROCKII over ROCKI, while lowering the polar surface area at A9 led to an increase in inhibitor potency for ROCKII. In the case of the *R*-enantiomer, reducing the polar surface area at A6 and A9 also effected an increase in potency, however an increase in the PSA at A8 was indicated to enhance ROCKII selectivity. Additionally, lowering the molar refractivity of the substituent at A6 also enhanced potency, resulting in a total prediction that a small, less-polar substituent is optimal at this site. At A8 of the *R*-enantiomer, the manual Hansch analysis indicated that an increase in selectivity for ROCKII over ROCKI was associated with an increase in σ . This indicated that electron rich motifs such as 7- CF_3 & 8-Cl, 7- CF_3 & 8- NO_2 , 8- CF_3 , 7,9- Cl_2 , 8- $\text{c-C}_5\text{H}_9$, and 8- $\text{c-C}_6\text{H}_{11}$ have potential to improve ROCKII selectivity, or they should at least be equally selective.

MATERIALS AND METHODS

General Procedures (Biology)

Millipore ROCK-I (h) inhibition assay. In a final reaction volume of 25 μ L, ROCKI (human, amino acids 17-535) (5-10 mU) was incubated with 8 mM MOPS pH 7.0, 0.2 mM EDTA, 30 μ M KEAKEKRQEIQAKRRRLSSLRASTSKSGGSQK, 10 mM magnesium acetate and [γ -³²P-ATP] (specific activity approx. 500 cpm/pmol, concentration as required). The reaction was initiated by the addition of the MgATP mix. After incubation for 40 minutes at room temperature, the reaction was stopped by the addition of a 3% phosphoric acid solution (5 μ L). The reaction (10 μ L) was then spotted onto a P30 filtermat and washed three times for 5 min in 75 mM phosphoric acid and once in methanol prior to drying and scintillation counting.

Millipore ROCK-II (h) inhibition assay. In a final reaction volume (25 μ L), ROCKII (human, amino acids 11-552) (5-10 mU) was incubated with 50 mM Tris pH 7.5, 0.1 mM EGTA, 30 μ M KEAKEKRQEIQAKRRRLSSLRASTSKSGGSQK, 10 mM magnesium acetate and [γ -³²P-ATP] (specific activity approx. 500 cpm/pmol, concentration as required). The reaction proceeded as described above.

Reaction Biology ROCK-I (h) inhibition assay. *In vitro* activities of inhibitors were determined at Reaction Biology Corporation using the “HotSpot” assay platform. The ROCK-I kinase (0.5 nM, h1-535 expressed in insect cells with an N-terminal GST tag), along with the long S6 kinase substrate peptide as substrate, was prepared with 20 mM

Hepes pH 7.5, 10mM MgCl₂, 1 mM EGTA, 0.02% Brij35, 0.02 mg/ml BSA, 0.1 mM Na₃VO₄, 2 mM DTT, and 1% DMSO. Compounds were delivered into the reaction, followed ~20 minutes later by addition of a mixture of ATP (Sigma) and ³³P ATP (PerkinElmer) to a final concentration of 10 μM. Reactions were carried out at 25°C for 120 minutes, followed by spotting of the reactions onto P81 ion exchange filter paper (Whatman). Unbound phosphate was removed by extensive washing of filters in 0.75% phosphoric acid. After subtraction of background derived from control reactions containing inactive enzyme, kinase activity data was expressed as the percent remaining kinase activity in test samples compared to vehicle (dimethyl sulfoxide) reactions. IC₅₀ values and curve fits were obtained using Prism (GraphPad Software)⁵⁴.

Reaction Biology ROCK-II (h) inhibition assay. ROCK-II kinase inhibition assays were performed as described above with ROCK-II kinase (1.0 nM, h5-554 expressed in baculovirus in Sf9 insect cells with an N-terminus GST-tag).

Reaction Biology Mechanism of Action Studies. Compounds: Powder samples dissolved in DMSO to make 10 mM stock DMSO. Kinase reaction buffer: 20 mM HEPES-HCl, pH 7.5, 10 mM MgCl₂, 1 mM EGTA, 0.02% Brij35, 0.1 mM Na₃VO₄, 0.02 mg/mL BSA, 2 mM DTT, and 1% DMSO. Enzymes: ROCKI, recombinant human protein, catalytic domain (amino acids 1-535; accession #NP_00397), GST-tagged, expressed in insect cells, Mw= 89.7 kDa; ROCKII, recombinant human protein (amino acids 5-554; accession #NM_004850), N-terminal GST-tagged, expressed in Sf9 cells, Mw= 88 kDa. Substrate: long S6 kinase substrate peptide, [[KEAKEKRQEIQAKRRRLSSLRASTSKSGGSQK], Mw= 3,630 Da. Reaction conditions: 0.5 nM ROCKI, 20 μM Long S6 kinase substrate peptide, and varied ATP; 1

nM ROCKII, 20 μ M Long S6 kinase substrate peptide, and varied ATP. Experimental procedures: the kinase assays were performed at room temperature. The compounds were added in 10-dose IC₅₀ mode into enzyme/substrate mixture using acoustic technology, and incubated for 20 min to ensure the compound was equilibrated and bound to the enzyme. Then 5 concentrations of ATP were added to initiate the reaction. The activity was monitored every 5-15 min for time course.

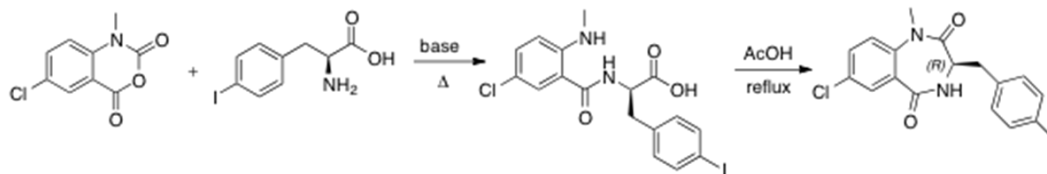
General Procedures (Chemistry)

All solvents and substrates used in synthesis were acquired from commercial sources and were used without further purification. The progress of each reaction was monitored by thin layer chromatography (TLC). TLC was performed using glass plates obtained from EMD Chemicals Inc., which were pre-coated with a 0.25-mm-thick layer of Silica Gel 60 F254. The plates were visualized by UV quenching (254 nm). All compounds were routinely checked by TLC to detect decomposition. Additionally, reaction progress was also determined by mass using a Micromass LCT time-of-flight mass spectrometer with electrospray. Column chromatography was performed by the Biotage Flashmaster II purification system. Crude reaction mixtures were dissolved in minimal solvent and dried onto the silica gel of an appropriately sized Biotage Isolute pre-packed silica gel column under vacuum. Chromatography was performed at the following flow rates: 12 mL/min (2 g column), 18 mL/min (5 g column), 23 mL/min (10 g column), 25 mL/min (20g column), 40 mL/min (50 g column). Samples were detected by a Knauer UV detector at 254 nm. Solvent removal was accomplished with the use of a Buchi rotary evaporator and residual solvent was removed using a high vacuum oil

pump (ca. 0.1 mm Hg). Enantiomeric purity was evaluated using a Chiracel OJ-H column, eluting with 100% MeOH on a Waters HPLC system. Proton and carbon nuclear magnetic resonance (^1H and ^{13}C NMR) spectra were recorded in $\text{DMSO-}d_6$, on a Varian UnityINOVA spectrometer operating at 500 MHz. Data are reported as follows: chemical shift (on the δ scale in parts per million downfield from tetramethylsilane (δ 0.00) using the residual solvent as an internal standard), multiplicity (s= singlet, d= doublet, dd= doublet of doublets, ddd= doublet of doublet of doublets t= triplet, qt= quartet of triplets, qdt= quartet of doublet of triplets, q= quartet, qn= quintet, sx= sextet, ABq= quartet, m= multiplet, b= broad), integration, coupling constant (J in Hz), and assignment (referenced to the numbering scheme of the associated figures). The internal reference peak was δ 2.50 for $(\text{CH}_3)_2\text{SO}$. Chemical shifts for ^{13}C NMR are reported relative to the internal reference solvent peak (δ 39.5 for $(\text{CD}_3)_2\text{SO}$). Deuterated NMR solvents were purchased from Cambridge Isotopes and used without further purification. All NMR spectra were measured at ambient probe temperature. Mass spectra (MS) were measured on a Micromass LCT Time-of-Flight mass spectrometer with Electrospray. Samples were dissolved in a mixture of methylene chloride/methanol and aliquoted in a methanol/water/formic acid solution.

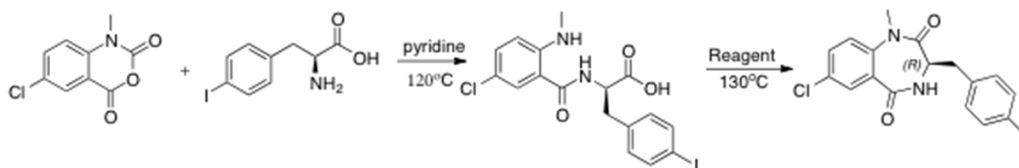
Optimization of the **BZD-29** synthetic route:

(Optimization of Coupling Step):



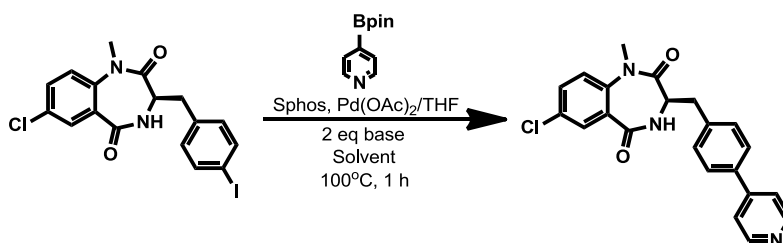
Base	Solvent	Temp. (°C)	Yield (%)	er (%R:%S)
Et ₃ N	AcN/H ₂ O	50	71%	91:9
DIEA	AcN/H ₂ O	50	69%	91:9
Pyridine	THF, DMF, (neat)	50, 80, 100	No or min. react.	---
Pyridine	(neat)	120	82%	97:3
2-Picoline	(neat)	120	72%	89:11
2,6-Lutidine	(neat)	120	66%	84:16

(Optimization of Cyclization Step):

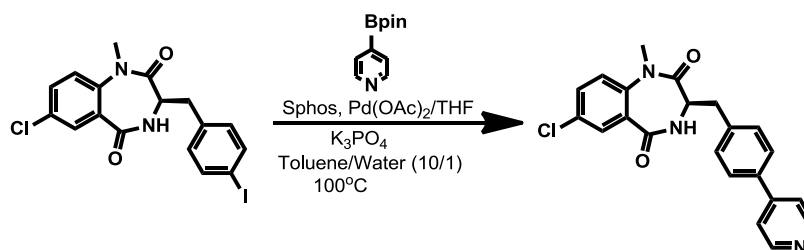


Reagent	Yield	er (%R:%S)
AcOH	82%	97.4 : 2.6
DMSO	84%	95.1 : 4.9
HCl(g)/DMF	63%	93.8 : 6.2

(Optimization of Suzuki Step):



Base	Solvent (mL)	Catalyst (mol%)	Yield (%)	er (%R:%S)
KOH	Toluene/H ₂ O (1:1)	3	46.1	90:10
Na ₂ CO ₃	Toluene/H ₂ O (1:1)	3	34.9	92:8
K ₂ CO ₃	Toluene/H ₂ O (1:1)	3	36.0	93:7
NaOH	Toluene/H ₂ O (1:1)	3	48.6	89:11
K ₃ PO ₄	Toluene/H ₂ O (1:1)	3	42.2	97:3
K ₃ PO ₄	Toluene/H ₂ O (2:1)	3	48.6	97:3
K ₃ PO ₄	Toluene/H ₂ O (10:1)	3	64.7	97:3
K ₃ PO ₄	Toluene/H ₂ O (10:1)	1	64.3	97:3



Time (h)	Yield (%)	er (%R:%S)
0	N.D.	97:3
0.5	64	97:3
1	66	97:3
2	67	95:5
6	69	93:7
12	68	92:8

General Protocol 1 (GP1): Cyclization of Isatoic Anhydride. The appropriate anthranilic acid (1eq) was dissolved along with triphosgene (1eq) in THF (4.3 mL/mmol anthranilic acid) at room temperature with stirring. The mixture was heated to 70°C for 2h and then allowed to cool to room temperature. The mixture was then poured slowly into stirring water, allowed to stir for 10 minutes and the solid precipitate was filtered off. The filter cake was washed 3x with water and allowed to dry over vacuum.

General Protocol 2 (GP2): Methylation of Isatoic Anhydride. Sodium hydride (1.32 eq) was suspended in DMF (1.5 mL/mmol isatoic anhydride) with stirring for 10 minutes. The appropriate isatoic anhydride (1eq) was then dissolved in DMF (1.5 mL/mmol isatoic anhydride) and added to the sodium hydride mixture by cannula with stirring. The mixture was allowed to stir at room temperature for 50 minutes before the dropwise addition of methyl iodide (1.2eq). The mixture was heated to 37°C with stirring for 18h. Additional methyl iodide (0.3eq) was then added and conditions were continued an additional 3h. The mixture was cooled to room temperature before being slowly poured into 1N HCl (3 mL/mL DMF) at 5°C. The suspension was stirred for 10 minutes before the precipitate was filtered off, washed with excess water, and allowed to dry over vacuum.

General Protocol 3 (GP3): Coupling of Isatoic Anhydride with Amino Acid. The appropriate isatoic anhydride (1eq) was dissolved with the appropriate amino acid (D-iodophenylalanine for the production of *R* enantiomers, L-iodophenylalanine for the production of *S* enantiomers, or DL-iodophenylalanine for the production of racemic mixtures) (1.15eq) in pyridine (2 mL/mmol isatoic anhydride) over molecular sieves.

The mixture was refluxed at 120°C for 4 hours before being filtered hot. The molecular sieves were washed with excess ethyl acetate and the filtrate was evaporated to dryness. Excess pyridine was azeotroped with toluene twice and the resultant material was taken to the next step without further process.

General Protocol 4 (GP4): Cyclization of the Benzodiazepine Ring. The resultant material from GP3 was dissolved in acetic acid (4 mL/mmol isatoic anhydride) and refluxed at 130°C for 18 hours. The mixture was then allowed to cool to room temperature before water and ethyl acetate were added. The aqueous layer was slowly and carefully neutralized with saturated sodium bicarbonate solution and extracted twice with ethyl acetate. The organic layers were combined and washed with water and brine before drying over sodium sulfate. The mixture was filtered and evaporated. The resultant material was dissolved in minimal ethyl acetate and passed through a silica plug with excess ethyl acetate. The filtrate was evaporated and taken to the next step without further process.

General Protocol 5 (GP5): Miyaura Borylation. The resultant material (1eq) from GP4 was dissolved along with bispinnacolatodiboron (2eq), potassium acetate (3eq), and [1,1'-Bis(diphenylphosphino)ferrocene]dichloropalladium(II) complex with dichloromethane (7mol%), in degassed DMF. The mixture was heated to 80°C for 6 hours. Xylenes were added to the mixture which was then evaporated in an 80°C rotovap bath to remove as much DMF as possible. Another evaporation cycle with xylenes was performed and the resultant material was taken to the next step.

General Protocol 6 (GP6): Suzuki Coupling. The resultant material from the previous step (1.5eq), in addition to the appropriate halogenated coupling partner (1eq), and potassium phosphate tribasic (2eq) was dissolved in degassed toluene and water (10/1, 2ml/mmol halogenated starting material total). The catalyst solution was prepared freshly by dissolving SPhos (2mol%) and palladium acetate (1mol%) in degassed THF. The catalyst solution was then sonicated for 1 minute before adding 0.1 mL/mmol halogenated starting material to the reaction mixture. The whole mixture was then heated at 100°C with stirring for 1.5h. The mixture was allowed to cool before ethyl acetate was added. The mixture was then passed through a silica plug with excess ethyl acetate.

General Procedure 7 (GP7): TBDMS Deprotection. The appropriate material (1eq) was treated with TBAF in THF (1.0 M, 1.01eq) in THF (4 mL/mmol starting material) at room temperature overnight. The reaction was treated with 1N HCl and extracted 3 times with ethyl acetate. The ethyl acetate was washed with water and brine and evaporated to dryness. The residue was purified by flash chromatography (ethyl acetate/hexanes) to give pure product.

General Procedure 8 (GP8): Acetamide-Hydroxyl Coupling. The appropriate bromo-acetamido compound (1.2eq) was coupled to a hydroxyl compound (1eq) with potassium carbonate (3eq) in DMF (0.41 mL/mmol hydroxyl compound) at 80°C for 21h. The reaction was allowed to cool to room temperature before quenching with saturated, aqueous NH₄Cl. The resulting precipitate was dissolved in DCM, washed with water

and brine and dried. The solvent was evaporated and the resulting material was purified by flash chromatography (ethyl acetate hexanes) to give pure product.

4-(4,4,5,5-tetramethyl-1,3,2-dioxaborolan-2-yl)-1H-pyrrolo[2,3-b]pyridine. 4-bromo-7-azaindole was borylated by the protocol described in GP5.

6-((tert-butyldimethylsilyl)oxy)-1H-benzo[d][1,3]oxazine-2,4-dione. 5-hydroxy isatoic anhydride (1eq) was treated with tertbutyldimethylsilyl triflate (1.7eq) in pyridine (3 mL/mmol isatoic anhydride) at room temperature overnight. The solvent was then evaporated and azeotroped twice with toluene. The resulting material was dissolved in DCM and washed with saturated bicarbonate, brine, and then dried. The resulting material was purified by flash chromatography (Ethyl acetate/hexanes) to give pure 6-((tert-butyldimethylsilyl)oxy)-1H-benzo[d][1,3]oxazine-2,4-dione.

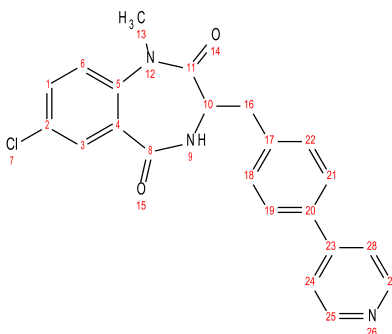
2-bromo-N-propylacetamide. Propylamine (2eq) was treated with 2-bromoacetyl bromide (1eq) in DCM (2.1 mL/mmol 2-bromoacetyl bromide) at 0°C. The reaction was warmed to room temperature and stirred 1 hour. The precipitate was filtered and washed with excess DCM. The filtrate was washed with 2N HCl twice, brine, and dried. The solvent was evaporated to give pure 2-bromo-N-propylacetamide without purification.

*Characterizations of previously prepared **BZD** compounds can be found in their associated reference⁵⁵.

Compound Characterizations

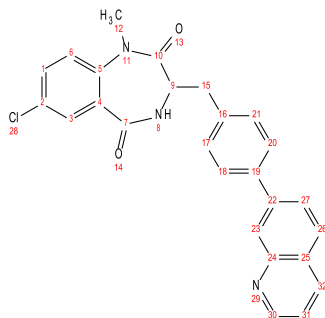
All characterizations were conducted for the racemate of each compound.

7-chloro-1-methyl-3-(4-(pyridin-4-yl)benzyl)-3,4-dihydro-1H-benzo[e][1,4]diazepine-2,5-dione (BZD-29; LDM-2-5)



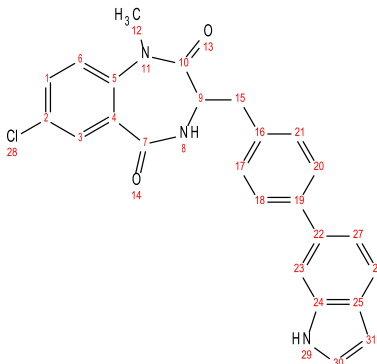
BZD-29 was prepared by GP2 (starting material: 5-chloroisatoic anhydride), GP3, GP4, GP5, and GP6 (reagent: 4-bromopyridine). The resulting crude product was purified by flash chromatography [0-100%(10%MeOH/EA)/hex to provide 7-chloro-1-methyl-3-(4-(pyridin-4-yl)benzyl)-3,4-dihydro-1H-benzo[e][1,4]diazepine-2,5-dione (overall yield= 40.6%) as an off-white solid; R_f= 0.35 (EA); ¹H NMR (500 MHz) (δ/ppm) 3.19 (ddt, 1H, J= 12.3, J= 6.8, J= 1.0, 16), 3.25 (ddt, 1H, J= 12.4, J=6.9, J=1.1, 16'), 3.40 (s, 3H, 13), 5.00 (t, 1H, J=6.8, 10), 7.18 (d, 1H, J=7.6, 6), 7.41 (dt, 2H, J=7.5, J=1.1, 18, 22), 7.50 (dd, 1H, J=7.5, J=2.0, 1), 7.64 (d, 2H, J=7.5, 19, 21), 7.90 (d, 2H, J=5.0, 24, 28), 8.08 (s, 1H, 9), 8.12 (d, 1H, J=2.0, 3) 8.69 (d, 2H, J=5.1, 25, 27); ¹³C NMR (500 MHz) (δ/ppm) 33.7, 37.6, 54.2, 121.4, 123.9, 125.7, 127.9, 128.3, 131.46, 131.5, 132.2, 134.2, 138.0, 140.8, 147.4, 147.9, 168.5, 169.5; Exact Mass (ES): determined mass: 391.1093 u, exact mass: 391.1088 u.

7-chloro-1-methyl-3-(4-(quinolin-7-yl)benzyl)-3,4-dihydro-1H-benzo[e][1,4]diazepine-2,5-dione (rac-1; LDM-2-29)



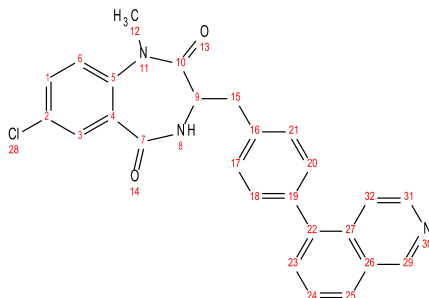
1 was prepared by GP2 (starting material: 5-chloroisatoic anhydride), GP3, GP4, GP5, and GP6 (reagent: 7-bromoquinoline). The resulting crude product was purified by flash chromatography [0-100%(10%MeOH/EA)/hex to provide 7-chloro-1-methyl-3-(4-(quinolin-7-yl)benzyl)-3,4-dihydro-1H-benzo[e][1,4]diazepine-2,5-dione (overall yield= 36.2%) as an off-white solid; R_f= 0.35 (EA); Purity: overall= 97.3%; ¹H NMR (500 MHz) (δ/ppm) 3.10 (ddt, 1H, J=12.4, J=7.0, J=1.0, 15), 3.38 (s, 1H, 12), 3.51 (ddt, 1H, J=12.5, J=7.1, J=1.1, 15'), 4.97 (t, 1H, J=7.0, 1), 7.13 (d, 1H, J=7.5, 6), 7.48 (m, 3H, 1, 17, 21), 7.64 (d, 2H, J=10.9, 18, 20), 7.71 (t, 1H, J=7.5, 31), 7.75 (dd, 1H, J=7.5, J=1.5, 27), 8.04 (dd, 1H, J=7.5, J=1.5, 26), 8.08 (d, 1H, J=1.9, 3), 8.18 (d, 1H, J=1.5, 23), 8.36 (s, 1H, 8), 8.62 (dt, 1H, J=7.7, J=1.5, 32), 9.03 (dd, 1H, J=7.5, J=1.5, 30); ¹³C NMR (500 MHz) (δ/ppm) 33.7, 37.6, 54.2, 121.2, 121.8, 123.9, 125.7, 126.6, 127.8, 127.9, 128.1, 128.5, 131.5, 131.5, 132.2, 134.5, 135.8, 137.5, 138.9, 140.8, 147.1, 150.4, 168.5, 169.5; Exact Mass (ES): determined mass: 441.1247 u, exact mass: 441.1244 u.

3-(4-(1H-indol-6-yl)benzyl)-7-chloro-1-methyl-3,4-dihydro-1H-benzo[e][1,4]diazepine-2,5-dione (rac-2; LDM-2-31)



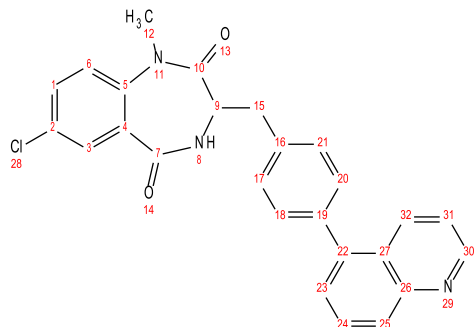
2 was prepared by GP2 (starting material: 5-chloroisatoic anhydride), GP3, GP4, GP5, and GP6 (reagent: 6-bromo-1H-indole). The resulting crude product was purified by flash chromatography [0-100%(10%MeOH/EA)/hex] to provide 3-(4-(1H-indol-6-yl)benzyl)-7-chloro-1-methyl-3,4-dihydro-1H-benzo[e][1,4]diazepine-2,5-dione (overall yield= 43.2%) as an off-white solid; R_f= 0.35 (EA); Purity: overall= 96.8%; ¹H NMR (500 MHz) (δ/ppm) 3.22 (ddt, 1H, J=12.4, 7.3, 1.1, 15), 3.28 (ddt, 1H, J=12.4, 7.1, 1.0, 15'), 3.40 (s, 3H, 12), 4.89 (t, 1H, J=7.2, 9), 6.56 (dd, 1H, J=7.5, J=1.5, 31), 7.14 (d, 1H, J=7.6, 6), 7.35 (m, 3H, 17, 21, 30), 7.49 (dd, 1H, J=7.4, J=2.1, 1), 7.64 (d, 2H, J=10.9, 18, 20), 7.91 (m, 2H, 23, 27), 7.99 (s, 1H, 8), 8.15 (dd, 1H, J=7.5, J=1.5, 26), 8.21 (d, 1H, J=2.0, 3), 11.57 (s, 1H, 29); ¹³C NMR (500 MHz) (δ/ppm) 33.7, 37.6, 54.2, 102.7, 112.3, 121.0, 121.9, 123.9, 124.9, 125.7, 127.8, 127.8, 128.5, 131.5, 131.5, 132.2, 134.5, 135.6, 136.3, 137.5, 140.8, 168.5, 169.5; Exact Mass (ES): determined mass: 429.1247 u, exact mass: 429.1244 u.

7-chloro-3-(4-(isoquinolin-5-yl)benzyl)-1-methyl-3,4-dihydro-1H-benzo[e][1,4]diazepine-2,5-dione (rac-3; LDM-2-21)



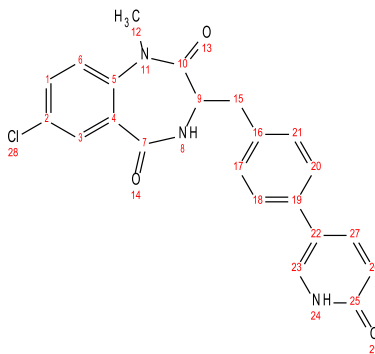
3 was prepared by GP2 (starting material: 5-chloroisatoic anhydride), GP3, GP4, GP5, and GP6 (reagent: 5-bromoisoquinoline). The resulting crude product was purified by flash chromatography [0-100%(10%MeOH/EA)/hex] to provide 7-chloro-3-(4-(isoquinolin-5-yl)benzyl)-1-methyl-3,4-dihydro-1H-benzo[e][1,4]diazepine-2,5-dione (overall yield= 36.8%) as an off-white solid; R_f= 0.35 (EA); Purity: overall= 95.8%; ¹H NMR (500 MHz) (δ/ppm) 3.23 (ddt, 1H, J=12.4, J=7.2, J=1.0, 15), 3.29 (ddt, 1H, J=12.3, J=7.1, J=1.1, 15'), 3.41 (s, 3H, 12), 4.89 (t, 1H, J=7.2, 9), 7.15 (d, 1H, J=7.5, 6), 7.38 (dt, 2H, J=7.5, J=1.2, 17, 21), 7.49 (dd, 1H, J=7.4, J=1.9, 1), 7.69 (m, 3H, 18, 20, 24), 7.84 (d, 1H, J=7.5, 32), 7.90 (dd, 1H, J=7.6, J=1.6, 23), 8.04 (m, 2H, 3, 25), 8.34 (s, 1H, 8), 8.53 (d, 1H, J=7.5, 31), 9.26 (d, 1H, J=1.5); ¹³C NMR (500 MHz) (δ/ppm) 33.7, 37.6, 54.2, 116.4, 123.9, 124.7, 125.7, 126.6, 127.0, 127.8, 128.3, 129.3, 131.5, 131.5, 132.2, 135.2, 135.3, 135.6, 139.8, 140.8, 147.8, 152.3, 168.5, 169.5; Exact Mass (ES): determined mass: 441.1249 u, exact mass: 441.1244 u.

7-chloro-1-methyl-3-(4-(quinolin-5-yl)benzyl)-3,4-dihydro-1H-benzo[e][1,4]diazepine-2,5-dione (rac-4; LDM-2-23)



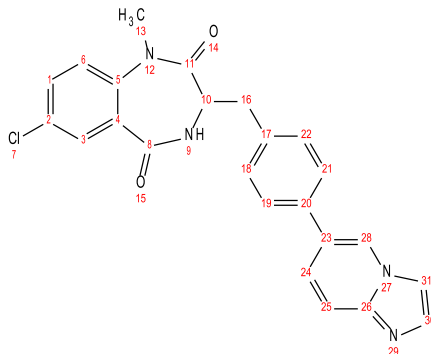
4 was prepared by GP2 (starting material: 5-chloroisatoic anhydride), GP3, GP4, GP5, and GP6 (reagent: 5-bromoquinoline). The resulting crude product was purified by flash chromatography [0-100%(10%MeOH/EA)/hex] to provide 7-chloro-1-methyl-3-(4-(quinolin-5-yl)benzyl)-3,4-dihydro-1H-benzo[e][1,4]diazepine-2,5-dione (overall yield= 42.9%) as an off-white solid; R_f= 0.35 (EA); Purity: overall= 96.1%; ¹H NMR (500 MHz) (δ/ppm) 3.26 (qdt, 2H, J=12.4, J=7.1, J=1.0, 15, 15'), 3.40 (s, 3H, 12), 4.91 (t, 1H, J=7.2, 9), 7.15 (d, 1H, J=7.6, 6), 7.37 (dt, 2H, J=7.4, J=1.2, 17, 21), 7.49 (dd, 1H, J=7.5, J=1.9, 1), 7.60 (m, 2H, 18, 20), 7.66 (t, 1H, J=7.5, 31), 7.80 (m, 2H, 23, 24), 8.12 (dd, 2H, J=6.9, J=1.9, 3, 25), 8.20 (dd, 1H, J=7.5, J=1.5, 32), 8.33 (s, 1H, 8), 8.88 (dd, 1H, J=7.7, J=1.5, 30); ¹³C NMR (500 MHz) (δ/ppm) 33.7, 37.6, 54.2, 123.3, 123.7, 123.9, 124.3, 125.7, 127.0, 128.3, 128.8, 129.3, 131.5, 131.5, 132.2, 132.5, 135.2, 135.3, 137.7, 140.8, 147.1, 149.6, 168.5, 169.5; Exact Mass (ES): determined mass: 441.1254 u, exact mass: 441.1244 u.

7-chloro-1-methyl-3-(4-(6-oxo-1,6-dihydropyridin-3-yl)benzyl)-3,4-dihydro-1H-benzo[e][1,4]diazepine-2,5-dione (rac-5; LDM-2-27)



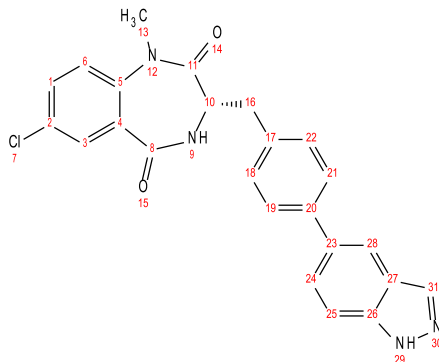
5 was prepared by GP2 (starting material: 5-chloroisatoic anhydride), GP3, GP4, GP5, and GP6 (reagent: 5-bromopyridin-2(1H)-one). The resulting crude product was purified by flash chromatography [0-100%(10%MeOH/EA)/hex] to provide 7-chloro-1-methyl-3-(4-(6-oxo-1,6-dihydropyridin-3-yl)benzyl)-3,4-dihydro-1H-benzo[e][1,4]diazepine-2,5-dione (overall yield= 32.4%) as an off-white solid; Purity: overall= 95.5%; R_f= 0.35 (EA); ¹H NMR (500 MHz) (δ/ppm) 3.26 (m, 1H, 15, 15'), 3.41 (s, 3H, 12), 4.91 (t, 1H, J=6.7, 9), 6.42 (d, 1H, J=10.9, 26), 7.15 (d, 1H, J=7.6, 6), 7.28 (dt, 2H, J=7.3, J=1.0, 17, 21), 7.41 (m, 2H, 18, 20), 7.49 (dd, 1H, J=7.6, J=2.0, 1), 7.55 (d, 1H, J=10.9, 27), 7.94 (s, 1H, 23), 8.18 (d, 1H, J=2.0, 3), 8.52 (s, 1H, 8), 11.24 (s, 1H, 24); ¹³C NMR (500 MHz) (δ/ppm) 33.7, 37.6, 54.2, 110.6, 121.4, 123.9, 125.7, 125.9, 129.5, 131.5, 131.5, 132.2, 133.9, 135.1, 136.8, 140.1, 140.8, 161.2, 168.5, 169.5; Exact Mass (ES): determined mass: 407.1042 u, exact mass: 407.1037 u.

7-chloro-3-(4-(imidazo[1,2-a]pyridin-6-yl)benzyl)-1-methyl-3,4-dihydro-1H-benzo[e][1,4]diazepine-2,5-dione (rac-6; LDM-2-19)



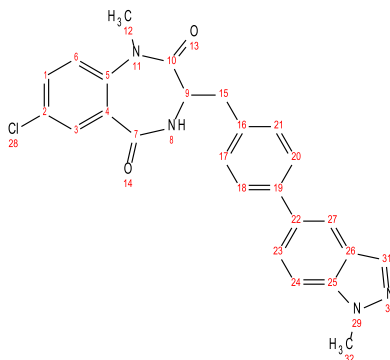
6 was prepared by GP2 (starting material: 5-chloroisatoic anhydride), GP3, GP4, GP5, and GP6 (reagent: 6-bromoimidazo[1,2-a]pyridine). The resulting crude product was purified by flash chromatography [0-100%(10%MeOH/EA)/hex] to provide 7-chloro-3-(4-(imidazo[1,2-a]pyridin-6-yl)benzyl)-1-methyl-3,4-dihydro-1H-benzo[e][1,4]diazepine-2,5-dione (overall yield= 31.5%) as an off-white solid; R_f= 0.35 (EA); Purity: overall= 96.2%; ¹H NMR (500 MHz) (δ/ppm) 3.10 (ddt, 1H, J=12.5, J=6.3, J=1.1, 16), 3.39 (s, 3H, 13), 3.53 (ddt, 1H, J=12.4, J=6.2, J=1.1, 16'), 5.02 (t, 1H, J=6.3, 10), 7.19 (d, 1H, J=7.5, 6), 7.48 (dd, 1H, J=7.5, J=1.9, 1), 7.56 (dt, 2H, J=7.3, J=1.1, 18, 22), 7.64 (d, 1H, J=7.5, 31), 7.68 (d, 2H, J=5.0, 19, 21), 7.83 (d, 1H, J=7.5, 25), 7.94 (dd, 1H, J=7.5, J=1.5, 24), 8.06 (m, 2H, 3, 30), 8.16 (s, 1H, 9), 8.99 (d, 1H, J=1.5, 28); ¹³C NMR (500 MHz) (δ/ppm) 33.7, 37.6, 54.2, 114.1, 120.3, 123.9, 125.7, 126.0, 129.8, 131.3, 131.5, 131.5, 132.2, 133.2, 134.0, 134.6, 134.8, 140.8, 144.7, 168.5, 169.5; Exact Mass (ES): determined mass: 430.1202 u, exact mass: 430.1197 u.

3-(4-(1H-indazol-5-yl)benzyl)-7-chloro-1-methyl-3,4-dihydro-1H-benzo[e][1,4]diazepine-2,5-dione ((S)-7; LDM-2-17)



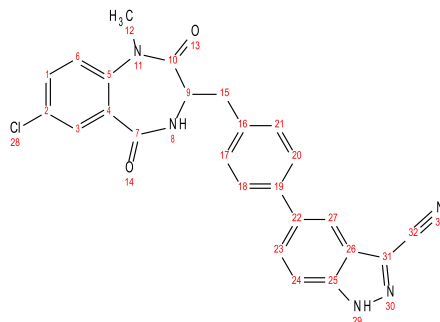
(S)-7 was prepared by GP2 (starting material: 5-chloroisatoic anhydride), GP3, GP4, GP5, and GP6 (reagent: 5-bromo-1H-indazole). The resulting crude product was purified by flash chromatography [0-100%(10%MeOH/EA)/hex] to provide 3-(4-(1H-indazol-5-yl)benzyl)-7-chloro-1-methyl-3,4-dihydro-1H-benzo[e][1,4]diazepine-2,5-dione (overall yield= 40.1%) as an off-white solid; R_f= 0.35 (EA); Purity: overall= 96.1%, chiral= 97.8%; ¹H NMR (500 MHz) (δ/ppm) 3.21 (ddt, 1H, J=12.5, J=7.3, J=1.1, 16), 3.28 (ddt, 1H, J=12.4, J=7.3, J=1.1, 16'), 3.40 (s, 3H, 13), 4.88 (t, 1H, J=7.3, 10), 7.19 (d, 1H, J=7.6, 6), 7.39 (dt, 2H, J=7.7, J=1.1, 18, 22), 7.49 (dd, 1H, J=7.5, J=2.1, 1), 7.64 (m, 3H, 19, 21, 26) 7.95 (dd, 1H, J=7.5, J=1.3, 24), 8.10 (d, 1H, J=2.0, 3), 8.33 (d, 2H, J=1.7, 28, 31), 8.37 (s, 1H, 9) ; ¹³C NMR (500 MHz) (δ/ppm) 33.7, 37.6, 54.2, 110.9, 119.2, 123.5, 123.9, 125.7, 126.6, 127.8, 128.5, 131.5, 131.5, 135.7, 137.5, 139.4, 140.8, 168.5, 169.5 ; Exact Mass (ES): determined mass: 430.1204 u, exact mass: 430.1197 u.

7-chloro-1-methyl-3-(4-(1-methyl-1H-indazol-5-yl)benzyl)-3,4-dihydro-1H-benzo[e][1,4]diazepine-2,5-dione (rac-8; LDM-2-33)



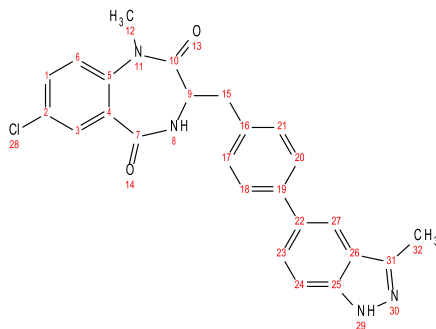
8 was prepared by GP2 (starting material: 5-chloroisatoic anhydride), GP3, GP4, GP5, and GP6 (reagent: 5-bromo-1-methyl-1H-indazole). The resulting crude product was purified by flash chromatography [0-100%(10%MeOH/EA)/hex] to provide 7-chloro-1-methyl-3-(4-(1-methyl-1H-indazol-5-yl)benzyl)-3,4-dihydro-1H-benzo[e][1,4]diazepine-2,5-dione (overall yield= 46.6%) as an off-white solid; Rf= 0.35 (EA); Purity: overall= 95.2%; ¹H NMR (500 MHz) (δ/ppm) 3.16 (ddt, 1H, J=12.5, J=6.0, J=1.1, 15), 3.31 (ddt, 1H, J=12.4, J=5.9, J=1.0, 15'), 3.39 (s, 3H, 12), 3.81 (s, 3H, 32), 4.97 (t, 1H, J=6.0, 9), 7.13 (d, 1H, J=7.5, 6), 7.38 (dt, 2H, J=7.6, J=1.1), 7.48 (dd, 1H, J=7.5, J=1.9, 1), 7.64 (d, 2H, J=10.9, 18, 20), 7.81 (d, 1H, J=7.5, 24), 7.89 (dd, 1H, J=7.4, J=1.4, 23), 8.10 (d, 1H, J=1.9, 3), 8.26 (dt, 2H, J=2.6, J=1.4, 27, 31), 8.29 (s, 1H, 8); ¹³C NMR (500 MHz) (δ/ppm) 33.7, 35.6, 37.6, 54.2, 113.0, 120.1, 123.9, 125.7, 126.8, 127.8, 128.5, 131.5, 131.5, 132.2, 132.7, 133.2, 134.5, 137.5, 138.3, 140.8, 168.5, 169.5; Exact Mass (ES): determined mass: 444.1363 u, exact mass: 444.1353 u.

5-(4-((7-chloro-1-methyl-2,5-dioxo-2,3,4,5-tetrahydro-1H-benzo[e][1,4]diazepin-3-yl)methyl)phenyl)-1H-indazole-3-carbonitrile ((S)-9; LDM-2-235)



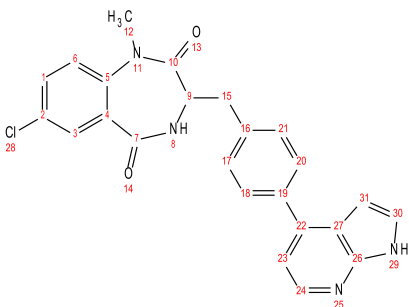
(S)-9 was prepared by GP2 (starting material: 5-chloroisatoic anhydride), GP3, GP4, GP5, and GP6 (reagent: 5-bromo-1H-indazole-3-carbonitrile). The resulting crude product was purified by flash chromatography [0-100%(10%MeOH/EA)/hex] to provide 5-(4-((7-chloro-1-methyl-2,5-dioxo-2,3,4,5-tetrahydro-1H-benzo[e][1,4]diazepin-3-yl)methyl)phenyl)-1H-indazole-3-carbonitrile (overall yield= 41.1%) as an off-white solid; R_f= 0.35 (EA); Purity: overall= 95.8%, chiral=97.1; ¹H NMR (500 MHz) (δ/ppm) 3.21 (ddt, 1H, J=12.4, J=7.1, J=1.0, 15), 3.28 (ddt, 1H, J=12.4, J=7.2, J=1.0, 15'), 3.40 (s, 3H, 12), 4.88 (t, 1H, J=7.2, 9), 7.14 (d, 1h, J=7.5, 6), 7.36 (dt, 2H, J=7.4, J=1.1, 17, 21), 7.49 (dd, 1H, J=7.5, J=1.9, 1), 7.64 (m, 3H, 18, 20, 24), 7.97 (dd, 1H, J=7.5, J=1.5, 23), 8.01 (s, 1H, 8), 8.20 (d, 1H, J=1.9, 3), 8.70 (d, 1H, J=1.5, 27); ¹³C NMR (500 MHz) (δ/ppm) 33.7, 37.6, 54.2, 108.7, 112.6, 114.7, 120.6, 120.6, 123.9, 125.0, 125.7, 127.8, 128.5, 131.5, 131.5, 132.2, 134.5, 134.6, 137.5, 140.8, 141.9, 168.5, 169.5; Exact Mass (ES): determined mass: 455.1154 u, exact mass: 455.1149 u.

7-chloro-1-methyl-3-(4-(3-methyl-1H-indazol-5-yl)benzyl)-3,4-dihydro-1H-benzo[e][1,4]diazepine-2,5-dione ((S)-10; LDM-2-243)



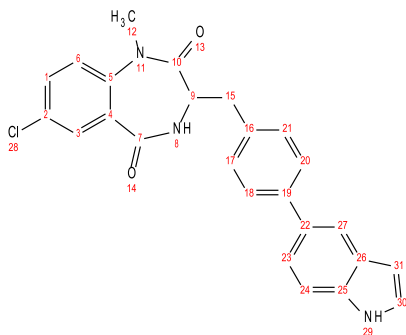
(S)-10 was prepared by GP2 (starting material: 5-chloroisatoic anhydride), GP3, GP4, GP5, and GP6 (reagent: 5-bromo-3-methyl-1H-indazole). The resulting crude product was purified by flash chromatography [0-100%(10%MeOH/EA)/hex] to provide 7-chloro-1-methyl-3-(4-(3-methyl-1H-indazol-5-yl)benzyl)-3,4-dihydro-1H-benzo[e][1,4]diazepine-2,5-dione (overall yield= 31.0%) as an off-white solid; R_f= 0.35 (EA); Purity: overall= 96.2%, chiral= 95.9%; ¹H NMR (500 MHz) (δ/ppm) 2.58 (s, 3H, 32), 3.25 (m, 2H, 15, 15'), 3.40 (s, 3H, 12), 4.95 (t, 1H, J=6.8), 7.14 (d, 1H, J=7.5, 6), 7.36 (dt, 2H, J=7.4, J=1.1, 17, 21), 7.49 (dd, 1H, J=7.5, J=1.9, 1), 7.58 (d, 1H, J=7.5, 24), 7.64 (d, 2H, J=10.9, 18, 20), 7.97 (dd, 1H, J=7.5, J=1.5, 23), 8.17 (dd, 2H, J=10.2, J=1.8, 3, 27), 8.28 (s, 1H, 8); ¹³C NMR (500 MHz) (δ/ppm) 13.4, 33.7, 37.6, 54.2, 112.2, 121.1, 121.9, 123.9, 125.2, 125.7, 127.8, 128.5, 131.5, 131.5, 132.2, 134.4, 134.5, 137.5, 140.8, 140.9, 144.6, 168.5, 169.5; Exact Mass (ES): determined mass: 444.1350 u, exact mass: 444.1353 u.

3-(4-(1H-pyrrolo[2,3-b]pyridin-4-yl)benzyl)-7-chloro-1-methyl-3,4-dihydro-1H-benzo[e][1,4]diazepine-2,5-dione (rac-11; LDM-2-269)



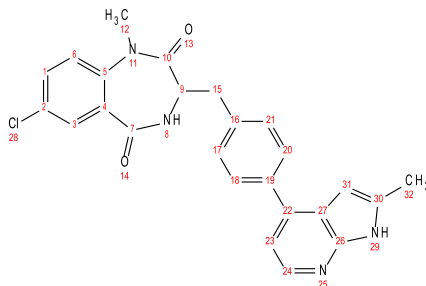
11 was prepared by GP2 (starting material: 5-chloroisatoic anhydride), GP3, GP4, GP5, and GP6 (reagent: 4-bromo-7-azaindole). The resulting crude product was purified by flash chromatography [0-100%(10%MeOH/EA)/hex] to provide 3-(4-(1H-pyrrolo[2,3-b]pyridin-4-yl)benzyl)-7-chloro-1-methyl-3,4-dihydro-1H-benzo[e][1,4]diazepine-2,5-dione (overall yield= 35.7%) as an off-white solid; R_f= 0.35 (EA); Purity: overall= 97.1%, chiral= 95.0%; ¹H NMR (500 MHz) (δ/ppm) 3.22 (ddt, 1H, J=12.4, J=7.1, J=1.0, 15), 3.30 (ddt, 1H, J=12.4, J=7.2, J=1.0, 15'), 3.40 (s, 3H, 12), 4.88 (t, 1H, J=7.2, 9), 6.74 (d, 1H, J=7.5, 31), 7.15 (d, 1H, J=7.5, 6), 7.37 (m, 3H, 17, 21, 30), 7.49 (dd, 1H, J=7.6, J=2.0, 1), 7.75 (d, 2H, J=10.9, 18, 20), 7.90 (d, 1H, J=7.5, 23), 8.02 (s, 1H, 8), 8.17 (d, 1H, J=2.0, 3), 8.65 (d, 1H, J=7.5, 24), 11.84 (s, 1H, 29); ¹³C NMR (500 MHz) (δ/ppm) 33.7, 37.6, 54.2, 94.5, 115.9, 122.7, 123.4, 123.9, 125.7, 128.2, 129.6, 131.5, 131.5, 132.2, 134.7, 137.4, 138.6, 140.8, 145.1, 148.4, 168.5, 169.5; Exact Mass (ES): determined mass: 430.1203 u, exact mass: 430.1197 u.

3-(4-(1H-indol-5-yl)benzyl)-7-chloro-1-methyl-3,4-dihydro-1H-benzo[e][1,4]diazepine-2,5-dione (rac-12; LDM-2-25)



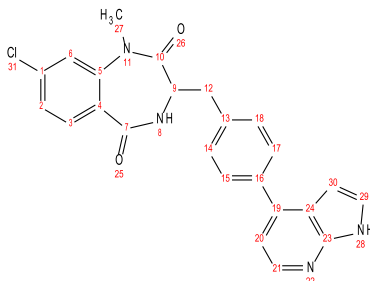
12 was prepared by GP2 (starting material: 5-chloroisatoic anhydride), GP3, GP4, GP5, and GP6 (reagent: 5-bromo-1H-indole). The resulting crude product was purified by flash chromatography [0-100%(10%MeOH/EA)/hex] to provide 3-(4-(1H-indol-5-yl)benzyl)-7-chloro-1-methyl-3,4-dihydro-1H-benzo[e][1,4]diazepine-2,5-dione (overall yield= 39.6%) as an off-white solid; R_f= 0.35 (EA); Purity: overall= 95.9%; ¹H NMR (500 MHz) (δ/ppm) 3.21 (ddt, 1H, J=12.5, J=7.2, J=1.1, 15), 3.28 (ddt, 1H, J=12.4, J=7.2, J=1.0, 15'), 3.40 (s, 3H, 12), 4.88 (t, 1H, J=7.3, 9), 6.68 (dd, 1H, J=7.5, J=1.5, 31), 7.14 (d, 1H, J=7.5, 17), 7.34 (ddd, 3H, J=7.5, J=2.5, J=1.2, 17, 21, 30), 7.49 (dd, 1H, J=7.5, J=1.9, 1), 7.64 (m, 2H, 18, 20), 7.73 (d, 1H, J=7.5, 24), 7.85 (dd, 1H, J=7.5, J=1.5, 23), 8.00 (s, 1H, 8), 8.13 (t, 1H, J=1.5, 27), 8.20 (d, 1H, J=2.0, 3), 11.53 (s, 1H, 29); ¹³C NMR (500 MHz) (δ/ppm) 33.7, 37.6, 54.2, 102.7, 112.9, 120.4, 123.8, 125.7, 125.8, 125.9, 127.8, 128.5, 131.5, 131.5, 132.2, 134.5, 134.6, 137.4, 137.5, 140.8, 168.5, 169.5; Exact Mass (ES): determined mass: 429.1247 u, exact mass: 429.1244 u.

7-chloro-1-methyl-3-(4-(2-methyl-1H-pyrrolo[2,3-b]pyridin-4-yl)benzyl)-3,4-dihydro-1H-benzo[e][1,4]diazepine-2,5-dione ((S)-13; LDM-2-299)



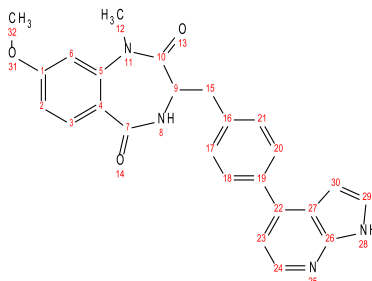
(S)-13 was prepared by GP2 (starting material: 5-chloroisatoic anhydride), GP3, GP4, GP5, and GP6 (reagent: 4-bromo-2-methyl-7-azaindole). The resulting crude product was purified by flash chromatography [0-100%(10%MeOH/EA)/hex] to provide 7-chloro-1-methyl-3-(4-(2-methyl-1H-pyrrolo[2,3-b]pyridin-4-yl)benzyl)-3,4-dihydro-1H-benzo[e][1,4]diazepine-2,5-dione (overall yield= 46.6%) as an off-white solid; R_f= 0.35 (EA); Purity: overall= 96.6%, chiral= 97.2%; ¹H NMR (500 MHz) (δ/ppm) 2.29 (s, 3H, 32), 3.21 (ddt, 1H, J=12.4, J=6.7, J=1.0, 15), 3.29 (ddt, 1H, J=12.6, J=6.6, J=1.0, 15'), 3.40 (s, 3H, 12), 4.94 (t, 1H, J=6.5, 9), 6.33 (s, 1H, 31), 7.14 (d, 1H, J=7.5, 6), 7.42 (dt, 2H, J=7.2, J=1.1, 17, 21), 7.49 (dd, 1H, J=7.6, J=2.0, 1), 7.78 (d, 2H, J=10.9, 18, 20), 7.89 (d, 1H, J=7.5, 23), 8.05 (d, 1H, J=1.9, 3), 8.43 (s, 1H, 8), 8.61 (d, 1H, J=7.5, 24), 11.59 (s, 1H, 29); ¹³C NMR (500 MHz) (δ/ppm) 13.1, 33.7, 37.6, 54.2, 97.1, 115.5, 123.9, 125.7, 127.8, 128.2, 129.6, 130.8, 131.5, 131.5, 132.2, 134.7, 135.8, 136.6, 140.8, 144.8, 149.6, 168.5, 169.5; Exact Mass (ES): determined mass: 444.1362 u, exact mass: 444.1353 u.

3-(4-(1H-pyrrolo[2,3-b]pyridin-4-yl)benzyl)-8-chloro-1-methyl-3,4-dihydro-1H-benzo[e][1,4]diazepine-2,5-dione ((S)-14; LDM-2-307)



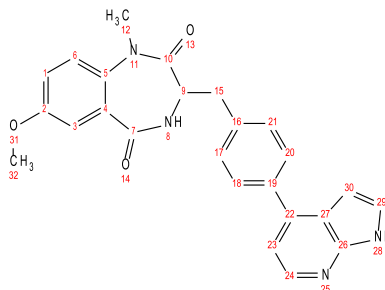
(S)-14 was prepared by GP2 (starting material: 4-chloroisatoic anhydride), GP3, GP4, and GP6 (reagent: 4-(4,4,5,5-tetramethyl-1,3,2-dioxaborolan-2-yl)-1H-pyrrolo[2,3-b]pyridine). The resulting crude product was purified by flash chromatography [0-100%(10%MeOH/EA)/hex] to provide 3-(4-(1H-pyrrolo[2,3-b]pyridin-4-yl)benzyl)-8-chloro-1-methyl-3,4-dihydro-1H-benzo[e][1,4]diazepine-2,5-dione (overall yield= 38.2%) as an off-white solid; R_f= 0.35 (EA); Purity: overall= 95.9%, chiral= 95.8%; ¹H NMR (500 MHz) (δ/ppm) 3.23 (ddt, 1H, J=12.5, J=7.4, J=1.1, 15), 3.31 (ddt, 1H, J=12.3, J=7.1, 15'), 3.41 (s, 3H, 12), 4.88 (t, 1H, J=7.1, 9), 6.86 (d, 1H, J=7.5, 30), 7.38 (ddd, 3H, J=7.3, J=2.2, J=1.2, 17, 19, 21), 7.53 (dd, 1H, J=7.5, J=1.9, 2), 7.61 (d, 1H, J=2.0, 6), 7.77 (d, 2H, J=10.9, 18, 20), 7.91 (d, 1H, J=7.5, 23), 7.96 (d, 1H, J=7.5, 3), 8.47 (s, 1H, 8), 8.65 (d, 1H, J=7.5, 24), 11.83 (s, 1H, 28); ¹³C NMR (500 MHz) (δ/ppm) 33.4, 37.6, 54.2, 94.5, 115.9, 120.4, 122.3, 122.7, 123.4, 128.2, 128.5, 129.6, 131.0, 134.7, 137.4, 137.5, 138.6, 142.2, 145.1, 148.4, 167.6, 168.7; Exact Mass (ES): determined mass: 430.1206 u, exact mass: 430.1197 u.

3-(4-(1H-pyrrolo[2,3-b]pyridin-4-yl)benzyl)-8-methoxy-1-methyl-3,4-dihydro-1H-benzo[e][1,4]diazepine-2,5-dione ((S)-15; LDM-3-3)



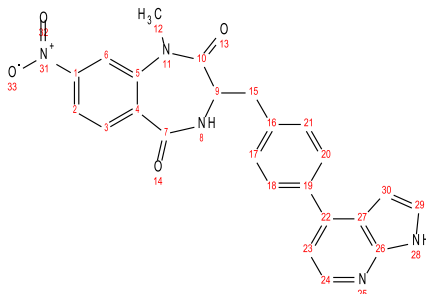
(S)-15 was prepared by GP2 (starting material: 4-methoxyisatoic anhydride), GP3, GP4, and GP6 (reagent: 4-(4,4,5,5-tetramethyl-1,3,2-dioxaborolan-2-yl)-1H-pyrrolo[2,3-b]pyridine). The resulting crude product was purified by flash chromatography [0-100%(10%MeOH/EA)/hex] to provide 3-(4-(1H-pyrrolo[2,3-b]pyridin-4-yl)benzyl)-8-methoxy-1-methyl-3,4-dihydro-1H-benzo[e][1,4]diazepine-2,5-dione (overall yield= 42.2%) as an off-white solid; Rf= 0.35 (EA); Purity: overall= 96.1%, chiral= 98.0%; ¹H NMR (500 MHz) (δ/ppm) 3.22 (ddt, 1H, J=12.5, J=7.4, J=1.1, 15), 3.29 (ddt, 1H, J=12.5, J=7.1, J=1.1, 15'), 3.40 (s, 3H, 12), 3.77 (s, 3H, 32), 4.88 (t, 1H, J=7.0, 9), 6.68 (d, 1H, J=7.5, 30), 6.99 (d, 2H, J=7.0, 2, 6), 7.35 (d, 1H, J=7.5, 29), 7.38 (dt, 2H, J=7.4, J=1.1, 17, 21), 7.80 (m, 2H, 18, 20), 7.97 (t, 2H, J=7.1, 3, 23), 8.37 (s, 1H, 8), 8.66 (d, 1H, J=7.5, 24), 11.84 (s, 1H, 28); ¹³C NMR (500 MHz) (δ/ppm) 33.4, 37.6, 54.2, 55.6, 94.5, 107.5, 111.7, 115.9, 122.7, 123.4, 126.7, 128.2, 129.6, 130.9, 134.7, 137.4, 138.6, 141.0, 145.1, 148.4, 160.3, 167.6, 168.7; Exact Mass (ES): determined mass: 426.1697 u, exact mass: 426.1692 u.

3-(4-(1H-pyrrolo[2,3-b]pyridin-4-yl)benzyl)-7-methoxy-1-methyl-3,4-dihydro-1H-benzo[e][1,4]diazepine-2,5-dione ((S)-16; LDM-3-5)



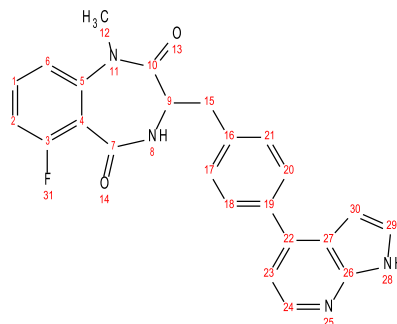
(S)-16 was prepared by GP2 (starting material: 5-chloroisatoic anhydride), GP3, GP4, and GP6 (reagent: 4-(4,4,5,5-tetramethyl-1,3,2-dioxaborolan-2-yl)-1H-pyrrolo[2,3-b]pyridine). The resulting crude product was purified by flash chromatography [0-100%(10%MeOH/EA)/hex] to provide 3-(4-(1H-pyrrolo[2,3-b]pyridin-4-yl)benzyl)-7-methoxy-1-methyl-3,4-dihydro-1H-benzo[e][1,4]diazepine-2,5-dione (overall yield= 49.8%) as an off-white solid; Rf= 0.35 (EA); Purity: overall= 96.0%, chiral= 95.8%; ¹H NMR (500 MHz) (δ/ppm) 3.16 (ddt, 1H, J=12.6, J=6.3, J=1.1, 15), 3.33 (ddt, 1H, J=12.4, J=6.3, J=1.0, 15'), 3.40 (s, 3H, 12), 3.73 (s, 3H, 32), 5.09 (t, 1H, J=6.2, 6.67 (d, 1H, J=7.5, 30), 7.35 (d, 1H, J=7.5, 29), 7.41 (dt, 1H, J=7.5, J=1.2, 17, 21), 7.60 (m, 2H, 3, 6), 7.64 (dd, 1H, J=7.5, J=1.9, 1), 7.73 (d, 2H, J=10.9, 18, 20), 7.89 (d, 1H, J=7.5, 23), 8.23 (s, 1H, 8), 8.64 (d, 1H, J=7.5, 24), 11.74 (s, 1H, 28); ¹³C NMR (500 MHz) (δ/ppm) 33.7, 37.6, 54.2, 55.8, 94.5, 115.4, 115.9, 116.8, 122.7, 123.2, 123.4, 128.2, 129.6, 131.8, 134.7, 137.4, 138.6, 138.6, 145.1, 148.4, 158.2, 168.5, 169.5; Exact Mass (ES): determined mass: 426.1697 u, exact mass: 426.1692 u.

3-(4-(1H-pyrrolo[2,3-b]pyridin-4-yl)benzyl)-1-methyl-8-nitro-3,4-dihydro-1H-benzo[e][1,4]diazepine-2,5-dione ((S)-17; LDM-3-35)



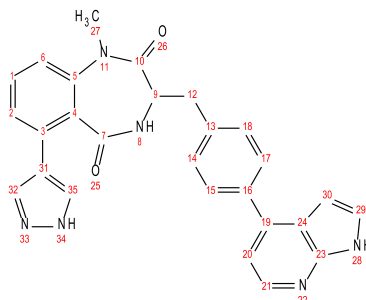
(S)-17 was prepared by GP2 (starting material: 4-nitroisatoic anhydride), GP3, GP4, and GP6 (reagent: 4-(4,4,5,5-tetramethyl-1,3,2-dioxaborolan-2-yl)-1H-pyrrolo[2,3-b]pyridine). The resulting crude product was purified by flash chromatography [0-100%(10%MeOH/EA)/hex] to provide 3-(4-(1H-pyrrolo[2,3-b]pyridin-4-yl)benzyl)-1-methyl-8-nitro-3,4-dihydro-1H-benzo[e][1,4]diazepine-2,5-dione (overall yield= 30.1%) as an off-white solid; R_f= 0.35 (EA); Purity: overall= 96.4%, chiral= 97.1%; ¹H NMR (500 MHz) (δ/ppm) 3.20 (m, 2H, 15, 15'), 3.43 (s, 3H, 12), 4.88 (t, 1H, J=6.9, 9), 6.66 (d, 1H, J=7.5, 30), 7.40 (m, 3H, 17, 21, 29), 7.80 (m, 2H, 18, 20), 7.98 (d, 1H, J=7.7, 23), 8.12 (dd, 1H, J=7.6, J=2.0, 2), 8.15 (s, 1H, 8), 8.19 (d, 1H, J=2.0, 6), 8.29 (d, 1H, J=7.6, 3), 8.67 (d, 1H, J=7.5, 24) 11.85 (s, 1H, 28); ¹³C NMR (500 MHz) (δ/ppm) 33.4, 37.6, 54.2, 94.5, 113.6, 115.9, 117.0, 122.7, 123.4, 128.1, 128.2, 129.6, 130.5, 134.7, 137.4, 138.6, 144.0, 145.1, 147.3, 148.4, 167.6, 168.7; Exact Mass (ES): determined mass: 441.1447 u, exact mass: 441.1437 u.

3-(4-(1H-pyrrolo[2,3-b]pyridin-4-yl)benzyl)-6-fluoro-1-methyl-3,4-dihydro-1H-benzo[e][1,4]diazepine-2,5-dione ((S)-18; LDM-3-39)



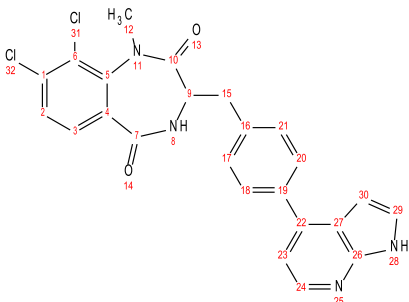
(S)-18 was prepared by GP1 (starting material: 2-amino-6-fluorobenzoic acid), GP2, GP3, GP4, and GP6 (reagent: 4-(4,4,5,5-tetramethyl-1,3,2-dioxaborolan-2-yl)-1H-pyrrolo[2,3-b]pyridine). The resulting crude product was purified by flash chromatography [0-100%(10%MeOH/EA)/hex] to provide 3-(4-(1H-pyrrolo[2,3-b]pyridin-4-yl)benzyl)-6-fluoro-1-methyl-3,4-dihydro-1H-benzo[e][1,4]diazepine-2,5-dione (overall yield= 24.3%) as an off-white solid; Rf= 0.35 (EA); Purity: overall= 96.9%, chiral= 97.0%; ¹H NMR (500 MHz) (δ/ppm) 3.14 (ddt, 1H, J=12.6, J=6.3, J=1.2, 15), 3.38 (s, 3H, 12), 3.45 (ddt, 1H, J=12.4, J=6.2, J=1.0, 15'), 4.99 (t, 1H, J=6.2, 9), 6.65 (d, 1H, J=7.5, 30), 7.01 (dd, 1H, J=7.5, J=1.9, 6), 7.25 (t, 1H, J=3.1, 2), 7.33 (d, 1H, J=7.5, 29), 7.50 (m, 3H, 1, 17, 21), 7.74 (d, 2H, J=10.9, 18, 20), 7.93 (d, 1H, J=7.5, 23), 8.24 (s, 1H, 8), 8.68 (d, 1H, J=7.5, 24), 11.74 (s, 1H, 28); ¹³C NMR (500 MHz) (δ/ppm) 33.4, 37.6, 54.3, 94.5, 110.4, 110.6, 115.9, 118.2, 118.2, 120.0, 120.2, 122.7, 123.4, 128.2, 129.6, 130.9, 131.0, 134.7, 137.4, 138.6, 142.2, 142.2, 145.1, 148.4, 159.3, 161.3, 167.5, 167.5, 168.7; Exact Mass (ES): determined mass: 414.1505 u, exact mass: 414.1492 u.

3-(4-(1H-pyrrolo[2,3-b]pyridin-4-yl)benzyl)-1-methyl-6-(1H-pyrazol-4-yl)-3,4-dihydro-1H-benzo[e][1,4]diazepine-2,5-dione ((S)-19; LDM-3-47)



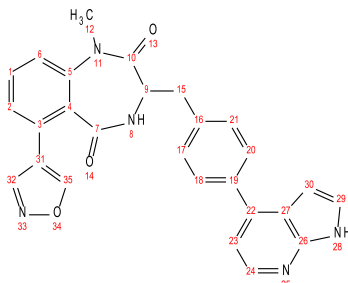
(S)-19 was prepared by GP2 (starting material: 6-bromoisatoic anhydride), GP3, GP4, GP6 (reagent: 4-(4,4,5,5-tetramethyl-1,3,2-dioxaborolan-2-yl)-1H-pyrrolo[2,3-b]pyridine), followed by an additional GP6 step (reagent: 4-pyrazole boronic acid pinacol ester). The resulting crude product was purified by flash chromatography [0-100%(10%MeOH/EA)/hex] to provide 3-(4-(1H-pyrrolo[2,3-b]pyridin-4-yl)benzyl)-1-methyl-6-(1H-pyrazol-4-yl)-3,4-dihydro-1H-benzo[e][1,4]diazepine-2,5-dione (overall yield= 16.4%) as an off-white solid; R_f= 0.35 (EA); Purity: overall= 97.9%, chiral= 95.7%; ¹H NMR (500 MHz) (δ/ppm) 3.22 (ddt, 1H, J=12.4, J=7.1, J=1.1, 15), 3.29 (ddt, 1H, J=12.4, J=7.1, J=1.1, 15'), 3.39 (s, 1H, 12), 4.90 (t, 1H, J=7.1, 9), 6.59 (d, 1H, J=12.4, J=7.1, J=1.1, 15'), 7.32 (dd, 2H, J=7.5, J=2.0, 6, 29), 7.42 (dt, 2H, J=7.5, J=1.1, 17, 21), 7.53 (d, 1H, J=1.5, 35), 7.60 (t, 1H, J=7.5, 1), 7.70 (m, 3H, 2, 18, 20), 8.05 (d, 1H, J=7.5, 23), 8.09 (d, 1H, J=1.5, 32), 8.71 (d, 1H, J=7.5, 24), 8.76 (s, 1H, 8), 11.72 (s, 1H, 28); ¹³C NMR (500 MHz) (δ/ppm) 33.4, 37.6, 54.3, 94.5, 115.9, 117.7, 119.4, 119.8, 122.7, 123.4, 126.2, 128.2, 128.9, 129.6, 130.6, 133.6, 134.7, 136.6, 137.4, 138.6, 145.1, 145.9, 148.4, 168.7, 170.7; Exact Mass (ES): determined mass: 462.1809 u, exact mass: 462.1804 u.

3-(4-(1H-pyrrolo[2,3-b]pyridin-4-yl)benzyl)-8,9-dichloro-1-methyl-3,4-dihydro-1H-benzo[e][1,4]diazepine-2,5-dione (rac-20; LDM-3-49)



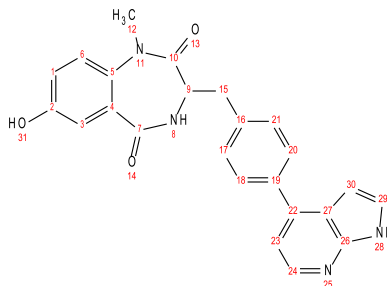
20 was prepared by GP1 (starting material: 2-amino-3,4-dichloro benzoic acid), GP2, GP3, GP4, and GP6 (reagent: 4-(4,4,5,5-tetramethyl-1,3,2-dioxaborolan-2-yl)-1H-pyrrolo[2,3-b]pyridine). The resulting crude product was purified by flash chromatography [0-100%(10%MeOH/EA)/hex] to provide 3-(4-(1H-pyrrolo[2,3-b]pyridin-4-yl)benzyl)-8,9-dichloro-1-methyl-3,4-dihydro-1H-benzo[e][1,4]diazepine-2,5-dione (overall yield= 45.5%) as an off-white solid; Rf= 0.35 (EA); Purity: overall= 97.0%; ¹H NMR (500 MHz) (δ/ppm) 3.10 (ddt, 1H, J=12.5, J=6.7, J=1.0, 23), 3.36 (s, 3H, 20), 3.52 (ddt, 1H, J=12.4, J=6.5, J=1.2, 23'), 4.99 (t, 1H, J=6.5, 17), 6.67 (d, 1H, J=7.5, 38), 7.38 (d, 1H, J=7.5, 37), 7.55 (ddd, 3H, J=7.5, J=2.9, J=1.8, 10, 25, 29), 7.80 (m, 2H, 26, 28), 7.84 (d, 1H, J=7.5, 11), 8.01 (d, 1H, J=7.5, 31), 8.05 (s, 1H, 16), 8.70 (d, 1H, J=7.5, 32), 11.83 (s, 1H, 36); ¹³C NMR (500 MHz) (δ/ppm) 37.4, 37.6, 54.3, 94.5, 115.9, 122.7, 123.4, 124.9, 127.6, 128.2, 129.6, 129.9, 131.6, 133.0, 134.7, 137.4, 138.6, 145.0, 145.1, 148.4, 168.5, 168.7; Exact Mass (ES): determined mass: 464.0811 u, exact mass: 464.0807 u.

3-(4-(1H-pyrrolo[2,3-b]pyridin-4-yl)benzyl)-6-(isoxazol-4-yl)-1-methyl-3,4-dihydro-1H-benzo[e][1,4]diazepine-2,5-dione ((S)-21; LDM-3-77)



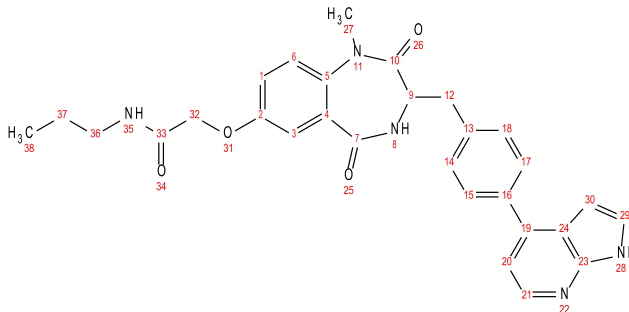
(S)-21 was prepared by GP1 (starting material: 2-amino-6-bromo benzoic acid), GP2, GP3, GP4, GP6 (reagent: 4-(4,4,5,5-tetramethyl-1,3,2-dioxaborolan-2-yl)-1H-pyrrolo[2,3-b]pyridine), followed by an additional GP6 step (reagent: 4-isoxazole boronic acid pinacol ester). The resulting crude product was purified by flash chromatography [0-100%(10%MeOH/EA)/hex] to provide 3-(4-(1H-pyrrolo[2,3-b]pyridin-4-yl)benzyl)-6-(isoxazol-4-yl)-1-methyl-3,4-dihydro-1H-benzo[e][1,4]diazepine-2,5-dione (overall yield= 14.7%) as an off-white solid; Rf= 0.35 (EA); Purity: overall= 96.9%, chiral= 97.0%; ¹H NMR (500 MHz) (δ/ppm) 3.26 (qdt, 2H, J=12.5, J=7.0, J=1.0, 23, 23'), 3.40 (s, 3H, 20), 4.90 (t, 1H, J=7.0, 17), 6.62 (d, 1H, J=75, 38), 7.4 (m, 2H, 14, 37), 7.45 (dt, 2H, J=7.4, J=1.1, 25, 29), 7.64 (t, 1H, J=7.5, 9), 7.70 (m, 3H, 10, 26, 28), 7.94 (d, 1H, J=1.5, 43), 8.05 (d, 1H, J=7.7, 31), 8.38 (d, 1H, J=1.5, 40), 8.70 (s, 1H, 16), 8.75 (d, 1H, J=7.5, 32), 11.73 (s, 1H, 36); ¹³C NMR (500 MHz) (δ/ppm) 33.4, 37.6, 54.3, 94.5, 115.9, 117.1, 120.6, 122.7, 123.4, 125.9, 126.8, 128.2, 129.5, 129.5, 131.9, 134.7, 137.4, 138.6, 144.8, 145.1, 148.4, 151.2, 156.5, 168.7, 170.7 ; Exact Mass (ES): determined mass: 463.1644 u, exact mass: 463.1644 u.

3-(4-(1H-pyrrolo[2,3-b]pyridin-4-yl)benzyl)-7-hydroxy-1-methyl-3,4-dihydro-1H-benzo[e][1,4]diazepine-2,5-dione ((S)-22; LDM-3-85)



(S)-22 was prepared by GP2 (starting material: 6-((tert-butyldimethylsilyl)oxy)-1H-benzo[d][1,3]oxazine-2,4-dione), GP3, GP4, GP6 (reagent: 4-(4,4,5,5-tetramethyl-1,3,2-dioxaborolan-2-yl)-1H-pyrrolo[2,3-b]pyridine), and GP7. The resulting crude product was purified by flash chromatography [0-100%(10%MeOH/EA)/hex] to provide 3-(4-(1H-pyrrolo[2,3-b]pyridin-4-yl)benzyl)-7-hydroxy-1-methyl-3,4-dihydro-1H-benzo[e][1,4]diazepine-2,5-dione (overall yield= 12.1%) as an off-white solid; R_f= 0.35 (EA); Purity: overall= 95.1%, chiral= 97.9%; ¹H NMR (500 MHz) (δ/ppm) 3.23 (ddt, 1H, J=12.4, J=7.3, J=1.1, 23), 3.30 (ddt, 1H, J=12.4, J=7.1, J=1.0, 23'), 4.88 (t, 1H, J=7.2, 17), 6.90 (d, 1H, J=7.5, 38), 7.06 (dd, 1H, J=7.5, J=2.0, 9), 7.40 (m, 3H, 25, 29, 37), 7.46 (d, 1H, J=7.5, 14), 7.49 (d, 1H, J=2.0, 11), 7.80(m, 2H, 26, 28), 7.95 (d, 1H, J=7.5, 31), 8.50 (s, 1H, 16), 8.69 (d, 1H, J=7.5, 32), 10.61 (s, 1H, 39), 11.83 (s, 1H, 36); ¹³C NMR (500 MHz) (δ/ppm) 36.8, 36.8, 56.8, 94.9, 110.5, 116.7, 117.1, 121.9, 123.0, 125.6, 126.9, 129.2, 129.7, 131.8, 133.7, 137.4, 139.8, 147.1, 147.3, 151.7, 167.3, 168.4 ; Exact Mass (ES): determined mass: 463.1646 u, exact mass: 463.1644 u.

2-((3-(4-(1H-pyrrolo[2,3-b]pyridin-4-yl)benzyl)-1-methyl-2,5-dioxo-2,3,4,5-tetrahydro-1H-benzo[e][1,4]diazepin-7-yl)oxy)-N-propylacetamide ((S)-23; LDM-4-17).

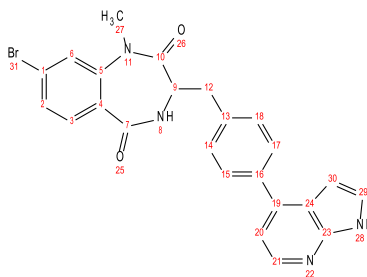


(S)-23 was prepared using GP2 (starting material: starting material: 6-((tert-butyl dimethylsilyl)oxy)-1H-benzo[d][1,3]oxazine-2,4-dione), GP3, GP4, GP7, GP8 (reagent: 2-bromo-N-propylacetamide) and GP6 (reagent: 4-(4,4,5,5-tetramethyl-1,3,2-dioxaborolan-2-yl)-1H-pyrrolo[2,3-b]pyridine). The resulting crude product was purified by flash chromatography [0-100%(10%MeOH/EA)/hex] to provide 2-((3-(4-(1H-pyrrolo[2,3-b]pyridin-4-yl)benzyl)-1-methyl-2,5-dioxo-2,3,4,5-tetrahydro-1H-benzo[e][1,4]diazepin-7-yl)oxy)-N-propylacetamide (overall yield= 8.2%) as an off-white solid; R_f= 0.35 (EA); Purity: overall= 98.4%, chiral= 96.1%; ¹H NMR (500 MHz) (δ/ppm) 0.81 (t, 3H, J=6.7, 38), 1.34 (qt, 2H, J=6.6, J=5.0, 37), 3.15 (t, 1H, J=5.0, 36), 3.20 (ddt, 1H, J=12.4, J=6.7, J=1.1, 12), 3.31 (ddt, 1H, J=12.6, J=6.9, 12'), 3.37 (t, 1H, J=5.0, 36'), 3.41 (s, 3H, 27), 4.45 (s, 2H, 32), 5.02 (t, 1H, J=6.6, 9), 6.61 (d, 1H, J=7.5), 7.09 (dd, 1H, J=7.5, J=1.9, 1), 7.33 (d, 1H, J=7.5, 29), 7.41 (dt, 2H, J=7.2, J=0.9, 14), 7.55 (d, 1H, J=7.5, 6), 7.7 (m, 3H, 3, 15, 17), 7.88 (d, 1H, J=7.5, 20), 8.15 (s, 1H, 35), 8.19 (s, 1H, 8), 8.63 (d, 1H, J=7.5, 21), 11.73 (s, 1H, 28); ¹³C NMR (500 MHz) (δ/ppm) 11.9, 23.9, 36.8, 36.8, 42.6, 56.8, 67.8, 94.9, 110.5, 116.7, 117.5, 118.7, 123.0, 124.7, 126.9,

129.7, 132.9, 133.7, 134.1, 137.4, 139.8, 147.1, 147.3, 158.5, 167.3, 168.4, 170.7;

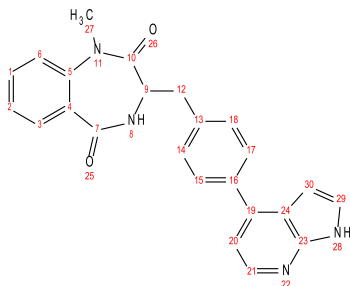
Exact Mass (ES): determined mass: 511.5726 u, exact mass: 511.5717 u.

3-(4-(1H-pyrrolo[2,3-b]pyridin-4-yl)benzyl)-8-bromo-1-methyl-3,4-dihydro-1H-benzo[e][1,4]diazepine-2,5-dione ((S)-24; LDM-4-13).



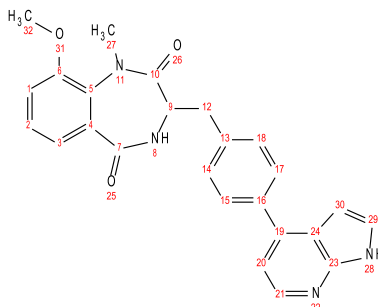
(S)-24 was prepared by GP2 (starting material: 4-bromoisatoic anhydride), GP3, GP4, and GP6 (reagent: 4-(4,4,5,5-tetramethyl-1,3,2-dioxaborolan-2-yl)-1H-pyrrolo[2,3-b]pyridine). The resulting crude product was purified by flash chromatography [0-100%(10%MeOH/EA)/hex] to provide 3-(4-(1H-pyrrolo[2,3-b]pyridin-4-yl)benzyl)-8-bromo-1-methyl-3,4-dihydro-1H-benzo[e][1,4]diazepine-2,5-dione (overall yield= 44.1%) as an off-white solid; R_f= 0.35 (EA); Purity: overall= 96.0%, chiral= 96.4%; ¹H NMR (500 MHz) (δ/ppm) 3.11 (ddt, 1H, J=12.5, J=6.2, J=1.1, 12), 3.39 (s, 3H, 27), 3.44 (ddt, 1H, J=12.4, J=6.2, J=1.0, 12'), 5.00 (t, 1H, J=6.2, 9), 6.71 (d, 1H, J=7.5, 30), 7.30 (m, 2H, 6, 29), 7.47 (dt, 2H, J=7.3, J=1.1, 14, 18), 7.66 (dd, 1H, J=7.6, J=2.0, 2), 7.75 (d, 2H, J=7.4, 15, 17), 7.92 (dd, 2H, J=7.5, J=6.5, 3, 20), 8.17 (s, 1H, 8), 8.68 (d, 1H, J=7.5, 21), 11.78 (s, 1H, 28); ¹³C NMR (500 MHz) (δ/ppm) 36.8, 36.8, 56.8, 94.9, 110.5, 116.7, 122.4, 123.0, 126.9, 127.0, 129.1, 129.7, 132.6, 132.7, 133.7, 137.4, 139.8, 143.3, 147.1, 147.3, 167.3, 168.3; Exact Mass (ES): determined mass: 474.0699 u, exact mass: 474.0691 u.

3-(4-(1H-pyrrolo[2,3-b]pyridin-4-yl)benzyl)-1-methyl-3,4-dihydro-1H-benzo[e][1,4]diazepine-2,5-dione ((S)-25; LDM-4-49).



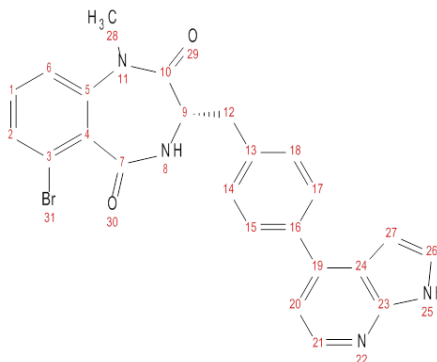
(S)-25 was prepared by GP3 (N-methylisatoic anhydride), GP4, and GP6 (reagent: 4-(4,4,5,5-tetramethyl-1,3,2-dioxaborolan-2-yl)-1H-pyrrolo[2,3-b]pyridine). The resulting crude product was purified by flash chromatography [0-100%(10%MeOH/EA)/hex] to provide 3-(4-(1H-pyrrolo[2,3-b]pyridin-4-yl)benzyl)-1-methyl-3,4-dihydro-1H-benzo[e][1,4]diazepine-2,5-dione (overall yield= 56.8%) as an off-white solid; R_f= 0.35 (EA); Purity: overall= 96.1%, chiral= 97.9%; ¹H NMR (δ/ppm) 3.16 (ddt, 1H, J=12.6, J=6.9, J=1.1, 12), 3.40 (m, 4H, 12', 27), 4.90 (t, 1H, J=6.8, 9), 6.65 (d, 1H, J=7.5, 30), 7.20 (m, 1H, 6), 7.31 (d, 1H, J=7.5, 29), 7.35 (td, 1H, J=7.5, J=2.0, 2), 7.41 (dt, 2H, J=7.4, J=1.1, 14, 18), 7.70 (d, 2H, J=7.5, 15, 17), 7.77 (td, 1H, J=7.5, J=2.0, 1), 7.87 (d, 1H, J=7.5, 20), 7.97 (dd, 1H, J=7.5, J=1.9, 3), 8.56 (s, 1H, 8), 8.63 (d, 1H, J=7.5, 21), 11.71 (s, 1H, 28); ¹³C NMR (500 MHz) (δ/ppm) 36.8, 36.8, 56.8, 94.9, 110.5, 116.7, 120.4, 122.6, 123.0, 124.4, 126.9, 129.7, 129.8, 131.0, 133.7, 137.4, 139.8, 140.7, 147.1, 147.3, 167.3, 168.3; Exact Mass (ES): determined mass: 396.1595 u, exact mass: 396.1586 u.

(S)-3-(4-(1H-pyrrolo[2,3-b]pyridin-4-yl)benzyl)-9-methoxy-1-methyl-3,4-dihydro-1H-benzo[e][1,4]diazepine-2,5-dione ((S)-26; LDM-4-57).



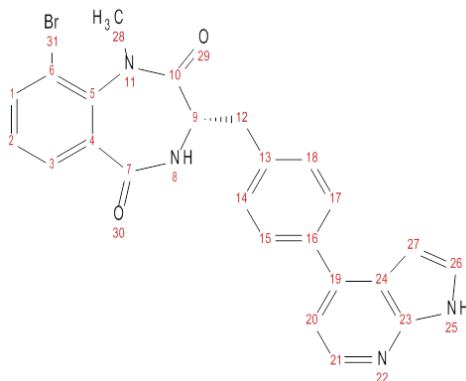
(S)-26 was prepared by GP2 (starting material: 8-methoxy-1H-benzo[d][1,3]oxazine-2,4-dione), GP3, GP4, and GP6 (reagent: 4-(4,4,5,5-tetramethyl-1,3,2-dioxaborolan-2-yl)-1H-pyrrolo[2,3-b]pyridine). The resulting crude product was purified by flash chromatography [0-100%(10%MeOH/EA)/hex] to provide (S)-3-(4-(1H-pyrrolo[2,3-b]pyridin-4-yl)benzyl)-9-methoxy-1-methyl-3,4-dihydro-1H-benzo[e][1,4]diazepine-2,5-dione (overall yield= 46.6%) as an off-white solid; R_f= 0.35 (EA); Purity: overall= 98.1%, chiral= 99.0%; ¹H NMR (500 MHz) (δ/ppm) 3.24 (qdt, 2H, J=12.4, J=6.6, J=1.1, 20, 20'), 3.39 (s, 3H, 35), 3.86 (s, 3H, 40), 4.96 (t, 1H, J=6.5, 17), 6.87 (d, 1H, J=7.4, 38), 7.14 (dd, 1H, J=7.5, J=1.9, 9), 7.40 (m, 2H, 10, 37), 7.51 (dt, 2H, J=7.3, J=1.1, 22, 26), 7.65 (dd, 1H, J=7.6, J=2.0, 11), 7.79 (d, 1H, J=7.6, 23, 25), 7.94 (d, 1H, J=7.5, 28), 8.59 (s, 1H, 16), 8.67 (d, 1H, J=7.7, 29), 11.74 (s, 1H, 36); ¹³C NMR (500 MHz) (δ/ppm) 37.7, 37.8, 56.0, 56.3, 94.9, 110.6, 112.9, 116.9, 123.9, 125.7, 126.9, 127.1, 129.8, 130.3, 133.8, 135.2, 136.9, 139.8, 147.5, 147.6, 159.4, 165.1, 168.4; Exact Mass (ES): determined mass: 426.1697 u, exact mass: 426.1692 u.

3-(4-(1H-pyrrolo[2,3-b]pyridin-4-yl)benzyl)-6-bromo-1-methyl-3,4-dihydro-1H-benzo[e][1,4]diazepine-2,5-dione ((S)-28; LDM-4-33).



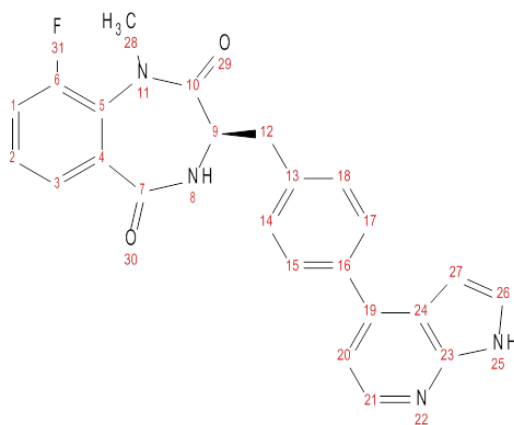
(S)-28 was prepared by GP1 (starting material: 2-amino-6-bromobenzoic acid), GP2, GP3, GP4, and GP6 (reagent: 4-(4,4,5,5-tetramethyl-1,3,2-dioxaborolan-2-yl)-1H-pyrrolo[2,3-b]pyridine). The resulting crude product was purified by flash chromatography [0-100%(10%MeOH/EA)/hex] to provide 3-(4-(1H-pyrrolo[2,3-b]pyridin-4-yl)benzyl)-6-bromo-1-methyl-3,4-dihydro-1H-benzo[e][1,4]diazepine-2,5-dione (overall yield= 32.1%) as an off-white solid; R_f= 0.33 (EA); Purity: overall= 96.1%, chiral= 97.9%; ¹H NMR (500 MHz) (δ/ppm) 3.23 (m, 1H, 12), 3.31 (m, 1H, 12'), 3.37 (s, 3H, 28), 4.84 (t, 1H, J=6.4, 9), 6.57 (d, 1H, J=7.5, 27), 7.17 (dd, 1H, J=7.4, J=1.9, 6), 7.35 (m, 2H, 1, 26), 7.38 (dt, 2H, J=7.4, J=1.1, 14, 18), 7.60 (dd, 1H, J=7.5, J=2.2, 2), 7.69 (m, 2H, 15, 17), 7.84 (d, 1H, J=7.5, 20), 8.39 (s, 1H, 8), 8.63 (d, 1H, J=7.5, 21), 11.71 (s, 1H, 25). ¹³C NMR (500 MHz) (δ/ppm) 36.7, 37.7, 55.0, 94.9, 110.6, 116.9, 121.1, 123.9, 124.0, 126.9, 129.8, 130.1, 131.2, 132.7, 133.8, 136.9, 139.8, 142.1, 147.5, 147.6, 167.0, 168.7; Exact Mass(ES): determined mass: 474.0698 u, exact mass: 474.0691 u.

3-(4-(1H-pyrrolo[2,3-b]pyridin-4-yl)benzyl)-9-bromo-1-methyl-3,4-dihydro-1H-benzo[e][1,4]diazepine-2,5-dione ((S)-29; LDM-4-45).



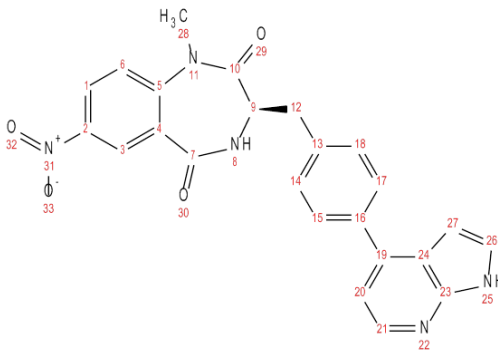
(S)-29 was prepared by GP1 (starting material: 2-amino-3-bromobenzoic acid), GP2, GP3, GP4, and GP6 (reagent: 4-(4,4,5,5-tetramethyl-1,3,2-dioxaborolan-2-yl)-1H-pyrrolo[2,3-b]pyridine). The resulting crude product was purified by flash chromatography [0-100%(10%MeOH/EA)/hex] to provide 3-(4-(1H-pyrrolo[2,3-b]pyridin-4-yl)benzyl)-9-bromo-1-methyl-3,4-dihydro-1H-benzo[e][1,4]diazepine-2,5-dione (overall yield= 38.9%) as an off-white solid; Rf= 0.36 (EA); Purity: overall= 96.0%, chiral= 97.6%; ¹H NMR (500 MHz) (δ/ppm) 3.22 (dt, 1H, J=6.7, J=1.0, 12), 3.23 (dt, 1H, J=6.6, 1.0, 12'), 3.40 (s, 3H, 28), 4.85 (t, 1H, J=6.6, 9), 6.57 (d, 1H, J=7.5, 27), 7.32 (t, 2H, J=7.5, 2, 26), 7.35 (d, 2H, J=10.9, 14, 18), 7.67 (m, 2H, 15, 17), 7.73 (dd, 1H, J=7.7, J=1.9, 1), 7.83 (d, 1H, J=7.5, 20), 7.87 (dd, 1H, J=7.5, J=1.9, 3), 8.14 (s, 1H, 8), 8.62 (d, 1H, J=7.5, 21), 11.71 (s, 1H, 25). ¹³C NMR (500 MHz) (δ/ppm) 37.7, 37.8, 55.0, 94.9, 110.6, 116.9, 118.2, 123.9, 126.9, 127.7, 129.4, 129.5, 129.8, 133.8, 134.3, 136.9, 139.8, 141.6, 147.5, 147.6, 165.1, 168.4; Exact Mass (ES): determined mass: 474.0701 u, exact mass: 474.0691 u.

3-(4-(1H-pyrrolo[2,3-b]pyridin-4-yl)benzyl)-9-fluoro-1-methyl-3,4-dihydro-1H-benzo[e][1,4]diazepine-2,5-dione ((R)-30; LDM-4-53).



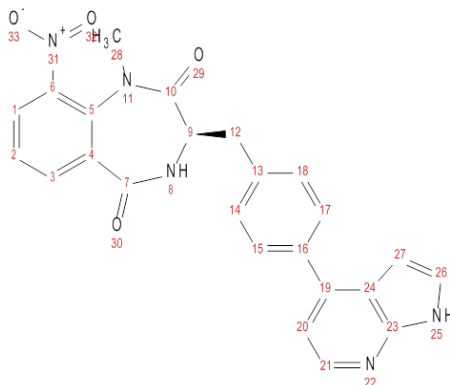
(R)-30 was prepared by GP1 (starting material: 2-amino-3-fluorobenzoic acid), GP2, GP3, GP4, and GP6 (reagent: 4-(4,4,5,5-tetramethyl-1,3,2-dioxaborolan-2-yl)-1H-pyrrolo[2,3-b]pyridine). The resulting crude product was purified by flash chromatography [0-100%(10%MeOH/EA)/hex] to provide 3-(4-(1H-pyrrolo[2,3-b]pyridin-4-yl)benzyl)-9-fluoro-1-methyl-3,4-dihydro-1H-benzo[e][1,4]diazepine-2,5-dione (overall yield= 41.1%) as an off-white solid; R_f= 0.35 (EA); Purity: overall= 95.9%, chiral= 96.8%; ¹H NMR (500 MHz) (δ/ppm) 3.25 (qdt, 2H, J=12.4, J=6.9, J=1.2, 12, 12'), 3.44 (s, 3H, 28), 4.85 (t, 1H, J=6.8, 9), 6.58 (d, 1H, J=7.5, 27), 7.32 (d, 1H, J=7.7, 26), 7.45 (m, 4H, 1, 2, 14, 18), 7.68 (m, 2H, 15, 17), 7.71 (dd, 1H, J=6.8, J=2.6, 3), 7.84 (d, 1H, J=7.5, 20), 8.12 (s, 1H, 8), 8.62 (d, 1H, J=7.5, 21), 11.72 (s, 1H, 25); ¹³C NMR (500 MHz) (δ/ppm) 37.7, 37.8, 37.8, 55.0, 94.9, 110.6, 116.9, 117.2, 117.4, 123.9, 126.9, 127.6, 127.6, 127.9, 128.0, 129.8, 130.7, 130.7, 133.8, 135.3, 135.5, 136.9, 139.8, 147.5, 147.6, 158.5, 160.5, 165.0, 165.1, 168.4, 168.5; Exact Mass (ES): determined mass: 414.1497 u, exact mass: 414.1492 u.

3-(4-(1H-pyrrolo[2,3-b]pyridin-4-yl)benzyl)-1-methyl-7-nitro-3,4-dihydro-1H-benzo[e][1,4]diazepine-2,5-dione ((R)-31; LDM-4-55).



(R)-31 was prepared by GP1 (starting material: 2-amino-5-nitrobenzoic acid), GP2, GP3, GP4, and GP6 (reagent: 4-(4,4,5,5-tetramethyl-1,3,2-dioxaborolan-2-yl)-1H-pyrrolo[2,3-b]pyridine). The resulting crude product was purified by flash chromatography [0-100%(10%MeOH/EA)/hex] to provide 3-(4-(1H-pyrrolo[2,3-b]pyridin-4-yl)benzyl)-1-methyl-7-nitro-3,4-dihydro-1H-benzo[e][1,4]diazepine-2,5-dione (overall yield= 36.0%) as an off-white solid; R_f= 0.30 (EA); Purity: overall= 96.9%, chiral= 97.0%; ¹H NMR (500 MHz) (δ/ppm) 3.25 (qdt, 2H, J=12.5, J=6.9, J=1.0, 12, 12'), 3.41 (s, 3H, 28), 4.85 (t, 1H, J=6.8, 9), 6.54 (d, 1H, J=7.5, 27), 7.32 (d, 1H, J=7.5, 26), 7.36 (dt, 2H, J=7.6, J=1.1, 14, 18), 7.41 (d, 1H, J=7.6, 6), 7.68 (m, 2H, 15, 17), 7.85 (d, 1H, J=7.7, 20), 8.14 (s, 1H, 8), 8.38 (dd, 1H, J=7.6, J=2.0, 1), 8.63 (d, 1H, J=7.5, 21), 8.83 (d, 1H, J=2.0, 3), 11.72 (s, 1H, 25); ¹³C NMR (500 MHz) (δ/ppm) 36.7, 37.7, 55.0, 94.9, 110.6, 116.9, 122.9, 123.9, 124.2, 126.1, 126.9, 129.7, 129.8, 133.8, 136.9, 139.8, 143.3, 147.2, 147.5, 147.6, 167.0, 168.4; Exact Mass (ES): determined mass: 441.1447 u, exact mass: 441.1437 u.

3-(4-(1H-pyrrolo[2,3-b]pyridin-4-yl)benzyl)-1-methyl-9-nitro-3,4-dihydro-1H-benzo[e][1,4]diazepine-2,5-dione ((R)-33; LDM-4-85).



(R)-33 was prepared by GP1 (starting material: 2-amino-3-nitrobenzoic acid), GP2, GP3, GP4, and GP6 (reagent: 4-(4,4,5,5-tetramethyl-1,3,2-dioxaborolan-2-yl)-1H-pyrrolo[2,3-b]pyridine). The resulting crude product was purified by flash chromatography [0-100%(10%MeOH/EA)/hex] to provide 3-(4-(1H-pyrrolo[2,3-b]pyridin-4-yl)benzyl)-1-methyl-9-nitro-3,4-dihydro-1H-benzo[e][1,4]diazepine-2,5-dione (overall yield= 38.2%) as an off-white solid; R_f= 0.30 (EA); Purity: overall= 96.1%, chiral= 97.4%; ¹H NMR (500 MHz) (δ/ppm) 3.32 (m, 5H, 12, 12', 28), 4.88 (t, 1H, J=6.7, 9), 6.58 (d, 1H, J=7.5, 27), 7.31 (d, 1H, J=7.5, 26), 7.38 (dt, 2H, J=7.4, J=1.0, 14, 18), 7.58 (t, 1H, J=7.5, 2), 7.69 (m, 2H, 15, 17), 7.85 (d, 1H, J=7.5, 20), 8.16 (s, 1H, 8), 8.19 (dd, 1H, J=7.5, J=2.1, 1), 8.23 (dd, 1H, J=7.6, J=2.0, 3), 8.63 (d, 1H, J=7.5, 21), 11.71 (s, 1H, 25); ¹³C NMR (500 MHz) (δ/ppm) 37.7, 37.8, 55.0, 94.9, 110.6, 116.9, 123.9, 126.9, 127.2, 129.3, 129.8, 132.1, 133.8, 134.7, 136.9, 139.8, 140.3, 145.5, 147.5, 147.6, 165.1, 168.4; Exact Mass (ES): determined mass: 441.1447 u, exact mass: 441.1437 u.

References

1. Kutter, E.; et al. Steric parameters in drug design. Monoamine oxidase inhibitors and antihistamines. *J. Med. Chem.* **1969**, *12*, 647.
2. Hansch, C.; et al. ρ - σ - π analysis. A method for the correlation of biological activity and chemical structure. *J. Am. Chem. Soc.* **1963**, *86*, 1616.
3. Fujita, T.; et al. A new substituent constant, π , derived from partition coefficients. *J. Am. Chem. Soc.* **1964**, *86*, 5175.
4. Hansch, C.; et al. The effect of intramolecular hydrophobic bonding on partition coefficients. *J. Org. Chem.* **1967**, *32*, 2583.
5. Bott, G; et al. Steric effects. A study of a rationally designed system. *J. Am. Chem. Soc.* **1980**, *102*, 5618.
6. Hansch, C.; et al. Aromatic substituent constants for structure-activity correlations. *J. Med. Chem.* **1973**, *16*, 1207.
7. Ney, G.M. Molecular recognition of small molecules by the mitochondrial F_1F_0 -ATPase. Ph.D. Dissertation, University of Michigan, Ann Arbor, Michigan. 2007
8. Free, S.M.; et al. A mathematical contribution to structure-activity studies. *J. Med. Chem.* **1964**, *7*, 395.
9. Kubinyi, H. QSAR and 3D QSAR in drug design Part 1: methodology. *Drug Discov. Today* **1997**, *2*, 457.
10. Craig, P.N.; et al. Minimal statistical data for structure-function correlations. *J. Med. Chem.* **1971**, *14*, 447.
11. Wermuth, C.G. *The Practice of Medicinal Chemistry*, 2nd ed.; Academic Press: Waltham, 2003.

12. Topliss, J.G.; et al. Chance correlations in structure-activity studies using multiple regression analysis. *J. Med. Chem.* **1972**, *15*, 1066.
13. Topliss, J.G. A manual method for applying the Hansch approach to drug design. *J. Med Chem.* **1977**, *20*, 463.
14. Craig, P.N. Interdependence between physical parameters and selection of substituent groups for correlation studies. *J. Med. Chem.* **1971**, *14*, 680.
15. Topliss, J.G. Utilization of operational schemes for analog synthesis in drug design. *J. Med. Chem.* **1972**, *15*, 1006.
16. Evans, B.E.; et al. Methods for drug discovery: development of potent, selective, orally effective cholecystinin antagonists. *J. Med. Chem.* **1988**, *31*, 2235.
17. DeSimone, R.W.; et al. Privileged structures: applications in drug discovery. *Comb Chem High Throughput Screen* **2004**, *7*, 473-494.
18. Costantino, L.; et al. Privileged structures as leads in medicinal chemistry. *Curr Med Chem* **2006**, *13*, 65-85.
19. Cambridge MedChem Consulting. Privileged Structures. www.cambridgemedchemconsulting.com/resource/hit_identification/privileged_structures.html (accessed Aug 18, 2013).
20. Muller, K. In *Topics in Structure-Based Molecular Design in Drug Discovery. Part I: Privileged Structures*. Lecture, ETH Zurich. Zurich, Switzerland, 2011.
21. Ripka W.C.; et al. Protein beta-turn mimetics. I. Design, synthesis, and evaluation in model cyclic peptides. *Tetrahedron* **1993**, *49*, 3593-3608.
22. Russel, S.J.; et al. Stability of cyclic beta-hairpins: asymmetric contributions from side chains of a hydrogen-bonded cross-strand residue pair. *J Am Chem Soc* **2003**, *125*, 388-395.
23. Olsen R.W.; et al. *Basic Neurochemistry: Molecular, Cellular and Medical Aspects*, 7th ed.; Academic Press: Waltham, 2005.

24. Derry, J.M.; et al. Identification of a residue in the gamma-aminobutyric acid type A receptor alpha subunit that differentially affects diazepam-sensitive and -insensitive benzodiazepine site binding. *J Neurochem* **2004**, *88*, 1431-1438.
25. Sigel, E.; et al. A gamma-aminobutyric acid/benzodiazepine receptor complex of bovine cerebral cortex. *J Biol Chem* **1983**, *258*, 6965-6971.
26. Araujo, A.C.; et al. Synthesis and Biological Evaluation of Novel Rigid 1,4-Benzodiazepine-2,5-dione Chimeric Scaffolds. *Eur J Org Chem* **2008**, *4*, 635-639.
27. Ramdas, L.; et al. Benzodiazepine compounds as inhibitors of the src protein tyrosine kinase: screening of a combinatorial library of 1,4-benzodiazepines. *Arch Biochem Biophys* **1999**, *368*, 394-400.
28. Borowicz, K.K.; et al. Influence of the combined treatment of LY 300164 (an AMPA/kainate receptor antagonist) with adenosine receptor agonists on the electroconvulsive threshold in mice. *Eur Neuropsychopharmacol* **2004**, *14*, 407-412.
29. Abraham, G.; et al. New non-competitive AMPA antagonists. *Bioorg Med Chem* **2000**, *8*, 2127-2143.
30. Wyatt, P.G.A.; et al. Structure–Activity Relationship Investigations of a Potent and Selective Benzodiazepine Oxytocin Antagonist. *Bioorganic & Medicinal Chemistry Letters* **2001**, *11*, 1301-1305.
31. Xu, X.S.; et al. Increasing I9Ks corrects abnormal repolarization in rabbit models of acquired LQT2 and ventricular hypertrophy. *Am J Physiol Heart Circ Physiol* **2002**, *283*, H664-670.
32. Stump, G.L.; et al. In vivo canine cardiac electrophysiologic profile of 1,4-benzodiazepine IKs blockers. *J Cardiovasc Pharmacol* **2003**, *42*, 105-112.
33. Seebohm, G.; et al. Pharmacological activation of normal and arrhythmia-associated mutant KCNQ1 potassium channels. *Circ Res* **2003**, *93*, 941-947.
34. Giragossian, C.; et al. Intermolecular interactions between peptidic and nonpeptidic agonists and the third extracellular loop of the cholecystokinin 1 receptor. *J Med Chem* **2003**, *46*, 3476-3482.

35. Agrawal, V.K.; et al. Quantitative structure-activity relationship studies on 5-phenyl-3-ureido-1,5-benzodiazepine as cholecystokinin-A receptor antagonists. *Bioorg Med Chem* **2002**, *10*, 3571-3581.
36. Kimura, T.; et al. A non-peptide compound which can mimic the effect of thrombopoietin via c-Mpl. *FEBS Lett* **1998**, *428*, 250-254.
37. Pascal, Y.; et al. Synthesis and structure-activity relationships of 4-oxo-1-phenyl-3,4,6,7-tetrahydro-[1,4]diazepino[6,7,1-hi]indoles: novel PDE4 inhibitors. *Bioorg Med Chem Lett* **2000**, *10*, 35-38.
38. Anzini, M.; et al. Synthesis, biological evaluation, and receptor docking simulations of 2-[(acylamino)ethyl]-1,4-benzodiazepines as kappa-opioid receptor agonists endowed with antinociceptive and anti-amnesic activity. *J Med Chem* **2003**, *46*, 3853-3864.
39. Ashwell, M.A.; et al. The design, synthesis and physical chemical properties of novel human vasopressin V2-receptor antagonists optimized for parenteral delivery. *Bioorg Med Chem Lett* **2000**, *10*, 783-786.
40. Marceau, F.; et al. Effects of two novel non-peptide antagonists at the rabbit bradykinin B2 receptor. *Peptides* **2001**, *22*, 1397-1402.
41. Keenan, R.M.; et al. Conformational preferences in a benzodiazepine series of potent nonpeptide fibrinogen receptor antagonists. *J Med Chem* **1999**, *42*, 545-559.
42. Mischiati, C.; et al. Binding of hybrid molecules containing pyrrolo [2,1-c][1,4]benzodiazepine (PBD) and oligopyrrole carriers to the human immunodeficiency type 1 virus TAR-RNA. *Biochem Pharmacol* **2004**, *67*, 401-410.
43. Smith, R.H.; et al. Prediction of binding affinities for TIBO inhibitors of HIV-1 reverse transcriptase using Monte Carlo simulations in a linear response method. *J Med Chem* **1998**, *41*, 5272-5286.
44. Cheng, M.F.; et al. Practical synthesis of potential endothelin receptor antagonists of 1,4-benzodiazepine-2,5-dione derivatives bearing substituents at the C3-, N1- and N4-positions. *Org Biomol Chem* **2006**, *4*, 510-518.

45. Joseph, C.G.; et al. The 1,4-benzodiazepine-2,5-dione small molecule template results in melanocortin receptor agonists with nanomolar potencies. *J Med Chem* **2008**, *51*, 1423-1431.
46. Nguyen, P.; et al. Mechanisms of the platelet aggregation induced by activated neutrophils and inhibitory effect of specific PAF receptor antagonists. *Thromb Res* **1995**, *78*, 33-42.
47. McDowell, R.S.B.; et al. From Peptide to Non-Peptide. 2. The de Novo Design of Potent, Non-Peptidal Inhibitors of Platelet Aggregation Based on Benzodiazepine Scaffold. *Journal of the American Chemical Society* **1994**, *116*, 5077-5083.
48. Paloma, V.; et al. 5-Imino-1,2,4-Thiadiazoles: First Small Molecules As Substrate Competitive Inhibitors of Glycogen Synthase Kianse 3. *J. Med. Chem.* **2012**, *55*, 1645-166.
49. Klebl, B.; et al. *Protein Kinases as Drug Targets*. WILEY-VCH Verlag GmbH & Co.: Weinheim, 2011.
50. Eason, I.H.; et al. The absolute activity of choline-esterase. *Proceedings of the Royal Society of London. Series B, Biological Sciences* **1936**, *121*, 142–164.
51. Strauss, O.H.; et al. Zone behaviour of enzymes. *The Journal of General Physiology* **1943**, *26*, 559–585.
52. Cheng, Y.C.; Prusoff, W.H. Relationship between the inhibition constant (K₁) and the concentration of inhibitor which causes 50 per cent inhibition (I₅₀) of an enzymatic reaction. *Biochemical Pharmacology* **1973**, *22*, 3099–3108.
53. Genetic Engineering & Biotechnology News. Drug Discovery: Successful Lead Optimization Strategies. <http://www.genengnews.com/gen-articles/drug-discovery-successful-lead-optimization-strategies/1825/> (accessed Aug 18, 2013).
54. Anastassiadis, T.; et al. Comprehensive assay of kinase catalytic activity reveals features of kinase inhibitor selectivity. *Nature Biotechnology*. **2011**, *29*, 1039-1045.
55. Francis, T.M. Target identification and validation of a novel family of anti-inflammatory 1,4-benzodiazpeine-2,5-diones. Ph.D. Dissertation, University of Michigan, Ann Arbor, Michigan, 2010.

56. Prieto, M.; et al. Arylboronic acids and arylpinacolboronate esters in Suzuki coupling reactions involving indoles. Partner role swapping and heterocycle protection. *J. Org. Chem.* **2004**, *69*, 6812-6820.
57. Miller, D. personal communication, February 2013.
58. Doran, J.D. New insights into the structure-function relationships of Rho-associated kinase: a thermodynamic and hydrodynamic study of the dimer-to-monomer transition and its kinetic implications. *Biochem. J.* **2004**, *384*, 255-262.
59. Barnett, S. F.; et al. Identification and characterization of pleckstrin-homology-domain-dependent and isoenzyme-specific Akt inhibitors. *Biochemical Journal* **2005**, *385*, 399-408.
60. Verri, A.; et al. L-ATP is recognized by some cellular and viral enzymes: does chance drive enzymic enantioselectivity? *Biochem. J.* **1999**, *337*, 585-590.
61. Horiuchi, K. *HotSpot Kinase Ki Studies*; 20120224-UMich-LDM-ROCK-MOA-RV02; Reaction Biology Corp.: Malvern, PA, 2012.
62. Wang, Y.; et al. Mixed inhibition of adenosine deaminase activity by 1,3-dinitrobenzene: a model for understanding cell-selective neurotoxicity in chemically-induced energy deprivation syndromes in brain. *Toxicol Sci* **2012**, *125*, 509-521.
63. Jacobs, M.; et al. The structure of dimeric ROCK1 reveals the mechanism for ligand selectivity. *J Biol Chem* **2006**, *281*, 260-268.
64. Enzyme Inhibition.
http://www.wiley.com/college/boyer/0470003790/animations/enzyme_inhibition/enzyme_inhibition.swf (accessed August 18, 2013).

Chapter 3

STRUCTURE-BASED DESIGN IN LEAD OPTIMIZATION

Introduction

The crystal structures of ROCKI and ROCKII, co-crystallized with Fasudil, were determined in 2006 and have significantly aided the discovery and design of new inhibitors¹⁻⁷. When using molecular modeling to predict successful new inhibitors, there are typically two basic approaches, including lead optimization of known compounds and fragment-based methods^{8,9}. Lead optimization involves manually building out from a previously established lead molecule, docked in its target receptor by a ligand-docking protocol, in order to make specific contacts or to improve non-specific contacts. However, fragment-based design involves the virtual screening of a library of chemical fragments for high binding affinity to the target, followed by the arrangement of the most successful fragments onto a template. Both approaches have been utilized in the design of ROCK inhibitors¹⁰, however, because a lead had previously been established (**BZD-29**) in this project, its template was maintained and optimized toward potent and selective inhibition of the targets. A pseudo-fragment based approach was involved however, in which fragments which formed desirable contacts were built onto the **BZD-29** template. These constructs were then screened and those which maintained the contacts seen in the fragments alone were then considered for synthesis.

The Glide-Prime algorithm. The interaction of **BZD-29** with ROCKI and ROCKII was modeled to aid in lead optimization using the Glide-Prime software package¹¹. By allowing side-chains to sample degrees of freedom in the receptor and by allowing minor movements of the backbone, the Glide-Prime algorithm accounts for flexibility of the ligand and the receptor^{11,12}. Specifically, through the introduction of loop predictions in the protocol, protein flexibility is addressed by this algorithm^{11,13}. Because ROCKI and ROCKII experience large changes in the conformations of loops upon binding of a ligand, this feature was especially important^{1,10,11,14}.

The Glide-Prime algorithm has been shown to be more accurate than other modeling programs in producing simulations of ligand:protein complexes which accurately reproduce crystallized complexes^{11,15}. In one examination, Glide-Prime generated poses for 72 non-covalently bound, co-crystallized ligands with an average RMSD of 1.46 Å (**Table 3.1**). ROCKII selective inhibitors (such as SR3677) have also been designed using Glide-Prime⁷. For example, a lead identified in a high-throughput screen was used along with this software in the design of new inhibitors with 20-fold selectivity for ROCKII versus ROCKI⁷.

Table 3.1 Representative ligand RMSDs for Glide-Prime induced fit docking of ligands from the indicated PDB structure into PDB receptor structures¹⁶.

Target	Receptor (PDB name)	Ligand from:	Ligand RMSD (Å)
Aldose reductase	2acr	1ah3	0.9
Antibody DB3	1dba	1dbb	0.3
CDK2^a	1buh	1dm2	1.1
CDK2^b	1dm2	1aq1	0.8

CDK2	1aq1	1dm2	0.8
COX-2	3pgh	1cx2	1.0
COX-2	1cx2	3pgh	1.0
Estrogen receptor	1err	3ert	1.0
Estrogen receptor	3ert	1err	1.4
Factor Xa	1ksn	1xja	1.5
Factor Xa	1xka	1ksn	1.5
HIV-RT^c	1rth	1c1c	1.3
HIV-RT	1c1c	1rth	2.5
Neuraminidase	1nsc	1a4q	0.8
Neuraminidase	1aq4	1nsc	1.7
PPAR_γ^d	1fm9	2prg	1.8
PPAR_γ	2prg	1fm9	3.0
Thermolysin	1kr6	1kjo	1.3
Thermolysin	1kjo	1kr6	3.2
Thymidine kinase	1kim	1ki4	0.4
Thymidine kinase	1ki4	1kim	1.2

a: CDK2: cyclin dependent kinase 2, **b:** COX-2: cyclooxygenase-2, **c:** HIV-RT: HIV reverse transcriptase, **d:** PPAR_γ: peroxisome proliferator-activated receptor- γ .

Induced-fit docking in Glide-Prime. A bound ligand can induce significant conformational changes in the geometry of the active site of a protein, however, it is often infeasible to determine the crystallographic structure of a complex¹³. The Glide-Prime software allows quick prediction of the geometry of an active site by exhaustively considering possible binding modes and induced conformational

changes which occur in the receptor active site as a result of binding by an inhibitor (Figure 3.1)¹³.

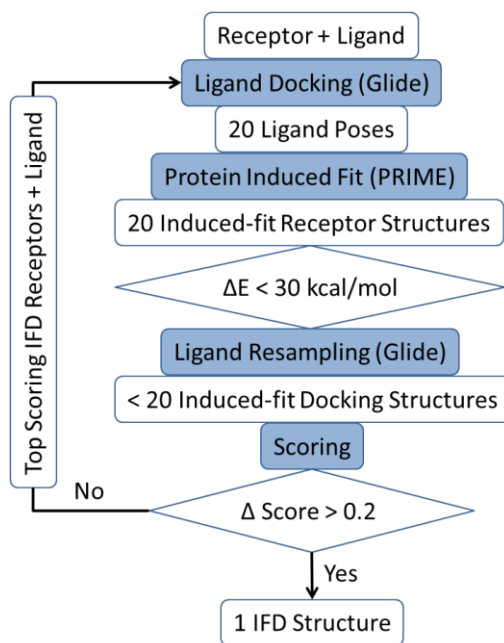


Figure 3.1. The induced-fit docking (IFD) protocol utilized by the Glide-Prime software¹².

In this induced fit docking (IFD) protocol, the ligand is first docked by Glide. Reduced van der Waals radii and increased Coulomb-vdW (Van der Waals) cutoffs are then used along with temporary removal of highly flexible side chains to produce an array of 20 divergent ligand poses during this initial docking step. In an effort to produce diverse poses, those with an RMSD of less than 0.5 Å and a maximum atomic displacement of less than 1.2 Å were considered to be redundant and therefore were eliminated. A Prime structure prediction is then used to reorient nearby side chains (those within 5 Å of any of the docked poses) to accommodate the ligand for each pose generated, with the lowest conformational energy. The total Prime energy, or molecular mechanics plus implicit solvation, was then used to rank

each protein structure. The five receptor orientations with the lowest energy scores were then docked with the ligand structures generated. Favorable binding interactions, defined as those which produced a change in free energy of < 30 kcal/mol, were then refined. Glide scores, based on the total energy of the ligand-receptor interactions, were then used to rank the complexes which resulted.

Contacts determined by Maestro. The Maestro software suite, which incorporates the Glide docking suite, defines and displays contacts and hydrogen bonds between a ligand and its receptor. Specifically, a hydrogen bond is defined by a total of four atoms: the hydrogen atom donor (H), the acceptor atom (A), the donor atom (D) bonded to H, and a neighboring atom (B) bonded to A; these result in the relationship: D-H...A-B. The maximum distance between the acceptor atom (A) and the donor hydrogen atom (H) is 2.5 Å, the angle between D-H...A must exceed the minimum donor angle of 120°, and the angle between H...A-B must be greater than the minimum acceptor angle of 90°. Contacts, however, are defined by the ratio given in **Equation 3.1**.

$$C = \frac{D_{1,2}}{(R_1+R_2)}$$

Equation 3.1. The ratio used to define contacts in Maestro; C: contact ratio; $D_{1,2}$: the distance between atoms 1 and 2, R_1 and R_2 : Van der Waals radii of atoms 1 and 2.

Based on **Equation 3.1**, contacts are classified as “good”, “bad”, or “ugly” by the ratio of the distance between the atoms versus the sum of their Van der Waals radii. The ratio of a good contact, where two atoms experience attractive forces (Van

der Waals or London dispersion forces), ranges from 1.30 to 0.89. The ratio of a bad contact, in which atoms may begin to experience repulsion due to overlap, falls between 0.89 and 0.75. And finally, an ugly contact ratio, in which two atoms experience significant repulsion as they attempt to occupy the same space, is less than 0.74. Because contacts only consider the overlap resulting from the outer portions of a charge distribution, they do not reflect electrostatic potential. Therefore, it is possible for a contact classified as bad to be favorable if the atoms possess opposing partial charges.

Enantioselective binding and inhibition. One reason for employing the stereoselective benzodiazepine synthesis discussed in Chapter 2 was for modeling purposes as well as for the detection of enantioselective binding. The latter represents an element commonly considered in molecular recognition since an enzyme may experience either equipotent or differential inhibition by enantiomers. A two-point binding model of recognition is believed to exist in cases of equipotent binding of enantiomers, where two chemical entities within each binding partner account for most of the associated binding energy¹⁷. If one enantiomer binds to the enzyme with ≥ 4 -fold higher affinity than that of the other enantiomer, however, enzyme-ligand interactions are said to be enantioselective¹⁸. For enantioselective binding to occur, a chiral atom must involve at least three of its four substituents in the recognition event. A multi-point attachment is described by two theories as requiring a chiral atom to involve at least three of its four substituents in the recognition event for enantioselective binding to occur¹⁹. In the three-point binding model, only one of the enantiomers is capable of the orientation necessary to interact

with three sites: A, B, and C (**Figure 3.2, a**). The three-dimensional binding surface is thus defined by three specific points so that only one enantiomer may contact each site optimally²⁰. Recently, it has been proposed that a fourth interaction may be necessary to distinguish between enantiomers (**Figure 3.2, b**)²¹. In this model, enantiomers may essentially bind to opposite sides of a binding surface²².

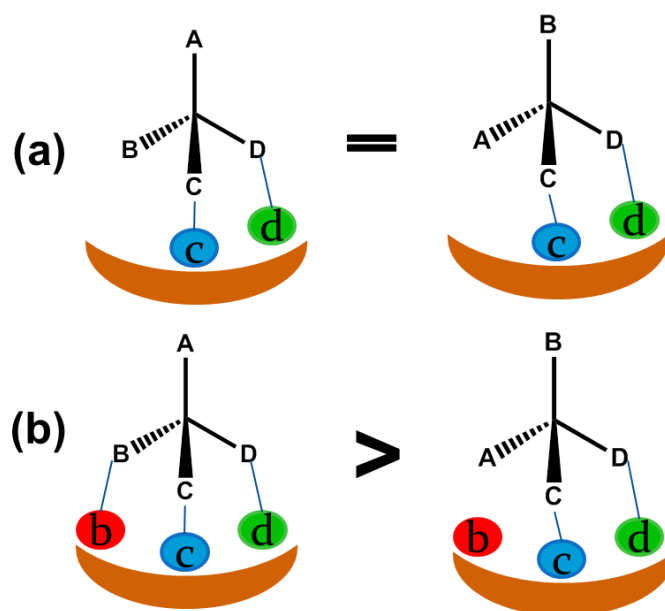


Figure 3.2. Three and four-point binding models. **(a)** Three-point interaction model. **(b)** Four-location model¹⁷.

These models have helped to explain the observed enantioselectivity of some enzymes. Many enzymes are capable of distinguishing between two enantiomers in the active site due to their composition by enantiopure substances²³. Enantioselectivity of the molecular target must therefore be considered when designing synthetic ligands for an enzyme. This issue is complex for several reasons. Firstly, there are examples of non-enantioselective enzymes, such as HIV-1 reverse transcriptase and thymidine kinases^{23,24}. Also, there are two mechanisms

which may describe molecular recognition: lock-and-key and induced fit. While the former assumes complementarity of enzyme and substrate, even when unbound, the latter proposes conformational changes of both enzyme and substrate which are mutually induced^{25,26}. The multiple mechanisms of recognition present a significant challenge when attempting to describe the precise structural features important for binding. Lastly, it is possible for optically active ligands to racemize *in vivo*, and the resulting enantiomers may give dissimilar results²⁷.

There are various possible effects when using racemic ligand mixtures *in vivo*. In some instances, potency may be decreased two-fold by the presence of the inert enantiomer of the optimal ligand. This is known as the “inert effect,” and many literature examples of it exist, including ibuprofen, methadone, morphine, and warfarin²⁷. In some cases, however, one enantiomer may actually be toxic²⁸. The most notorious example of significant toxicity resulting from a single enantiomer of a drug is the severe birth defects which were observed among women prescribed Thalidomide, due to the (+)-enantiomer^{27,29}.

RESULTS AND DISCUSSION

Molecular modeling protocol validation. The validation protocol described here mimics that followed in previous modeling work by Dr. Francis and Dr. Ung in the design of the **BZD** analogues, to ensure concurrent results¹⁶. Before predicting the binding mode of **BZD-29** to ROCKI and ROCKII, it was first necessary to validate Glide-Prime's ability to simulate the binding of these targets to a known ligand. Here, Glide-Prime was used to dock Fasudil back into the active sites of ROCKI (PDB= 2ESM) and ROCKII (PDB= 2F2U) after extraction^{1,41}. The five poses of the ligand with the lowest energy generated by the software were then compared to the structures of the crystallized ligand and to the complexes through calculations of RMSD values determined by comparing the relative distances between pairs of related heavy atoms (C, N, O)⁴⁶. In the Fasudil-ROCKI crystal structure (determined at 3.2 Å resolution), the isoquinoline ring occupies the same space as the adenine of ATP¹. The isoquinoline nitrogen accepts a hydrogen bond from the amide nitrogen of Met156, while the protonated homopiperazine amine donates a proton to the side chain of Asp160. Glide-Prime predicted the Fasudil/ROCKI complex with RMSD values of ≤ 1.71 Å (**Figure 3.3, Table 3.2**).

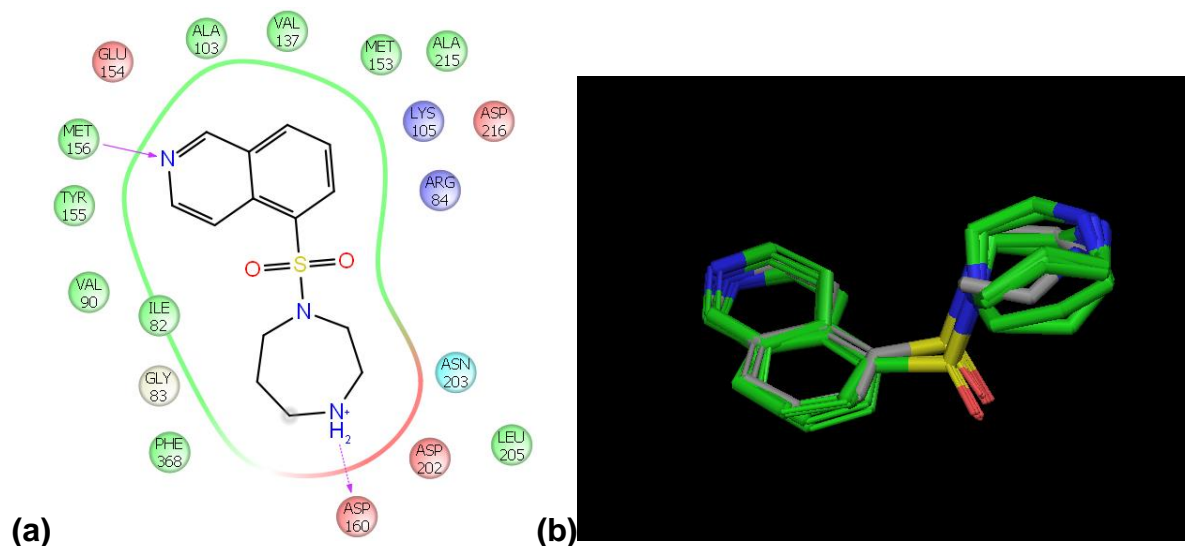


Figure 3.3. (a) A two-dimensional ligand interaction diagram of Fasudil binding to ROCK1. (b) The crystallized pose of Fasudil (grey) binding to ROCK1 superimposed on the Glide-Prime predicted poses (green). Yellow atoms indicate sulfur, red atoms indicate oxygen, and blue atoms indicate nitrogen. (PDB ID: 2ESM)¹

Table 3.2. The RMSD values for Fasudil crystallized in the ROCK1 complex versus the predicted pose of Fasudil in the ROCK1 complex. The relative distance between pairs of related heavy atoms in the crystallized and predicted poses are used to calculate the RMSD values.

Rank	Fasudil	Fasudil:ROCK1
1	0.9317	1.6224
2	0.9893	1.6181
3	1.371	1.6983
4	0.838	1.7072
5	1.5610	1.7130

The ROCKII-Fasudil crystal structure was determined at 2.4 Å resolution with a construct consisting of an N-terminal 67 residue extension (residues 18-84) and a kinase domain with a C-terminal extension (residues 85-417)⁴⁷. Two

crystallographically independent complexes are contained within the structure (**Figure 3.4 a and b, Figure 3.5 a and b**) with an RMSD of 0.65 Å between the two poses^{2,47}. Fasudil was docked into ROCKII to determine if both poses are accurately predicted by Glide-Prime. Fasudil occupies the ATP binding sites of both molecules of ROCKII and in both poses the isoquinoline ring resides in the adenine-binding pocket. In pose A of the complex, the homopiperazine ring forms polar interactions with the side chains of Asn219 and Asp232. In pose B, the homopiperazine ring shifts as a result of two bond rotations on the central sulfur atom of the sulfonyl group. Due to this conformational change, the amine of the homopiperazine ring is able to hydrogen bond with the side chain of Asp176 and the main chain of Asp218. In contrast to the interaction of Fasudil and ROCKII in pose A, the interaction of the phosphate binding loop (or P-loop) of pose B and Fasudil results from induced-fit, where the P-loop of pose B folds down to increase surface complementarity with the inhibitor^{2,47}. Specifically, the aromatic ring of Phe103 flips inside the loop to form a series of hydrophobic contacts with the homopiperazine ring (**Figure 3.5, b**)². This demonstrates a plasticity of the ROCK phosphate binding loop which is unseen in similar complexes of related enzymes and which has been proposed to account for the specificity of Fasudil for the ROCK kinases⁴⁷.

The Glide-Prime software was evaluated as to its ability to accurately predict these Fasudil-ROCKII complexes. The software successfully generated two distinct poses, analogous to poses A and B. The RMSD values for the top five Glide-Prime predicted poses for Fasudil binding to ROCKII compared to the crystallized poses were between 0.724-1.976 Å, while the range of RMSD values for the top five complex predictions was 0.611-1.725 Å (**Table 3.3**). Combined, these data validate the accuracy of Glide-Prime predictions of the Fasudil-ROCKI and -ROCKII complexes with low RMSD values.

Table 3.3. RMSD values for the top five Glide-Prime predicted poses for Fasudil binding to ROCKII compared to the crystallized poses. RMSD values are based on the relative distance between pairs of related heavy atoms in the predicted and crystallized poses and are calculated as previously described.

ROCKII (Pose A)			ROCKII (Pose B)		
Rank	Fasudil	Fasudil:ROCKII(A)	Rank	Fasudil	Fasudil:ROCKII(B)
1	0.724	0.611	1	0.725	1.599
2	0.756	0.620	2	1.221	1.698
3	0.801	0.626	3	1.470	1.700
4	0.898	0.618	4	1.531	1.725
5	0.951	0.665	5	1.976	1.722

Modeling the interaction of **BZD-29** with ROCKI and ROCKII. In the manner outlined in the introduction of this chapter and in **Figure 3.1** for the induced fit docking protocol, **BZD-29** was docked into the binding sites of both ROCKI (PDB ID: 2ESM) and ROCKII (PDB ID: 2F2U) (**Figure 3.6** and **3.7**)^{1,47}. As seen in Chapter 2,

initial inhibition data for **BZD-29** showed both enantiomers to be essentially equipotent for the ROCK isoforms. Additionally, their predicted contacts with the binding sites appear to be similar. Specifically, in ROCKI the pyridine ring of **(S)-BZD-29** accepts a hydrogen bond from the main chain amine of Met156 while N4 of the benzodiazepine ring donates a hydrogen bond to the side chain of Asp216 and the benzyl ring participates in a cation-pi stacking interaction with Lys200. In ROCKII, the pyridine of **(S)-BZD-29** also accepts a hydrogen bond from an analogous residue (Met172) N4 donates a long range hydrogen bond to the side chain of Asn219 while the benzyl ring participates in pi-cation stacking with Lys121. These interactions are mimicked by **(R)-BZD-29** except that in ROCKI, no pi-cation stacking is predicted, and in ROCKII, there is no prediction of an interaction between N4 and Asn219.

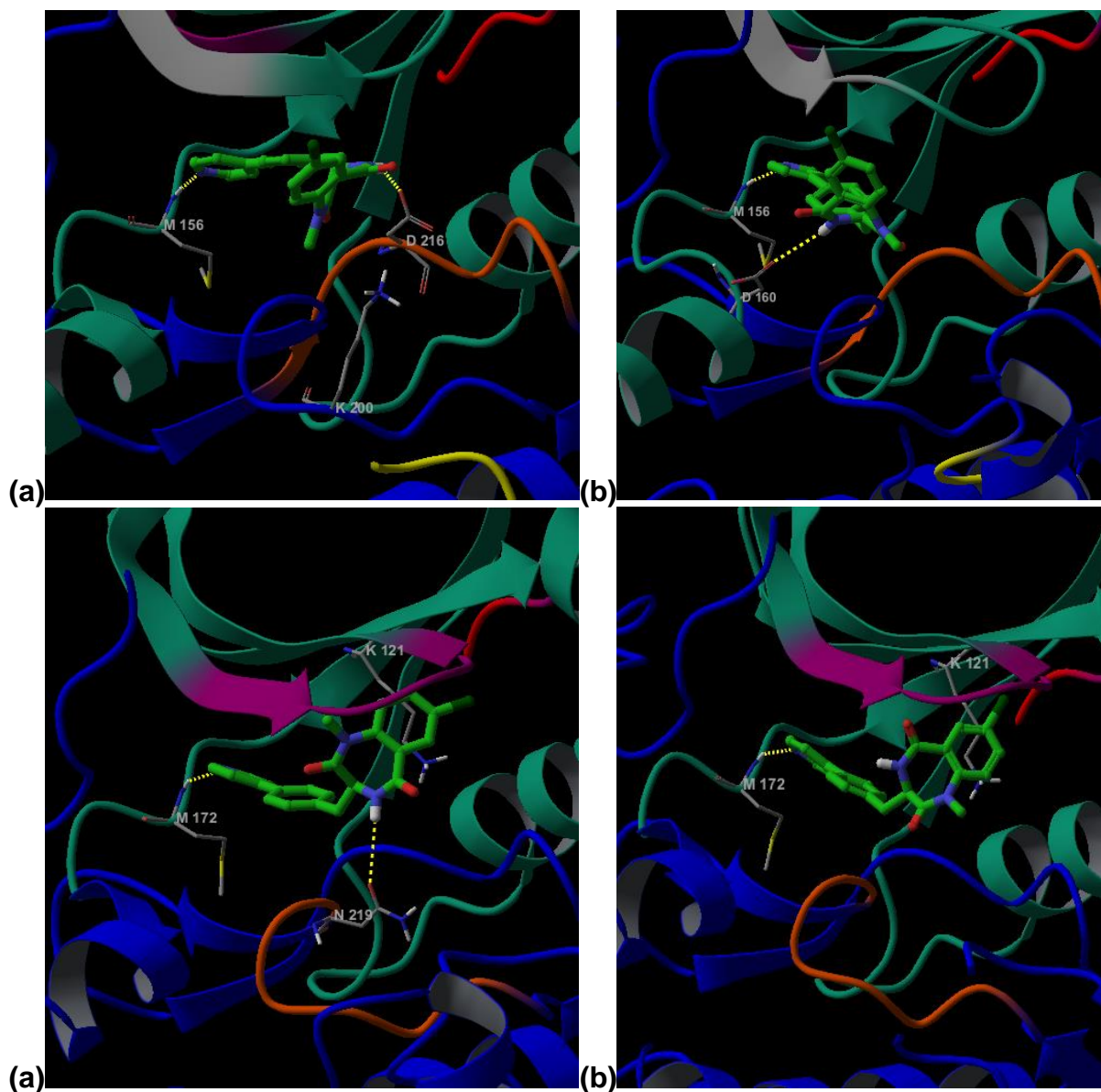


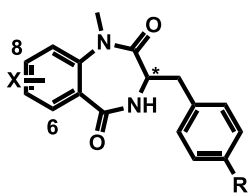
Figure 3.7. Predicted binding poses of **BZD-29** in ROCKI and ROCKII. **(a)** **(S)-BZD-29** in ROCKI. **(b)** **(R)-BZD-29** in ROCKI. **(c)** **(S)-BZD-29** in ROCKII. **(d)** **(R)-BZD-29** in ROCKII. Protein domain coloring: red= carboxy-terminal extension, teal= amino-terminal lobe, blue= carboxy-terminal lobe, purple= P-loop, yellow= A-loop, orange= C-loop.

Computational models and workflows. **Table 3.4** shows a selection of analogs of **BZD-29** which produced remarkable assay results and which were thus modeled in the binding sites of ROCKI and ROCKII in an attempt to rationalize their activities. In

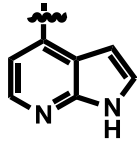
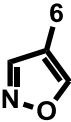
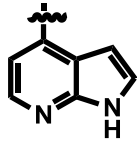
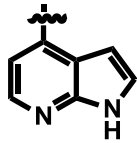
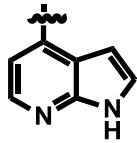
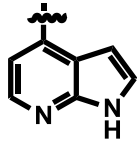
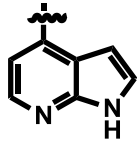
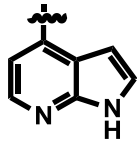
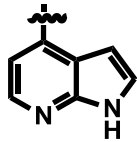
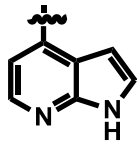
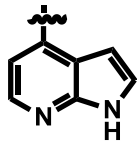
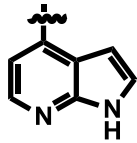
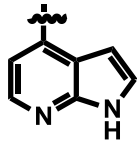
defining binding modes and critical interactions, an energetically significant hydrogen bond was inferred when a probable donor and acceptor were within 3.5 Å of each other⁴⁵. However, any hydrogen bond greater than 3.2 Å was categorized as long-distance and thus weak and predominantly electrostatic in nature⁴⁶.

Because substitution of the C ring was relatively facile and extensive literature sources exist for guidance in optimizing contact with the hinge region, this optimization was accomplished through the production of a series of modified analogues. In contrast, the tedious nature of A ring modification and the lack of relevant literature without knowledge of inhibitor orientation made the design of this region more amenable to predictive structure activity relationship (SAR) models and computational methods. With regards to the latter, two general workflows were employed. One protocol attempted to mimic the contacts reported to impart potency or selectivity to known ROCK inhibitors (Computational Workflow A) while another used fragments which made favorable contacts with the active site in the design of substituents to be included onto the template of **BZD-29** (Computational Workflow B).

Table 3.4. Inhibition results for **BZD-29** analogs with varied A and C rings.



Compound	R	X	ROCKI rel. ^a	ROCKII rel.	R2 Select. ^b	R2 E.S. ^c
<i>rac</i> -29 ^d		7-Cl	1.0x	1.0x	1.0	N/A
(<i>S</i>)-7 ^e		7-Cl	7.6x	5.6x	0.7	1.0
(<i>R</i>)-7 ^f			13.0x	5.6x	0.4	
(<i>S</i>)-11		7-Cl	14.0x	16.6x	1.2	2.2
(<i>R</i>)-11			27.9x	36.9x	1.3	
(<i>S</i>)-13		7-Cl	0.1x	0.1x	1.0	1.0
(<i>R</i>)-13			0.1x	0.1x	1.0	
(<i>S</i>)-19			3.9x	4.1x	1.1	2.1
(<i>R</i>)-19			1.9x	1.9x	1.0	

(S)-21			168.7x	110.0x	0.7	36.3
(R)-21			3.6x	3.0x	0.8	
(S)-22		7-OH	31.1x	63.2x	2.0	13.1
(R)-22			2.0x	4.8x	2.4	
(S)-25		H	43.7x	36.5x	0.8	1.3
(R)-25			51.0x	48.5x	1.0	
(S)-26		9-OMe	31.1x	32.1x	1.0	2.9
(R)-26			8.3x	11.2x	1.4	
(S)-29		9-Br	94.7x	69.3x	0.7	4.6
(R)-29			20.5x	15.0x	0.7	
(S)-30		9-F	195.2x	109.2x	0.6	5.6
(R)-30			27.9x	19.6x	0.7	

a: rel. IC₅₀= IC₅₀ relative to *rac*-BZD-29 (ROCKI= 3093.5 nm +/- 139.3, ROCKII= 3075.0 nm +/- 881.1), **b:** Selectivity for ROCKII (=ROCKI IC₅₀/ ROCKII IC₅₀), **c:** R2 E.S.= enantioselectivity of ROCKII, **d:** *rac*= racemate, **e:** (S)= >95% S-enantiomer, **f:** (R)= >95% R-enantiomer.

In Computational Workflow A, potent and/or selective inhibitors reported in literature were docked into the ROCKI and ROCKII binding sites with the induced-fit docking protocol previously described. Then poses of **BZD-29** docked into the same binding sites were superimposed onto the poses of the known inhibitors using the protein structure alignment function of Maestro. Next, components were manually affixed to the lead which mimicked those of the known inhibitors until contacts were made with the residues purported to be critical to the potency or selectivity of the known inhibitors. Then a virtual series of analogs with various substituents known to be synthetically accessible and believed to be capable of making these contacts was created. This virtual series was then docked to ROCKI and/or ROCKII and those compounds which successfully made the desired contacts were synthesized and assayed.

In Computational Workflow B, a pseudo-fragment based approach was utilized in which a fragment library, provided by Glide, was screened for favorable interactions with the local region of the ATP binding site occupied by the A ring of **BZD-29**. The most successful fragments were overlaid with the lead compound in the active site to predict their optimal orientations. Next, a virtual analog series incorporating these moieties, or electronically similar substitutions more amenable to stable compounds and/or facile synthesis, was created and then virtually screened in the same manner as in Computational Workflow A. The most successful virtual compounds were then produced and assayed in order of their synthetic accessibility.

As referenced in Chapter 2, a drawback of these types of computational design methods is the production of physicochemically unrelated analogs (such as **21** and **22**),

due to the incorporation of such highly specialized motifs for the establishment of specific contacts with the target. However, the combination of this approach with the traditional SAR techniques outlined in Chapter 2 allowed the data resulting from analogues to be analyzed with regards to their predicted contacts as well as to their effects on the general electronic or steric environment of the active site.

Rationalizing observed effects on potency and enantioselectivity. Firstly, the similar inhibition levels of the indazole-based inhibitors ((**S**)-**7** and (**R**)-**7**) to those of (**S**)-**BZD-29** and (**R**)-**BZD-29** suggest similar binding profiles. However, it does appear that the R-enantiomer of the indazole ((**R**)-**BZD-7**) inhibitor may bind more efficiently than did the R-enantiomer of the pyridine inhibitor ((**R**)-**BZD-29**). The results of modeling the indazole inhibitors (**Figure 3.8** and **3.9**) seem to explain this data. Due to the lack of ROCK isoform selectivity and the redundancy of the ROCK binding pockets, and in an effort to be concise, only the results of non-redundant docking poses for ROCKII are shown. As is evident from the resultant complexes, although the long range interactions associated with N4 of **BZD-29** are no longer predicted, interactions with the hinge region have increased to include a hydrogen donation to the main chain carbonyl of Glu170. This prediction is substantiated by extensive literature documentation of this type of bi-dentate bond formation for indazole-based kinase inhibitors⁴⁸. Next, the pi-cation stacking interaction with Lys121 seems to have shifted from the A ring of the inhibitor, seen for **BZD-29**, to the B ring of analog **7**. Additionally, (**S**)-**7** is makes contact with the side chain of Lys121 by accepting a hydrogen bond with a carbonyl of the benzodiazepine ring; however, this additional interaction is not suggested by the inhibition data since there is no significant difference between enantiomers.

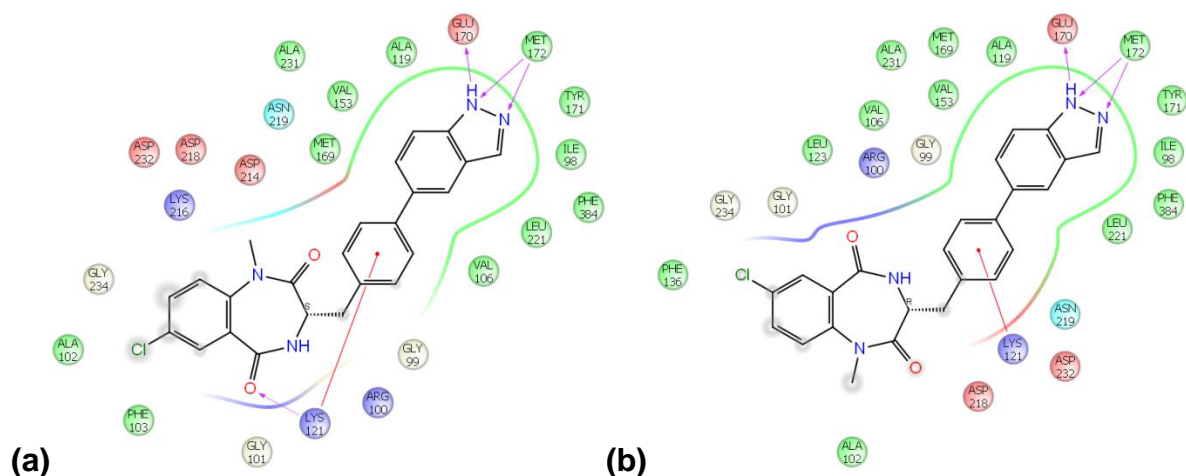


Figure 3.8. Two-dimensional ligand interaction diagrams of (a) **(S)-7** and (b) **(R)-7** in ROCKII.

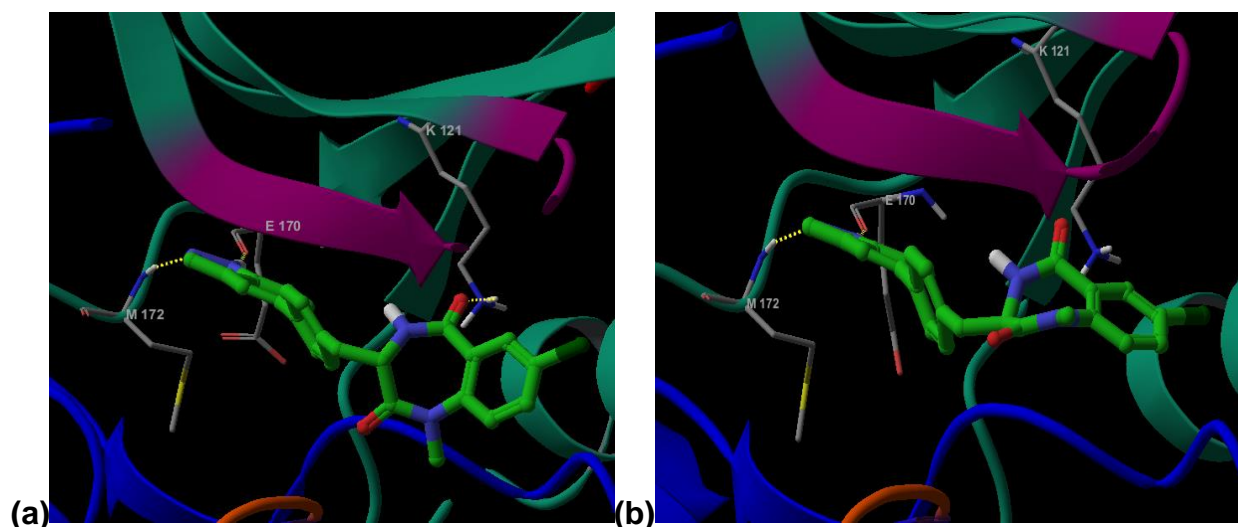


Figure 3.9. Predicted binding poses of (a) **(S)-7** and (b) **(R)-7** in ROCKII.

Next, the inhibition data for the azaindole-based analogs (**(S)-11** and **(R)-11**) showed them to be significantly more potent (up to 15x) compared to the pyridine-based inhibitors (**(S)-BZD-29** and **(R)-BZD-29**). As the docking results in **Figures 3.10** and **3.11** show, this may be due to the maintenance of the Lys121 pi-cation stacking interaction and the Met172 hydrogen bond acceptance with the addition of hydrogen

bond donations to Glu170 and Tyr171. Due to its potency and lack of reported cytochrome P inhibition concerns, azaindole was chosen as the optimal heterocycle for the C ring.

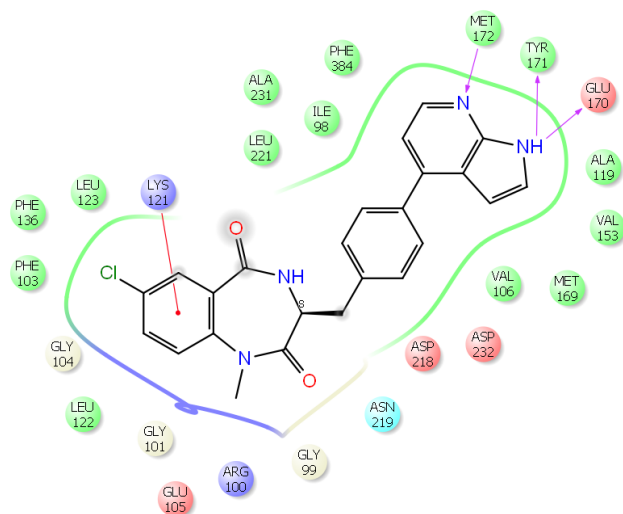


Figure 3.10. Two-dimensional ligand interaction diagram of **(S)-11** in ROCKII.

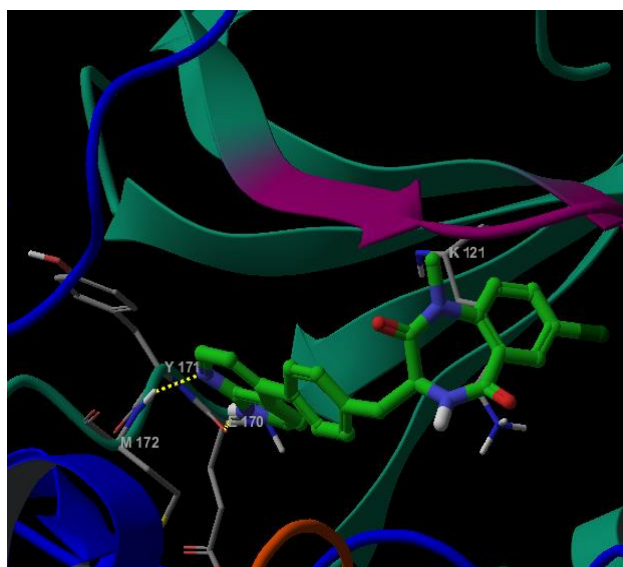


Figure 3.11. Predicted binding pose of **(S)-11** in ROCKII.

It was considered that one factor which might hinder the development of enantioselective binding for analogs based on the benzodiazepine scaffold was the restriction of two of the four substituents of the chiral atom (C3), by the rigidity of the benzodiazepine ring (**Figure 3.12**). By eliminating this constraint and allowing the chiral center substituents to reorient freely, it seemed conceivable that they might be better able to adopt the optimal orientations necessary to achieve specific interactions with the target. The simplest route to such an inhibitor involved the modification of a synthetic intermediate of a previously prepared analog, **11** (**Scheme 3.1**). This synthesis required coupling of L- or D-phenylalanine (to render the *S*- or *R*-enantiomer of the final product, respectively) with N-methyl isatoic anhydride in pyridine. Instead of cyclizing the resultant product in acetic acid, as shown in **Scheme 2.1**, the synthetic intermediate was methylated to more closely mimic the electronic state of the benzodiazepine-based analogs. The Suzuki coupling then proceeded in the same manner as previously described to produce analog **31**.

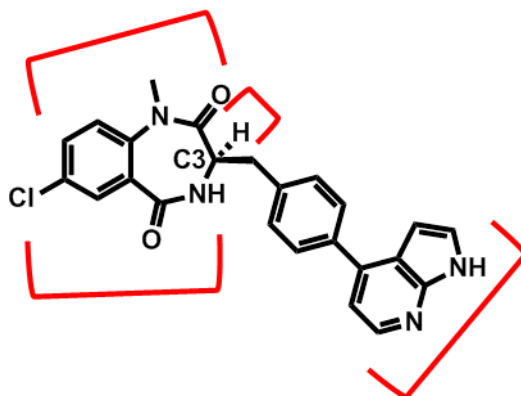
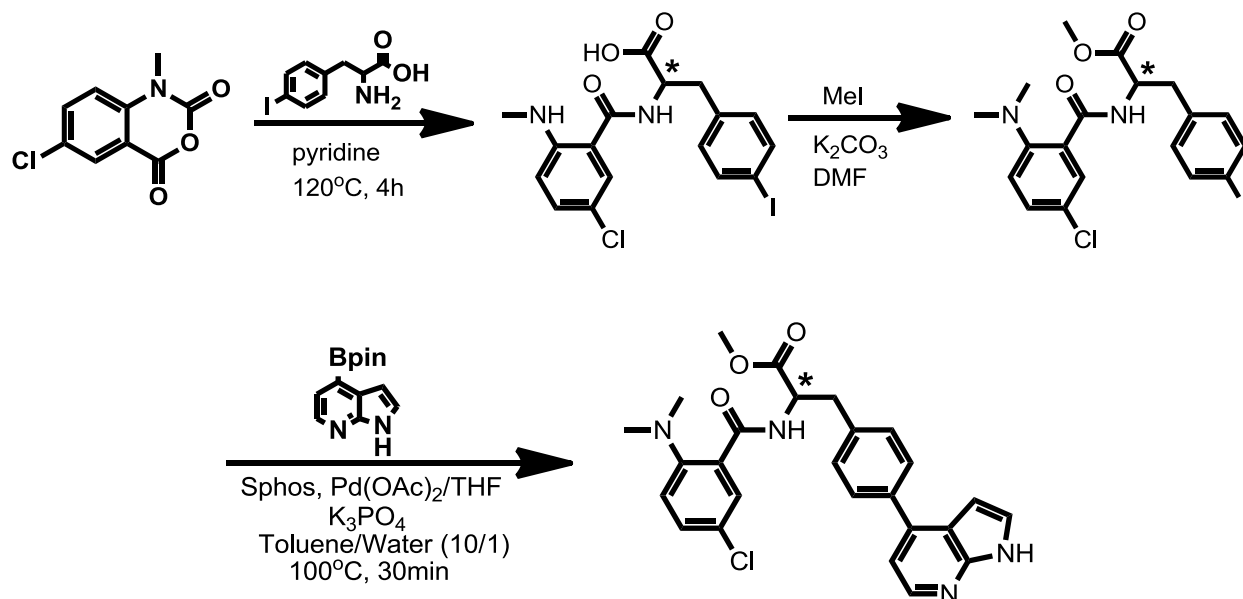


Figure 3.12. The structure of **11** with the chiral center displayed and its four substituents highlighted.



Scheme 3.1. Synthesis of **31**.

Although analog **31** was less potent than **11**, it did successfully develop a significant degree of enantioselectivity (**Table 3.5**). This indicated that introducing rotational flexibility to these inhibitors by elimination of the benzodiazepine ring might be one route to improving selectivity of future analogs by increasing the number of specific contacts between the inhibitors and the target.

Table 3.5. Comparison of the inhibition profiles of **11** and **31**.

Compound	ROCKI rel. ^a	ROCKII rel.	R2 E.S. ^b
(<i>S</i>)- 11 ^c	14.0x	16.6x	2.22
(<i>R</i>)- 11 ^d	27.9x	36.9x	
(<i>S</i>)- 31	4.8x	8.2x	4.8
(<i>R</i>)- 31	0.9x	1.7x	

a: rel. $IC_{50} = IC_{50}$ relative to *rac*-**BZD-29** (ROCKI= 3093.5 nm +/- 139.3, ROCKII= 3075.0 nm +/- 881.1), **b:** R2 E.S.= enantioselectivity of ROCKII, **c:** (*S*)= >95% *S*-enantiomer, **d:** (*R*)= >95% *R*-enantiomer.

Although, as mentioned in Chapter 1, the gatekeeper of ROCK which occludes the back hydrophobic pocket of the ATP binding cleft, is a large, hydrophobic methionine residue (Met169 in ROCKII), a small, hydrophobic substituent (methyl) was introduced on the azaindole ring to determine the size restrictions this imposed ((**S**)- and (**R**)-13) (**Figure 3.12**). The ability of an inhibitor to bind in this pocket often grants enhanced potency as well as improvements to selectivity due to a lesser degree of conservation of this region relative to the ATP binding site, thus any interaction with this region is highly desirable. Unfortunately, these analogs were inactive and Glide even failed to successfully produce a docking pose for either of these inhibitors. This indicates a severe restriction at this location.

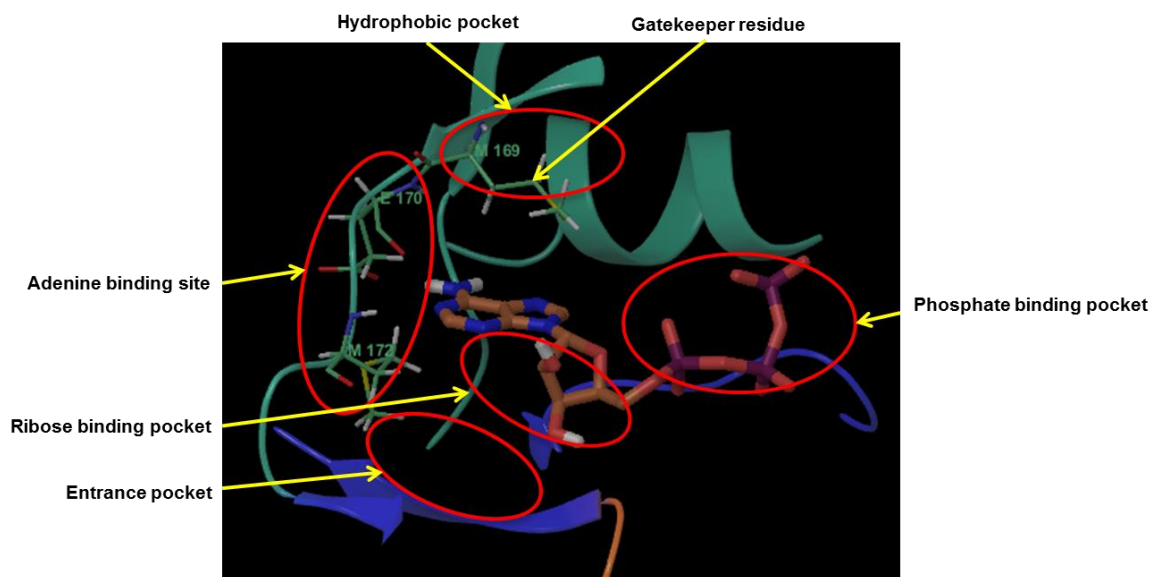


Figure 3.13. The putative regions of the ATP binding site with the location of the gatekeeper residue highlighted.

To visualize this effect, the binding poses of (**S**)- and (**R**)-11 were modified manually to include this methyl group at C3 of the azaindole ring. In doing this, it was observed, as is shown in **Figures 3.14** and **3.15**, that the methyl group came into close

contact with the side chain of the gatekeeper residue, Met169. Glide classified this steric clash as an “ugly” contact to describe the violation of the atoms’ Van der Waals radii as they attempted to occupy the same space. Because Met169 lies in the hinge region proximal to the residues necessary for azaindole binding and inhibition (Met172, Tyr171, and Glu170) it seems possible that repulsion between the Met169 side chain and this methyl group does not allow the azaindole ring to adopt the orientation necessary to make these critical contacts.

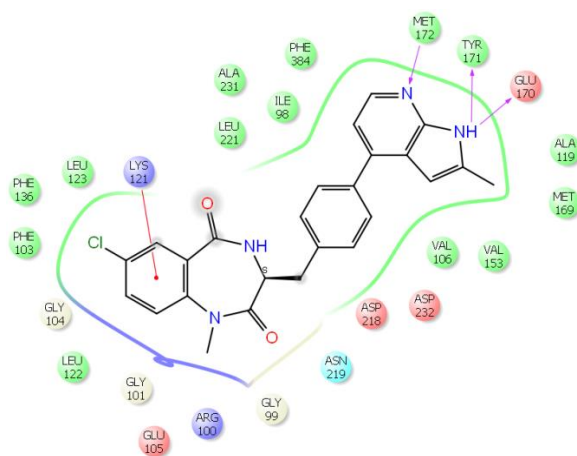


Figure 3.14. Two-dimensional ligand interaction diagrams of **(S)-13** in ROCKII.

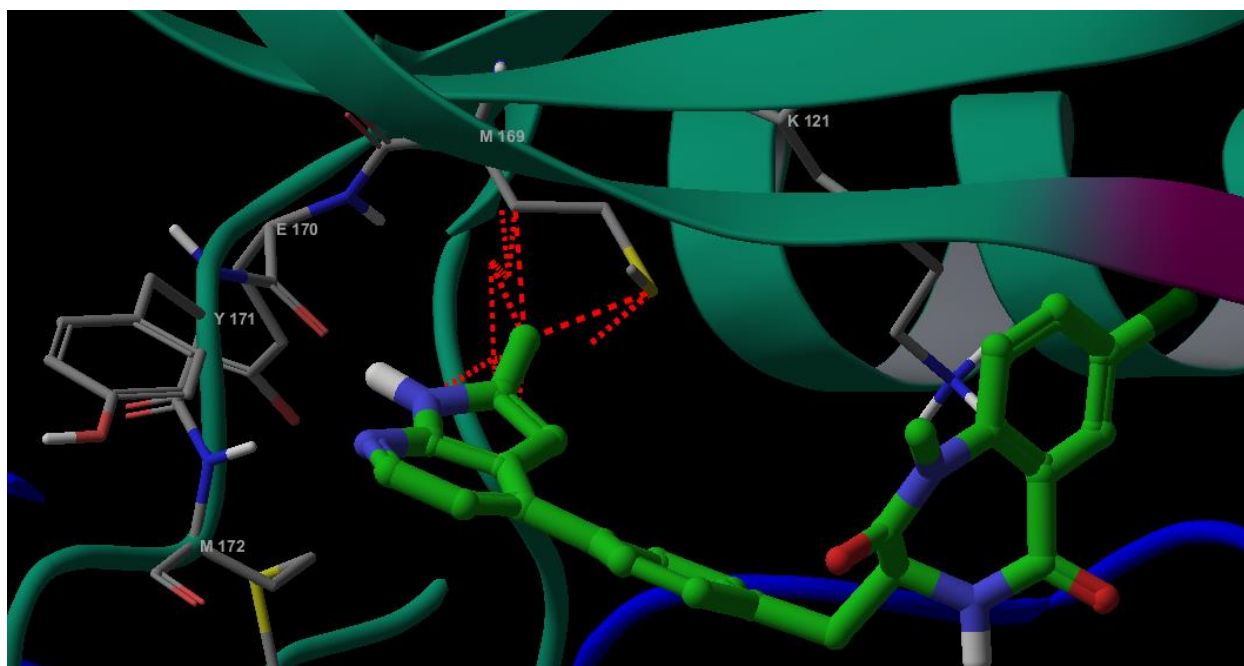


Figure 3.15. Manually amended binding pose of entry **(S)-11** showing “ugly” contacts between C3 methyl and the Met gatekeeper residue as red hashes.

Next, the A ring was modified to probe the possible interactions between the inhibitor and the target which might be achieved at this location. Due to the lack of a common intermediate for most analogs with A ring modifications, their synthesis was somewhat more tedious than that of the altered C ring analogs. Therefore it was desirable to utilize methods, such as the manual Hansch analysis described in Chapter 2 or computational methods to guide analog design and reduce the number of compounds necessary to gain useful information about this region of the binding pocket.

The first examples of successes resulting from Computational Workflow A were the hydroxyl analogs, entries **(S)-** and **(R)-22**. Here, Glide predicted a hydrogen bond should form between Lys121 and the A8-hydroxyl substituent, mimicking the hydrogen bond between the same residue and the amide carbonyl of the known inhibitor SR3677 (**Figure 3.16**). Both the computational models and the inhibition data suggest this

contact does occur (**Figures 3.17** and **3.18**). Aside from the improvement in potency seen for the *S*-enantiomer (**(S)-22**) a significant enantioselectivity emerges where the *S*-enantiomer is 13x more potent versus the *R*-enantiomer. This aspect suggests a multi-point attachment model to describe the optimal binding orientation of the *S*-enantiomer. In fact, in the model, the *S*-enantiomer appears to accept hydrogen bonds from the side chain of Lys121 by the hydroxyl oxygen and from the side chain of Lys216 by a carbonyl oxygen of the benzodiazepine ring, while donating a long-distance hydrogen bond to Asn 219 and maintaining the same contacts previously seen with Met172 and Glu170. Although the contact formerly predicted with Tyr171 by **11** is not seen in the prediction for **(S)-22**, this loss may be compensated for by the newly established contacts.

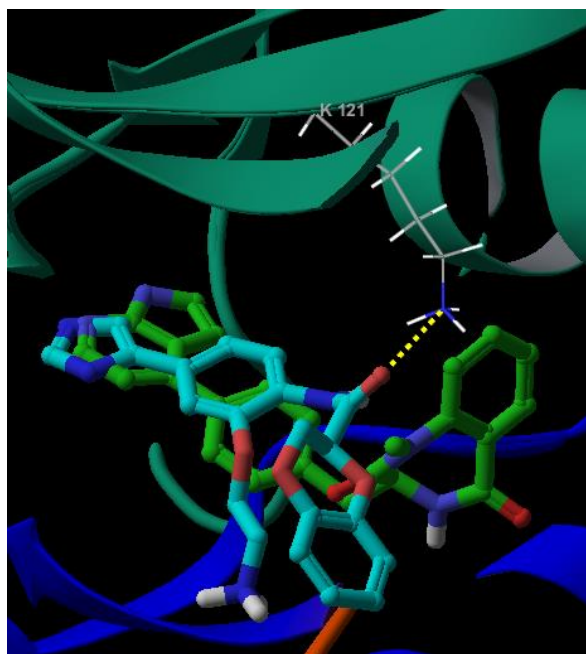


Figure 3.16. Overlay of the azaindole-based inhibitor, **11** (green) and SR3677 (blue) in the ROCKII active site with Lys121 displayed. The hydrogen bond formed between the carbonyl of SR3677 and Lys121 is shown by yellow hashes. This contact was successfully mimicked by the addition of a hydroxyl substituent on the A ring, leading to entries **(S)-** and **(R)-22**.

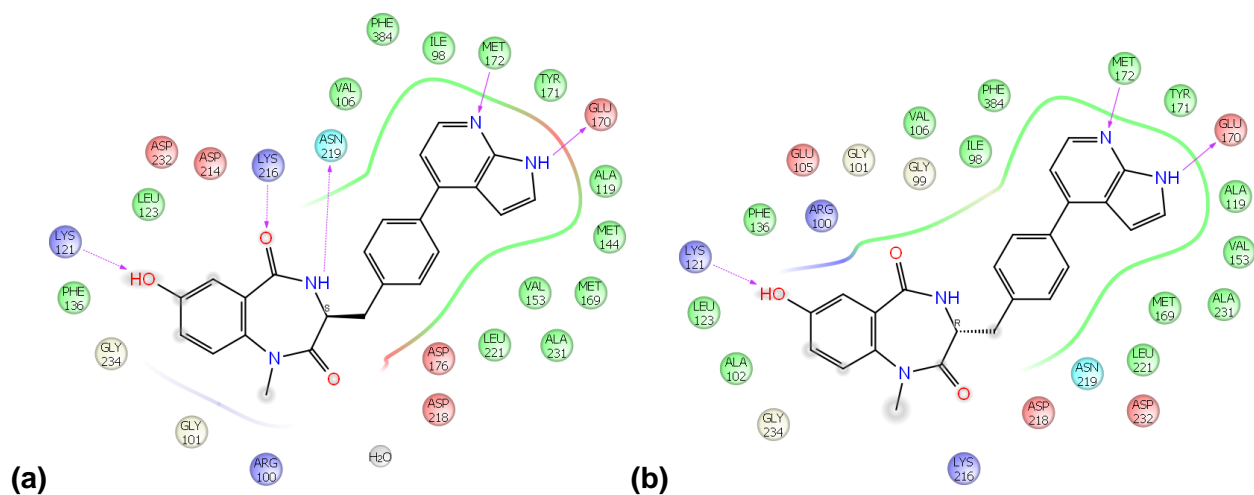


Figure 3.17. Two-dimensional ligand interaction diagrams of entries (a) (**S**)-22 and (b) (**R**)-22 in ROCKII.

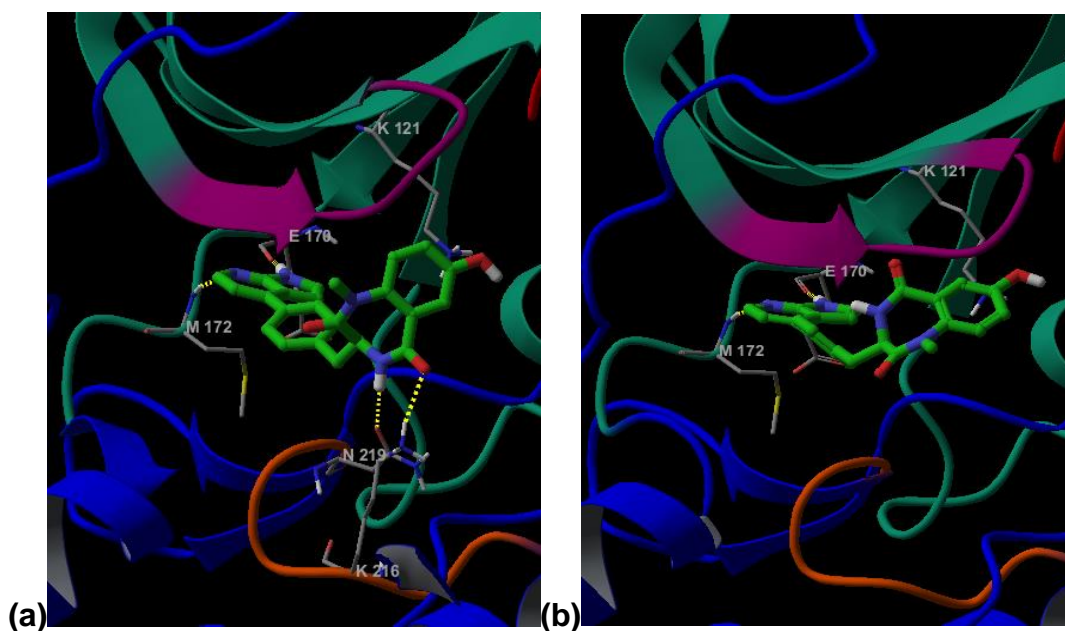


Figure 3.18. Predicted binding poses of (a) (**S**)-22 and (b) (**R**)-22 in ROCKII.

In an attempt to contact Lys216 due to its purported importance to the isozyme selectivity of one of the two known selective inhibitors to date, SLx-2119, the isoxazole-substituted analogs (**(S)**- and **(R)**-21) were designed with the same alignment protocol described previously for Computational Workflow A. Although it did not exhibit isoform selectivity, the *S*-enantiomer (**(S)**-21) represents the most potent inhibitor to date and, in

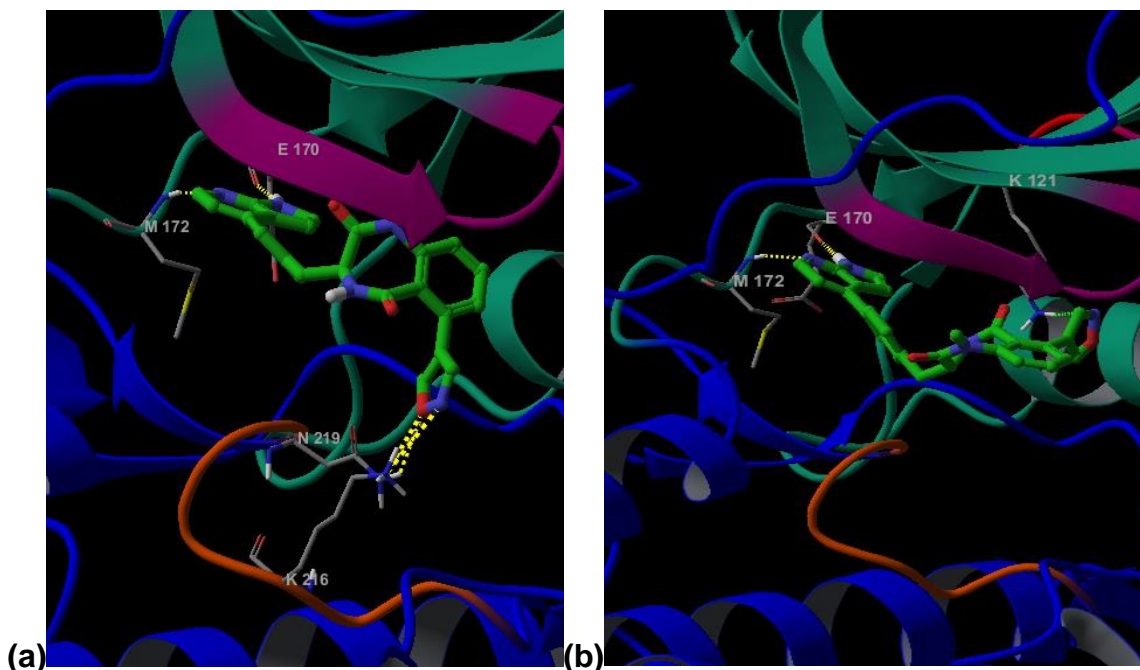


Figure 3.20. Predicted binding poses of (a) **(S)-21** and (b) **(R)-21** in ROCKII.

Next, fragment docking in the ATP binding pocket of ROCKII by Computational Workflow B highlighted possibilities of hydrogen bond formation with the backbone amine of Val106 or with the backbone carbonyl of Glu105. However, the docking poses of **BZD-29** and analog **11** showed limited space existed at this position, and the manual addition of even moderately sized substituents caused the benzodiazepine ring to reorient so that these contacts were not made. A series of analogs were produced in an attempt to make this contact while determining the extent of size restriction at this location. Of these, the 9-FI (**30**) was the optimal substituent, and was predicted to form a halogen bond with the carbonyl of Glu105, in addition to other favorable interactions, without causing reorientation of the benzodiazepine ring (**Figure 3.21, a**). Although 9-Br (**29**) should make a stronger halogen bond with this residue, the increased size led to the emergence of “ugly” contacts which presumably resulted in a less favorable

interaction (**Figure 3.21, b**). Although the (**S**)-**29** analog did improve ROCKII inhibition by approximately 69x times compared to that of **BZD-29**, the 9-FI analog ((**S**)-**30**) experienced an increase in ROCKII inhibition of 109-fold. Both compounds **29** and **30** also experienced significant enantioselectivity, 4.6x for **29** and 5.6x for **30**, supporting the prediction of this new contact.

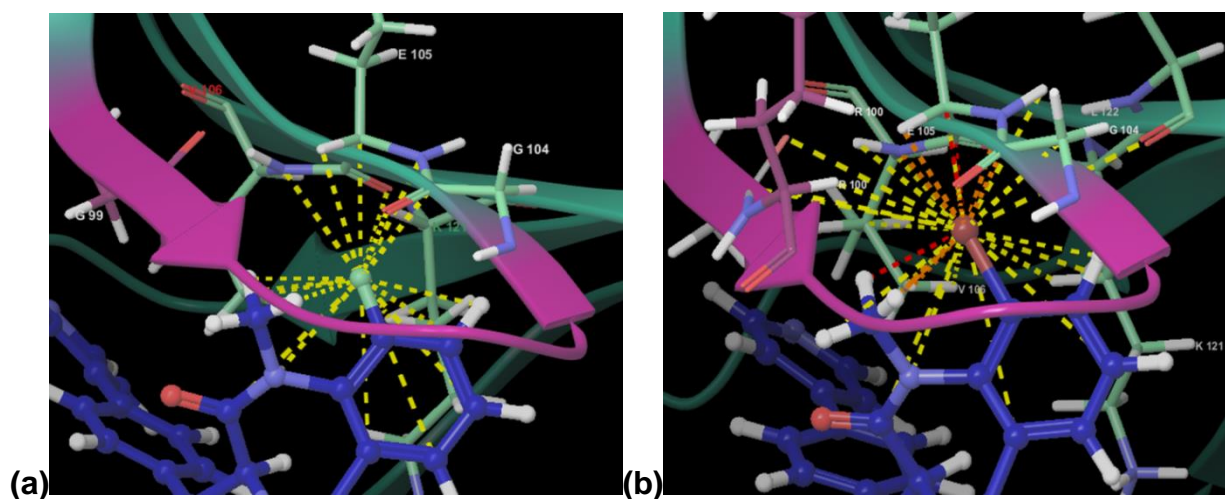


Figure 3.21. The good (yellow hashes), bad (orange hashes), and ugly (red hashes) contacts between fluorine (a) and bromine (b) at position 9 of the A ring and the ROCKII active site.

Enantioselective binding versus benzodiazepine-ring conformations. From the analog data shown in **Table 3.4**, it was observed that in each instance of significant enantioselectivity (**21**, **22**, **29**, and **30**), the *S*-enantiomer was more potent. It has been observed that 1,4-benzodiazepine-2,4-diones substituted at C3 tend to prefer a chair-like pose (known as the *M* configuration) as *S*-enantiomers but a boat-like pose (known as the *P* configuration) is the predominant configuration of *R*-enantiomers (**Figures 3.22** and **3.23**)⁴⁹. As shown, these configurations are preferred due to their placement of the C3 R group in a pseudo-equatorial orientation, the lower energy conformation compared

to a pseudo-axial orientation of the R group. These preferences increase greatly when substitutions at position 7 of the benzene ring increase in size due to the steric clash between this group and the R group of C3 in the pseudo-axial orientation⁴⁹.

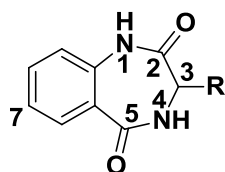


Figure 3.22. Number scheme of 1,4-benzodiazepine-2,4-dione template.

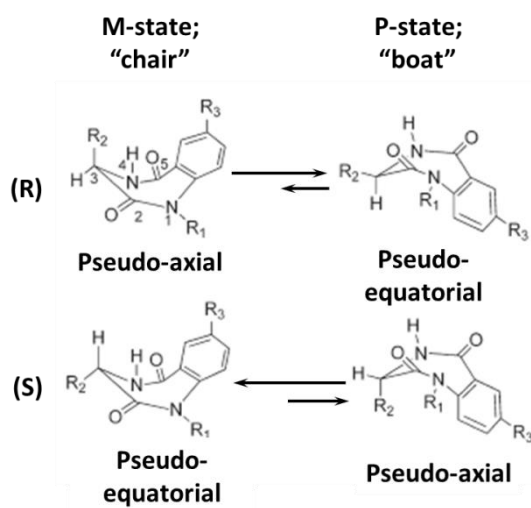


Figure 3.23. The conformational equilibria of the (3*R*)- and (3*S*)-1,4-benzodiazepine-2,5-dione nucleus.

It was considered then that the preference of the ROCKII ATP binding site for the *S*-enantiomer of the analogs may have simply reflected a preference for the chair-like, *M*-conformation of the benzodiazepine scaffold which is more readily adopted by the (*S*) enantiomer due to the large substituent at C3. due to general complementarity between this configuration and contours of the binding pocket. If this were indeed the case, then one would expect to observe a strong correlation between the size of the substituent at

A7 and the enantioselectivity of ROCKII for the inhibitor; as the size of the substituent increases, the degree of enantioselectivity should increase concurrently as the M-configuration is increasingly favored by the inhibitor. However, as **Figure 3.24** shows, there is no such relationship, and therefore the observed enantioselectivity is not driven by preference for the M-configuration alone, but likely by the establishment of specific contacts with the target.

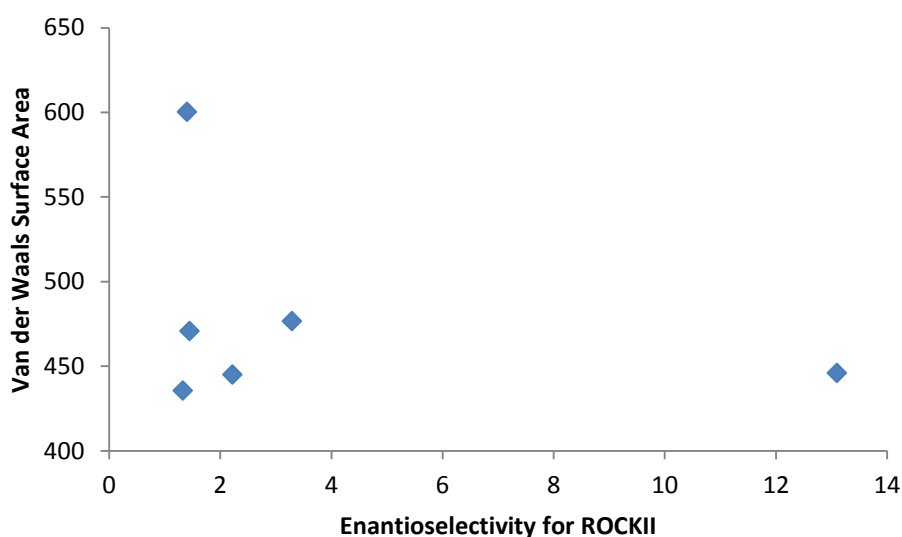


Figure 3.24. Comparison of enantioselectivity for ROCKII versus Van der Waals surface area (calculated by Maestro) for azaindole-based analogs incorporating varying substituents at A7.

Rationalizing observed selectivity among the kinome. As demonstrated in the network of kinase selectivity potential introduced in Chapter 1, the ROCK enzymes belong to a cluster of only 25 kinases (predominantly AGC kinases) which harbor a characteristic phenylalanine residue in a hydrophobic motif (HM). Contact with this residue, then, has potential to confer selectivity to an inhibitor. As shown in **Figure 3.25**, the pyridine ring of **BZD-29** makes a number of good contacts with this residue in

ROCKII (Phe384); these contacts are mirrored by **BZD-29** in ROCKI (Phe368) (not shown). This interaction may then be responsible for the selectivity of **BZD-29** for the ROCK enzymes over alternate members of the human kinome. Furthermore, because not all AGC kinases contain this hydrophobic motif selectivity feature, these contacts may also impart selectivity for ROCK's versus other members of the AGC family as well.

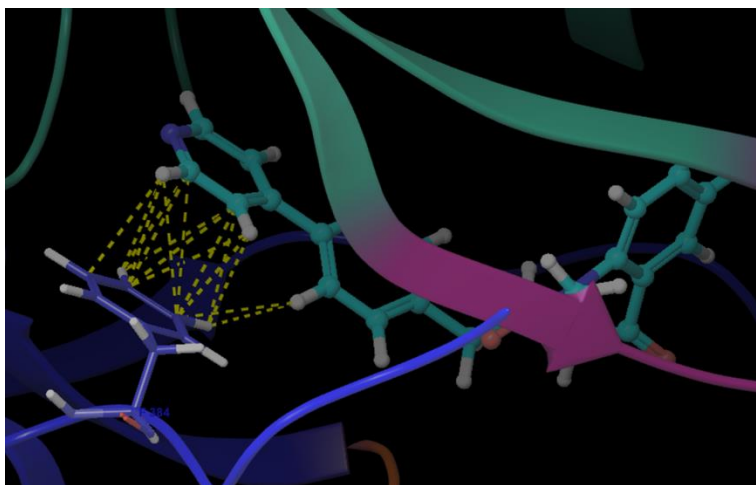


Figure 3.25. Contacts between **BZD-29** and Phe384 of ROCKII (PDB: 2F2U)⁴⁷.

Induced fit docking results suggest that the azaindole-based inhibitors also successfully make contact with this residue (**Figure 3.26**), and in fact the number of good contacts between Phe384 and the C ring is predicted to have increase. Therefore, if these contacts do confer specificity among the kinome, the current inhibitor series is expected to maintain a similar selectivity score to that observed for **BZD-29**.

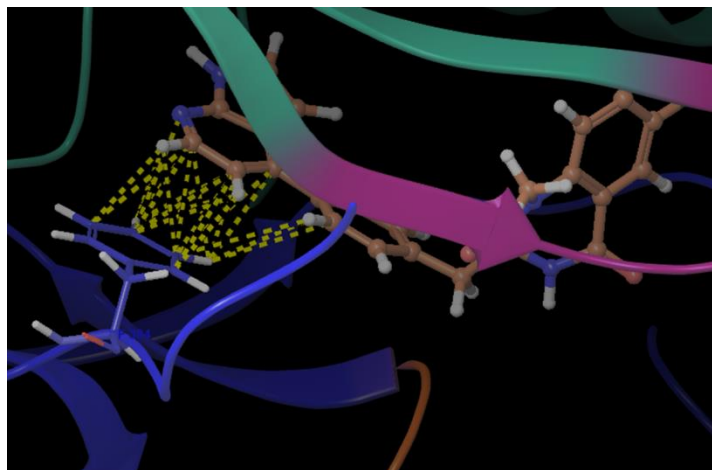


Figure 3.26. Contacts between **11** and Phe 384 of ROCKII (PDB: 2F2U)⁴⁷.

Additionally, it has been proposed by Yamaguchi et al. that contact with the conserved Leu221 residue of ROCK confers selectivity, among other AGC kinase family members such as PKA, to the well-known inhibitor Fasudil. **Figure 3.27** shows that this residue makes extensive contact with **BZD-29 (a)** as well as analog **11 (b)**. Therefore, if these contacts do indeed confer selectivity among AGC kinase family members as predicted, the new azaindole-based analog series are expected to maintain the level of selectivity observed for **BZD-29**.

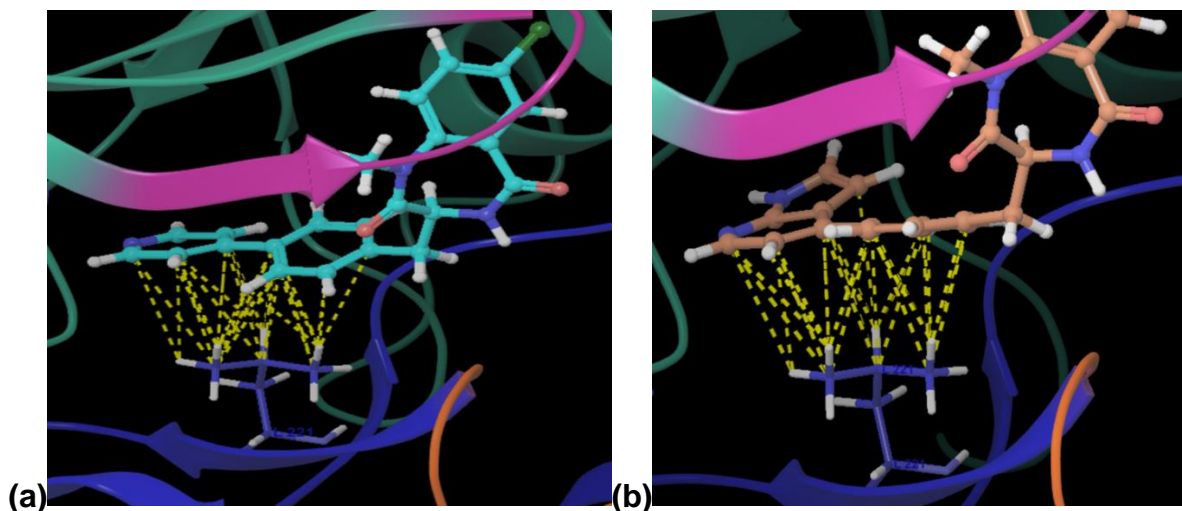


Figure 3.27. Contacts between Leu221 of ROCKII and (a) **BZD-29** or (b) compound **11** (PDB: 2F2U)⁴⁷.

To further investigate this prediction, **BZD-29** was docked into the corresponding ATP binding site of the closely related kinase PKA (**Figure 3.28**)⁵⁰. This pose was then aligned to that of **BZD-29** in ROCKII to allow a direct comparison of the conformations of this conserved Leu residue. As noted by the aforementioned authors, Met172, Leu221, and Ala231 of Rho kinase serve to form the base of the binding pocket. In PKA, these residues correspond to Val123, Leu173, and Thr183, respectively. While Leu221 of ROCK adopts a stable rotamer, protruding toward **BZD-29** to make a number of good contacts, the corresponding Leu173 of PKA is observed in a rare, unstable configuration due to side chain packing with the nonconserved Val123 and Thr183 residues. It is therefore predicted that Leu173 of PKA will make fewer favorable contacts with **BZD-29**. From the docking pose of **BZD-29** in ROCK, it even appears as if the B ring is rotated toward Leu221 in order to increase favorable contacts; this may explain the enhanced selectivity, even among the AGC kinase family, of **BZD-29** versus known ROCK inhibitors, such as Fasudil.

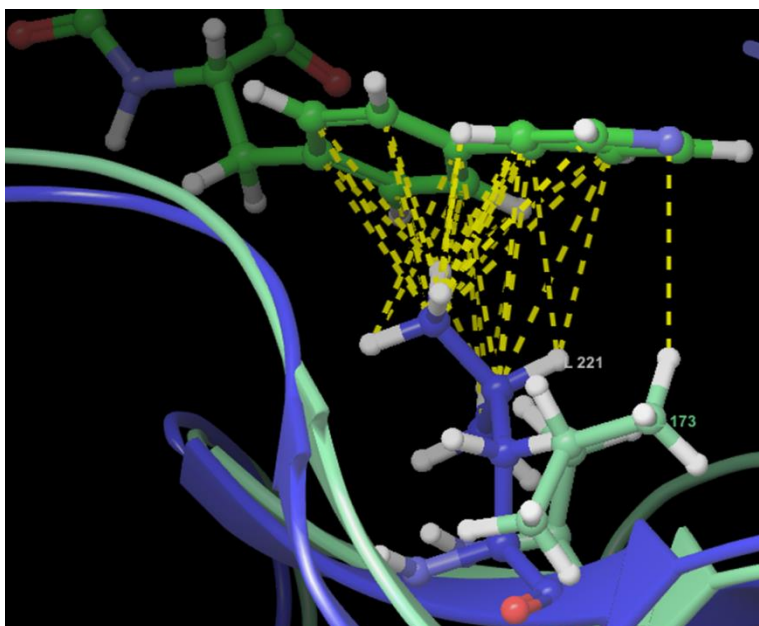


Figure 3.28. Overlay of ROCKII (blue) and PKA (green) structures from predicted binding poses with **BZD-29**; shown with good contacts (yellow hashes); (PDB: ROCKII= 2F2U, PKA= 1Q8W)^{47,50}.

For further analysis of this effect, **BZD-29** was docked into the original structure of PKA and the Glide Score of the highest ranked pose was noted (-6.623). Leu173 of PKA was then rotated until it was precisely overlaid with Leu221 of ROCK. **BZD-29** was then docked to this modified structure. The highest ranked pose resulting from this job had a Glide Score of -7.194 (the more negative the Glide Score, the more favorable the interaction). For reference, the Glide Score of **BZD-29** in ROCKII was -10.292. Therefore, although an improvement in binding of **BZD-29** to PKA was realized upon adjustment of Leu173 of PKA to mimic Leu221 of ROCKII, the difference was slight and did not result in the prediction of equipotent binding of PKA and ROCKII by **BZD-29**.

Rationalizing observed isoform selectivity. It was previously determined that **BZD-29** selectively inhibits ROCKII in cells from its ability to decrease the phosphorylation levels of a common ROCKI/II substrate (myosin light chain or MLC)

without affecting the presence of focal adhesions, known to depend solely on ROCKI for formation¹⁶. However, as shown in **Table 3.4**, **BZD-29** inhibits ROCKI and ROCKII at similar levels in the biochemical assays. Perhaps the most significant difference between the cellular assays and these biochemical assays is the ROCK construct used. As referenced previously, the biochemical assays employ constructs of only residues 1-545, of the >1300 amino acid enzyme. This region primarily incorporates the kinase domain, while lacking regions of the C-terminus, including the pleckstrin homology domain (or PH domain). Similar discordant results have previously been reported to occur in assays involving analogously truncated mutants.

In 2005, Barnett et al. identified a potent inhibitor of the Akt1 (IC_{50} = 58 nM) and Akt2 (IC_{50} = 210 nM) kinases (kinases of the same family, AGC, to which ROCKs belong) which had no inhibitory effect against mutants lacking the PH domain^{45,46}. To explain these differences, the authors proposed two models. Firstly, they considered that the contacts required for inhibitor binding may in fact lie in the PH domain itself. Secondly, they proposed that the PH domain may induce a specific conformation of the kinase domain to which the inhibitors bind. In the case of **BZD-29**, mechanism of action studies clearly demonstrated that **BZD-29** is an ATP-competitive inhibitor with respect to both ROCK enzymes. Furthermore, the biochemical assays have demonstrated that **BZD-29** retains inhibitory properties toward the PH-domain lacking ROCK mutants, albeit without the isoform selectivity observed in cellular assays. Although it remains possible that bad contact between the PH domain of ROCKI and **BZD-29** serves to specifically disallow binding, there is currently no direct evidence of this. Therefore, the first model is presently unsupported. The second model, however, appears to be

significantly bolstered by the results, in combination with current ROCK kinase literature.

Firstly, a substantial conformational shift in the kinase domain of ROCKII was observed upon induced fit docking with **BZD-29** (**Figure 3.29, a**). This was determined by performing a protein structural alignment with the unliganded ROCKII kinase domain (green) and the ROCKII kinase domain which resulted from an induced fit docking protocol (IFD) with **BZD-29** (red). Aside from the separation between the two structures which can be visualized, a global structural alignment performed by the Maestro software returned an RMSD value of 1.027 Å. This was significantly higher than the RMSD value (0.165 Å) returned for the global alignment of the unliganded ROCKI kinase (green) domain with the **BZD-29** bound ROCKI kinase domain resulting from IFD (red) (**Figure 3.29, b**), indicating that ROCKI does not experience a similar conformational change upon binding of **BZD-29**. A simple visual comparison of the two sets of superimposed structures also supports the prediction of a large conformational shift in the ROCKII kinase domain which is not observed for ROCKI.

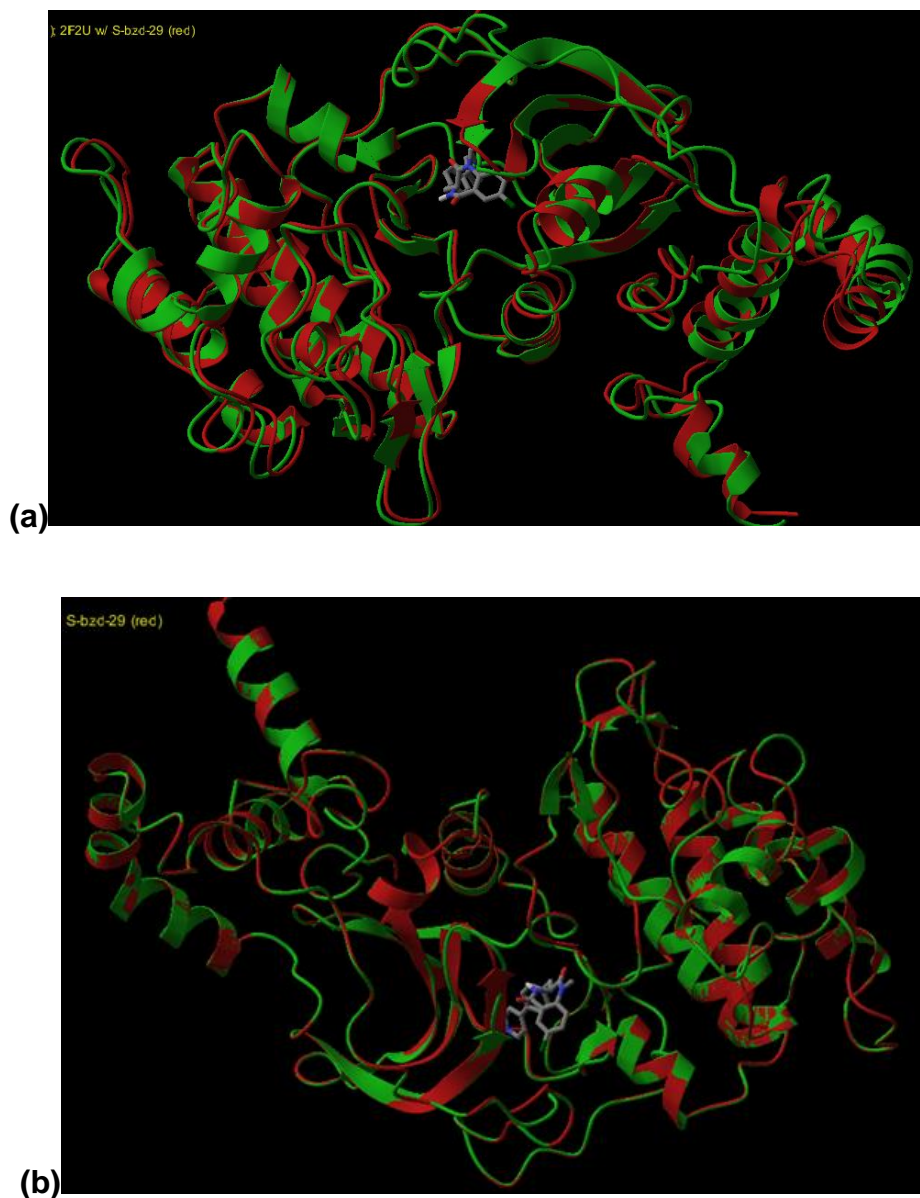


Figure 3.29. Alignments of unliganded (green) and **BZD-29**-bound (red) ROCKII (a) and ROCKI (b) kinase domains.

The kinase domain conformations of ROCKI and ROCKII produced by IFD with Fasudil were also aligned to their respective unliganded kinase domain conformations. It was visually apparent that no large conformational shift resulted in either kinase domain from binding of Fasudil, and expectedly, the RMSD's are small and approximately equivalent (0.009 Å and 0.012 Å for ROCKI and ROCKII, respectively).

These results are in agreement with the reported equipotency of Fasudil against the ROCK isoforms.

These observations support the second model proposed by Barnett et al. and suggest the mechanism for selectivity represented in **Figure 3.30**. As shown, in this model, the ROCK kinase domains adopt similar conformations when uninhibited by their respective PH domains, allowing the kinases to recognize **BZD-29** similarly, such that inhibition is equipotent. However, as **BZD-29** binds to ROCKII, a conformational change in the kinase domain is elicited which mimics that of the structure resulting from autoinhibition by the PH domain. In this manner, **BZD-29** is able to effectively inhibit the inactive (or autoinhibited) form of the protein. The enhanced potency for **BZD-29** in ROCKII versus ROCKI in cells is therefore analogous to that experienced by a type II kinase inhibitor versus a type I inhibitor. In the case of ROCKII, **BZD-29** is capable of locking the enzyme in an inactive state which cannot efficiently bind ATP; therefore, competition is averted. Also, by LeChatlier's principle, as the autoinhibited form of ROCKII is complexed with **BZD-29**, the equilibrium shifts toward this state, increasing the amount of autoinhibited ROCKII kinase which can then be efficiently inhibited by **BZD-29**.

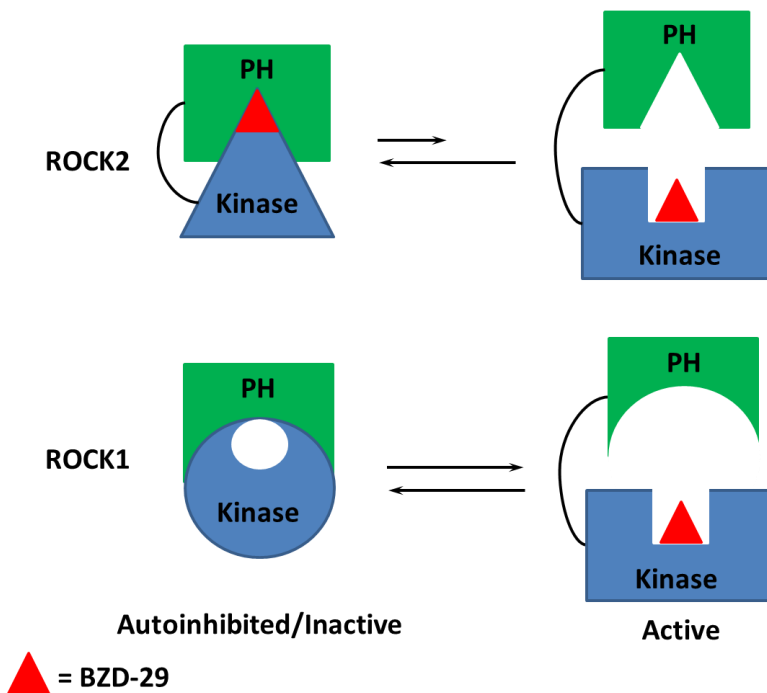


Figure 3.30. Proposed mechanism of ROCKII selectivity by **BZD-29**.

This model is supported by the current literature regarding ROCK as well. The largest distinctions between the ROCKI and ROCKII isozymes are located in the PH domains. With 65% sequence identity, these regions are the least conserved among the two enzymes. Additionally, the proteins' tertiary structures differ significantly due to non-identical amino acids within proline-containing regions of these domains, and these structural differences are what allow isoform specific activators to recognize each enzyme⁴⁷. It is reasonable to expect then that the structural differences in the PH domains may result in different recognition patterns between these regions and the kinase domain of each isoform; these differences might then be exploited by an inhibitor.

In an attempt to further understand the mechanism by which **BZD-29** elicits the observed conformational change in ROCKII, the sequences of ROCKI and ROCKII were aligned using the multiple sequence viewer tool in the Maestro software suite. The distinct residues were then highlighted (red) and the structures were overlaid to visualize the locations of unique amino acids (**Figure 3.31**). Next, the unique residue closest to the ATP binding pocket was identified as Thr365 of ROCKI, which corresponded to Ser381 of ROCKII. Ser381 of ROCKII was then mutated to a threonine residue, the protein was re-prepared, and a new induced fit docking job was conducted with **BZD-29**. The results are shown in **Figure 3.32**.

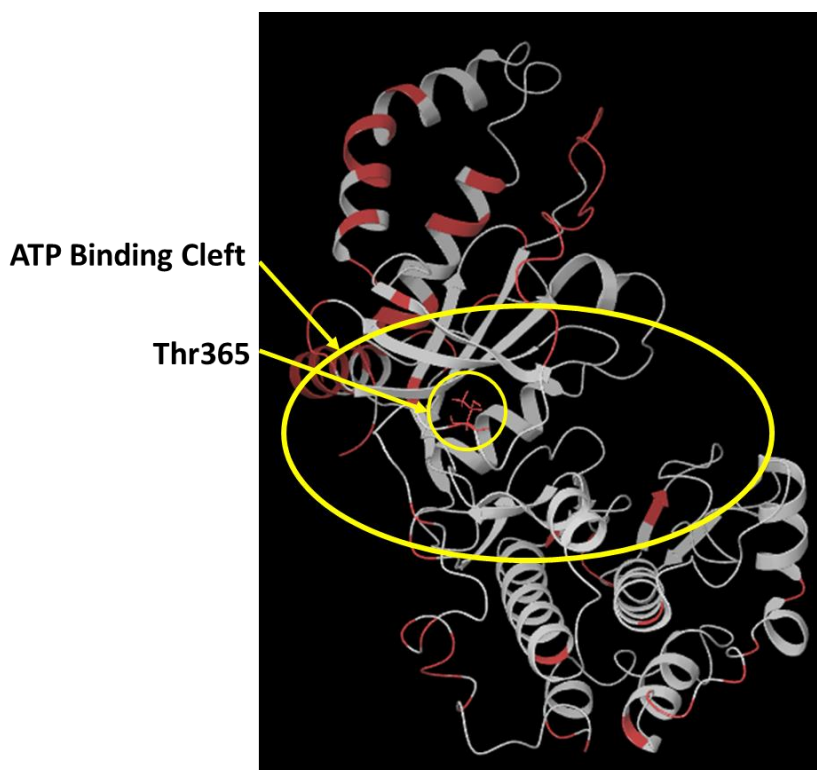


Figure 3.31. Results from overlay of ROCKI and ROCKII with unique amino acids colored red and Thr365 of ROCKI displayed.

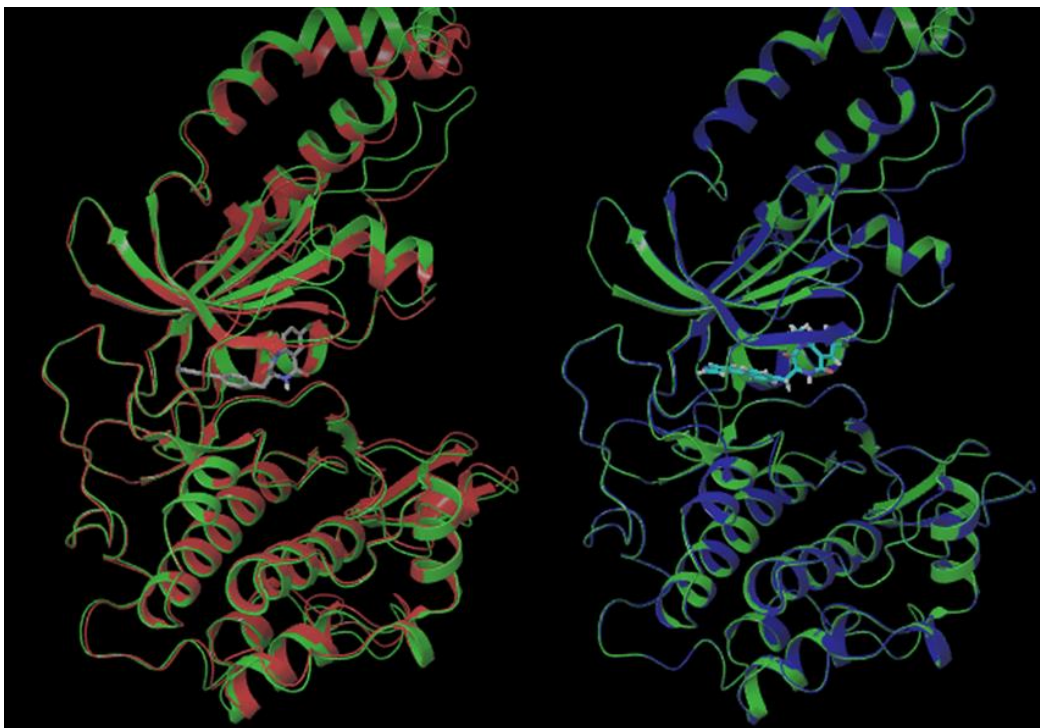


Figure 3.32. (left) Alignment of native ROCKII without ligand (green) and native ROCKII bound to **BZD-29** (red). (right) Alignment of native ROCKII without ligand (green) and the Thr381 ROCKII mutant bound to **BZD-29**.

As can be observed from **Figure 3.32** (right) the structure of mutated ROCKII in complex with **BZD-29** now aligns well with the structure of unliganded ROCKII (RMSD= 0.156 Å). These results suggest that Ser381 of ROCKII plays a crucial role in the conformational change which may allow **BZD-29** to selectively recognize ROCKII more efficiently than it recognizes ROCKI in cells. To rationalize the conformation which occurs in native ROCKII upon binding of **BZD-29**, the favorable contacts between Ser381 and other residues of the protein were determined. These residues were then compared to those which made favorable contacts with Thr365 of ROCKI. Unfortunately, all of these residues were analogous and no unique interaction was determined. Several instances of conformational differences between equivalent amino

acids did arise however, and possibly these subtle conformational distinctions combine to result in the large conformational change observed.

The observed conformational shift determined to occur upon binding of **BZD-29** to ROCKII was also predicted for the current inhibitor series (represented by analog **11**); the binding poses were aligned with an RMSD= 0.122 Å. Additionally, the binding pose of **11** in ROCKI also aligned well to that of **BZD-29** in ROCKI (RMSD= 0.09 Å). If the proposed model is correct, the current lead inhibitors are expected to retain the isoform selectivity achieved by **BZD-29**.

Material and Methods

Induced Fit Docking (IFD)

Glide Docking. The coordinates for all proteins were obtained from the Research Collaboration for Structural Bioinformatics (RCSB) Protein Data Bank (PDB). Specifically, crystal structures of the kinase domains of ROCK-II (PDB: 2F2U) and ROCK-I (PDB: 2ESM) were used.

Ligands were prepared in Maestro of the Schrodinger software with the OPLS_2005 force field. Possible ionization states were generated at pH 7.0 ± 2.0 by Epik. The ligands were then desalted to remove molecules other than the ligand and tautomers were generated where appropriate. Possible stereoisomers were generated and the number of ring conformations was set to 2 to mimic the well-documented benzodiazepine ring conformations (M and P).

Glide 5.9 was used for all docking calculations following previously described procedures^{15,20,23}. In the first stage of the induced fit protocol, minimization is performed on the receptor. Prime module of Schrodinger package performs flexible loop prediction that generates a maximum of five alternative glycine-rich loop (G99-E105) conformations of subsequent docking.

Softened-potential docking was then performed and 20 initial poses are generated for each receptor conformation. The softened-potential docking consisted

of scaling the van der Waals radii of non-polar atoms by 0.5 (for receptor atoms with partial atomic charge $q \leq 0.25e$ and for ligand atoms with $q \leq 0.15e$). Standard precision (SP) Glide scoring was used for this initial evaluation. By default, only the top ten scoring poses with Coulomb-vdW score and H-bond score less than 100 kcal/mol and 0 kcal/mol, respectively, are retained.

For each initial docking pose, receptor side-chains that are within 5.0 Å of the ligand are optimized to allow the side-chains to adopt optimal conformation to interact with the ligand. The ligand is then redocked into the induced-fit receptor and the final ligand pose is scored with Extra Precision (XP) Glide scoring function. The results are visualized with PyMOL³⁰.

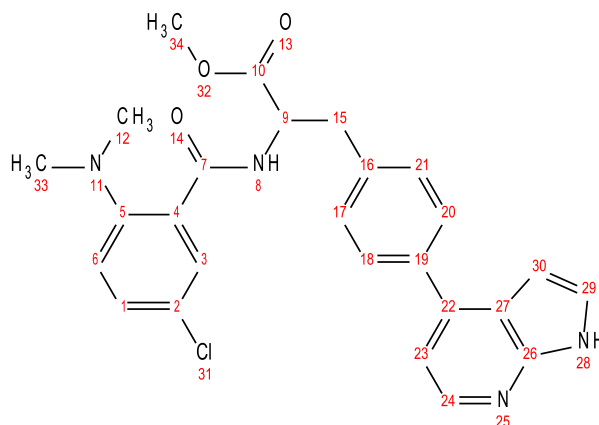
Prime Refinement. For each of the top 20 poses (with respect to Glide scores) from the initial softened-potential docking step, protein refinement was performed. Prime uses the OPLS parameter set³¹⁻³³ and a surface generalized Born implicit solvent model^{34,35}. First, a list is generated consisting of all residues having at least one atom within 5 Å of an atom in any of the 20 ligand poses. All side chains in the list underwent a conformational search and minimization³⁶.

After convergence to a low-energy solution, an additional minimization was performed allowing all residues in the list (backbone and side chain) and the ligand to be relaxed. Specifically, side-chain refinement was performed to residues within 5.0 Å of the defined loop segment. The complexes were ranked by Prime energy (molecular mechanics plus solvation), and those within 30 kcal/mol of the minimum energy structure were passed through for a final round of Glide docking and scoring.

Ligand Resampling and Final Scoring. The minimized ligand used in the first docking was redocked using Glide with default settings into each of the top receptor poses produced in the protein refinement step. A composite score that accounts for the protein/ligand interaction (Glide score) and the total energy of the system (Prime energy) was calculated using the following equation: $\text{Glide score} + 0.05 \times \text{Prime energy}$.

Chemistry

methyl-3-(4-(1H-pyrrolo[2,3-b]pyridin-4-yl)phenyl)-2-(5-chloro-2-(dimethylamino)benzamido)propanoate (**31**, LDM-3-45)



Synthesis of **31** began by coupling N-methyl isatoic anhydride (1 eq) with D- or L-iodophenylalanine (to provide the S- or R-enantiomer of the final product, respectively) (1.15 eq) in refluxing pyridine (2 mL/mmol) for 4 h. After cooling to room temperature, the solution was neutralized and extracted with ethyl acetate. The organic layer was washed with brine and dried over magnesium sulfate. After

filtration, the solvent was evaporated and the resulting residue was taken to the next step without purification.

The final material of the previous step was then treated with 2.1 eq of potassium carbonate before methylation with 1.91 eq of methyl iodide at room temperature in DMF (3 mL/mmol) at room temperature for 12 h. The solution was then poured into stirring 1N HCl and filtered. The final product was then prepared by GP6 (reagent: 4-(4,4,5,5-tetramethyl-1,3,2-dioxaborolan-2-yl)-1H-pyrrolo[2,3-b]pyridine). The resulting crude product was purified by flash chromatography [0-100%(10%MeOH/EA)/hex] to provide methyl 3-(4-(1H-pyrrolo[2,3-b]pyridin-4-yl)phenyl)-2-(5-chloro-2-(dimethylamino)benzamido)propanoate (overall yield= 16.1%) as an off-white solid; Rf= 0.30 (EA); ¹H NMR (500 MHz) (δ/ppm) 2.84 (s, 6H, 12, 33), 3.03 (ddt, 1H, J=12.4, J=7.4, J=1.0, 15), 3.32 (ddt, 1H, J=12.4, 7.5, 1.0, 15'), 3.66 (s, 3H, 34), 4.79 (t, 1H, J=7.6, 9), 6.57 (d, 1H, J=7.5, 30), 6.89 (d, 1H, J=7.5, 6), 7.34 (m, 2H, 1, 29), 7.39 (dt, 2H, J=7.4, J=1.2, 17, 21), 7.74 (m, 2H, 18, 20), 7.81 (d, 1H, J=7.5, 23), 7.96 (d, 1H, J=2.0, 3), 8.62 (d, 1H, J=7.5, 24), 10.06 (s, 1H, 8), 11.71 (s, 1H, 28); ¹³C NMR (500 MHz) (δ/ppm) 37.3, 43.2, 52.4, 53.3, 94.9, 110.5, 116.7, 119.7, 123.0, 124.5, 126.9, 128.3, 129.7, 131.6, 133.0, 133.7, 137.4, 139.8, 145.2, 147.1, 147.3, 166.9, 173.0; Exact Mass (ES): determined mass: 476.1620 u, exact mass: 476.1615 u.

References

1. Jacobs, M.; et al. The structure of dimeric ROCK I reveals the mechanism for ligand selectivity. *J Biol Chem* **2006**, *281*, 260-268.
2. Yamaguchi, H.; et al. Structural basis for induced-fit binding of Rho-kinase to the inhibitor Y-27632. *J Biochem* **2006**, *140*, 305-311.
3. Tamura, M.; et al. Development of specific Rho-kinase inhibitors and their clinical application. *Biochim Biophys Acta* **2005**, *1754*, 245-52.
4. Sessions, E.H.; et al. The development of benzimidazoles as selective rho kinase inhibitors. *Bioorg Med Chem Lett.* **2010**, *20*, 1939-1943.
5. Doe, C.; et al. Novel Rho kinase inhibitors with anti-inflammatory and vasodilatory activities. *J Pharmacol Exp Ther* **2007**, *320*, 89-98.
6. Stavenger, R.A.; et al. Discovery of aminofurazan-azabenzimidazoles as inhibitors of Rho-kinase with high kinase selectivity and antihypertensive activity. *J Med Chem* **2007**, *50*, 2-5.
7. Feng, Y.; et al. Discovery of substituted 4-(pyrazol-4-yl)-phenylbenzodioxane-2-carboxamides as potent and highly selective Rho kinase (ROCK-II) inhibitors. *J Med Chem* **2008**, *51*, 6642-6645.
8. Kitchen, D.B.; et al. Docking and scoring in virtual screening for drug discovery: methods and applications. *Nat Rev Drug Discov* **2004**, *3*, 935-49.
9. Scapin, G. Structural biology and drug discovery. *Curr Pharm Des* **2006**, *12*, 2087-97.
10. Jacobs, M.; et al. Crystal structure of Rho-kinase I kinase domain complexes and binding pockets thereof. U.S. Patent 7,655,446, February, 2009.

11. Friesner, R.A.; et al. Glide: a new approach for rapid, accurate docking and scoring. 1. Method and assessment of docking accuracy. *J Med Chem* **2004**, *47*, 1739-1749.
12. Sherman, W.; et al. Novel procedure for modeling ligand/receptor induced fit effects. *J Med Chem* **2006**, *49*, 534-553.
13. Friesner, R.A.; et al. Extra precision glide: docking and scoring incorporating a model of hydrophobic enclosure for protein-ligand complexes. *J Med Chem* **2006**, *49*, 6177-6196.
14. Gohda, K.; et al. A molecular mechanism of P-loop pliability of Rho-kinase investigated by molecular dynamic simulation. *J Comput Aided Mol Des* **2008**, *22*, 789-797.
15. Carugo, O. How root-mean-square distance (r.m.s.d) values depend on the resolution of protein structures that are compared. *J. Appl. Cryst.* **2002**, *36*, 125-128.
16. Francis, T.M. Target identification and validation of a novel family of anti-inflammatory 1,4-benzodiazepine-2,5-diones. Ph.D. Dissertation, University of Michigan, Ann Arbor, Michigan, 2010.
17. Ney, G.M. Molecular recognition of small molecules by the mitochondrial F₁F₀-ATPase. Ph.D. Dissertation, University of Michigan, Ann Arbor, Michigan, 2007.
18. Lamzin, V.S.; et al. How nature deals with stereoisomers. *Curr. Opin. Struct. Biol.* **1995**, *5*, 830.
19. Bergmann, M.; Fruton, J.S. On proteolytic enzymes. XII. Regarding the specificity of aminopeptidase and carboxypeptidase. A new type of enzyme in the intestinal tract. *J. Med. Biol. Chem.* **1937**, *117*, 189.
20. a.) Easson, L.; Stedman, E. Studies on the relationship between chemical constitution and physiological action. V. Molecular dissymmetry and physiological activity. *Biochem. J.* **1933**, *27*, 1257. b.) Ogston, A.G. Interpretation of experiments on metabolic processes, using isotopic tracer elements. *Nature.* **1948**, *163*, 963.
21. Mesecar, A.D.; Koshland, D.E., Jr. A new model for protein stereospecificity. *Nature* **2000**, *403*, 614.

22. Sundaresan, V.; Abrol, R. Biological chiral recognition: the substrate's perspective. *Chirality* **2005**, *17*, S30.
23. Bentley, R. Diastereoisomerism, contact points, and chiral selectivity: a four-site saga. *Arch. Biochem. Biophys.* **2003**, *414*, 1.
24. Verri, A.; et al. L-ATP is recognized by some cellular and vial enzymes: does chance drive enzymic enantioselectivity. *Biochem. J.* **1999**, *337*, 585.
25. Tobi, D.; Bahar, I. Structural changes involved in protein binding correlate with intrinsic motions of proteins in the unbound state. *Proc. Natl. Acad. Sci* **2005**, *102*, 18908.
26. Booth, T.D.; et al. Is chiral recognition a three-point process? *Chirality* **1997**, *9*, 96.
27. Ali, I.; et al. Role of racemization in optically active drugs development. *Chirality* **2007**, *19*, 453.
28. Pasutto, F.M. Mirror images: the analysis of pharmaceutical enantiomers. *J. Clin. Pharmacol.* **1992**, *32*, 917.
29. Crane, E.; List, A. Immunomodulatory drugs. *Cancer Invest.* **2005**, *23*, 625.
30. Friesner, R.A.; et al. Glide: a new approach for rapid, accurate docking and scoring. 1. Method and assessment of docking accuracy. *J Med Chem* **2004**, *47*, 1739-1749.
31. Halgren, T.A.; et al. Glide: a new approach for rapid, accurate docking and scoring. 2. Enrichment factors in database screening. *J Med Chem* **2004**, *47*, 1750-1759.
32. **Small-Molecule Drug Discovery Suite 2013-1**: Glide, version 5.9, Schrodinger, LLC, New York, NY, 2013.
33. The PyMOL Molecular Graphics System, Version 1.5.0.4 Schrodinger, LLC.

34. Jorgensen, W.L.M.; et al. Development and Testing of the OPLS All-Atom Force Field on Conformational Energetics and Properties of Organic Liquids. *J. Am. Chem. Soc.* **1996**, *118*, 11225-11236.
35. Kaminski, G.A.F.; et al. Evaluation and Reparametrization of the OPLS-AA Force Field for Proteins via Comparison with Accurate Quantum Chemical Calculations on Peptides. *J. Phys. Chem. B* **2001**, *105*, 6474-6487.
36. Jacobson, M.P.K.; et al. Force field validation using protein side chain prediction. *J. Phys. Chem. B* **2002**, *106*, 11673-11680.
37. Ghosh, A.R.; et al. Generalized born model based on a surface integral formulation. *J. Phys. Chem. B* **1998**, *102*, 10983-10990.
38. Gallicchio, E.; et al. The SGB/NP hydration free energy model based on the surface generalized born solvent reaction field and novel nonpolar hydration free energy estimators. *J Comput Chem* **2002**, *23*, 517-529.
39. Jacobson, M.P.; et al. On the role of the crystal environment in determining protein side-chain conformations. *J Mol Biol* **2002**, *320*, 597-608.
40. Armougom, F.; et al. The iRMSD: a local measure of sequence alignment accuracy using structural information. *Bioinformatics* **2006**, *22*, e35-39.
41. Yamaguchi, H.; et al. Molecular mechanism for the regulation of rho-kinase by dimerization and its inhibition by fasudil. *Structure* **2006**, *14*, 589-600.
42. Help, Index, & Glossary for Protein Explorer (PE). PE's Reference Manual. http://www.umass.edu/microbio/chime/pe_beta/pe/protexpl/igloss.htm (accessed August 18, 2013).
43. Jeffrey, G. *An introduction to hydrogen bonding*, 1st ed.; Oxford University Press.: Oxford, 1997.
44. Huang, D.; et al. Kinase selectivity potential for inhibitors targeting the ATP binding site: A network analysis. *Structural Bioinformatics* **2010**, *26*, 198-204.
45. Barnett, S. F.; et al. Identification and characterization of pleckstrin-homology-domain-dependent and isoenzyme-specific Akt inhibitors. *Biochemical Journal* **2005**, *385*, 399-408.

46. Sigma-Aldrich. Akt1/2 kinase inhibitor.
<http://www.sigmaaldrich.com/catalog/product/sigma/a6730?lang=en®ion=US>
(accessed August 18, 2013).
47. Yoneda, A.; et al. The Rho kinases I and II regulate different aspects of myosin II activity. *J Cell Biol* **2005**, *170*, 443-453.
48. Goodman, K.B.; et al. Development of dihydropyridone indazole amides as selective Rho-kinase inhibitors. *J Med Chem* **2007**, *50*, 6-9.
49. Meanwell, N.A.; Walker, N.A. 12.06 1,4-Diazepines. **2008** The Bristol Myers Squibb Pharmaceutical Research Institute: Wallingford, CT.
50. Breitenlechner, C.; et al. Protein kinase A in complex with Rho-kinase inhibitors Y-27632, Fasudil, and H-1152P: structural basis of selectivity. *Structure*, **2003**, *11*, 1595-1607.

Chapter 4

IMPACT OF CURRENT PROGRESS AND FUTURE DIRECTIONS

Introduction

In lead optimization, the general goals are to achieve enhanced levels of potency and efficacy against a specific target^{1,2}. Since a truly exhaustive search of chemical space is often impractical, this requires some method of prediction as to which analogs might improve binding and/or selectivity or provide the most useful information about the binding pocket and orientation of the inhibitor in it to guide future predictions. It is important, both during and after such a project, to assess the design of the venture itself, and to modify the approach to result in more accurate models if necessary. This may be accomplished by rating the models utilized as to their predictability and then using these as “parent” models from which the population can evolve through the creation of next generation, or “daughter”, models³. In this way, the quality of the population increases as the least accurate models are replaced by those which are newly developed. This chapter comprises such an assessment.

Lipophilic Efficiency (LipE). One way of gauging the quality of an inhibitor is to define its lipophilic efficiency (LipE). LipE refers to a parameter used in drug

discovery and design to evaluate research compound quality by estimating druglikeness^{4,5}. For a given compound, LipE is calculated using **Equation 4.1**, although cLogP is typically used in place of the empirical LogP values.

$$\text{LipE} = \text{pIC}_{50} - \text{LogP}$$

Equation 4.1. Calculation of lipophilic efficiency (LipE)⁶.

The value of LipE lies in its ability to express both potency (IC₅₀) and lipophilicity (LogP) in a single parameter. Because proteins are largely hydrophobic, a particularly greasy compound (one with a high LogP) might appear to bind to its target with great affinity simply due to the hydrophobic effect, where nonpolar substances tend to aggregate in aqueous solution to exclude water⁶. LipE negates this effect by penalizing compounds with especially high LogP values and allowing the highest quality inhibitors to stand out.

Enantioselectivity as a measure of interaction quality. As mentioned in Chapter 3, enantioselectivity is one way to assess the binding mode of a chiral inhibitor, although it does not appear to be necessary for the inhibition of every target. For example, anticancer screens have shown that achiral pyrimidines possess comparable activity to chiral analogs in the inhibition of tubulin polymerization⁷. However, when enantioselectivity does arise, it suggests the establishment of a high order of specific contacts between the inhibitor and the binding site⁸⁻¹⁰. Therefore, relative enantioselectivity among members of an inhibitor library targeting an apparently enantioselective target can be used to determine whether the improvement or failure of a specific inhibitor was due to the establishment or loss of a specific contact rather than

a change in its general relationship to the environment of the binding site. Due to the recognition that ROCKII appears to be enantioselective with regards to the current inhibitor series, this feature was used to assess inhibitor quality. Essentially, a higher quality compound should experience a higher degree of enantioselectivity, as a greater number of specific contacts arranged in such a precise manner as to optimally interact with the target should improve selectivity over alternative targets.

Assessment of the computational workflows. The computational methods were analyzed with respect to the biochemical effects produced by the compounds which they predicted. Here, the Glide Scores of the compounds predicted by the computational workflows were compared to their corresponding relative IC₅₀ values. GlideScore is a proprietary ligand scoring function which combines a set of terms describing a molecule and uses these as the basis of a binding affinity prediction. The formula for GlideScore is shown below in **Equation 4.2**^{11,12}.

$$\text{GScore} = 0.05 \cdot \text{vdW} + 0.15 \cdot \text{Coul} + \text{Lipo} + \text{Hbond} + \text{Metal} + \text{Rewards} + \text{RotB} + \text{Site}.$$

Equation 4.2. The equation of the GlideScore scoring function; vdW: Van der Waals energy, Coul: Coulomb energy, Lipo: lipophilic term from hydrophobic grid potential, Hbond: hydrogen-bonding term, Metal: metal-binding term, Rewards: rewards or penalties for different features (buried polar groups, hydrophobic enclosure, amide twists, etc.), RotB: penalty for freezing rotatable bonds, Site: polar interactions in the active site^{11,12}.

RESULTS AND DISCUSSION

Progress of the inhibitor series as represented by lipophilic efficiency. In addition to being the most potent analogs, compounds **(S)-21** and **(S)-30** also represent the most lipophilically efficient and, thus, the highest quality compounds. The chart below shows the lipophilic efficiency values, with respect to ROCKII, of the previously analyzed **BZD** library members, the current analog series represented in this thesis, and the known inhibitors Fasudil, SR3677, and Y-27632 (**Figure 4.1**)¹³⁻¹⁶. Although no inhibitors so far meet the suggested LipE >6 for quality drug candidates, it is clear that the current analog series has significantly improved LipE values versus the previous **BZD** analogs^{4,5,17}. The current inhibitors with LipE values > 4 for ROCKII represent **(S)-21** (4.44), **(S)-22** (4.56), **(R)-25** (4.12), and **(S)-30** (4.12). Additionally, these compounds have similar lipophilic efficiencies to an established ROCK inhibitor, Y-27632. The current series thus represents a significant improvement of this inhibitor class.

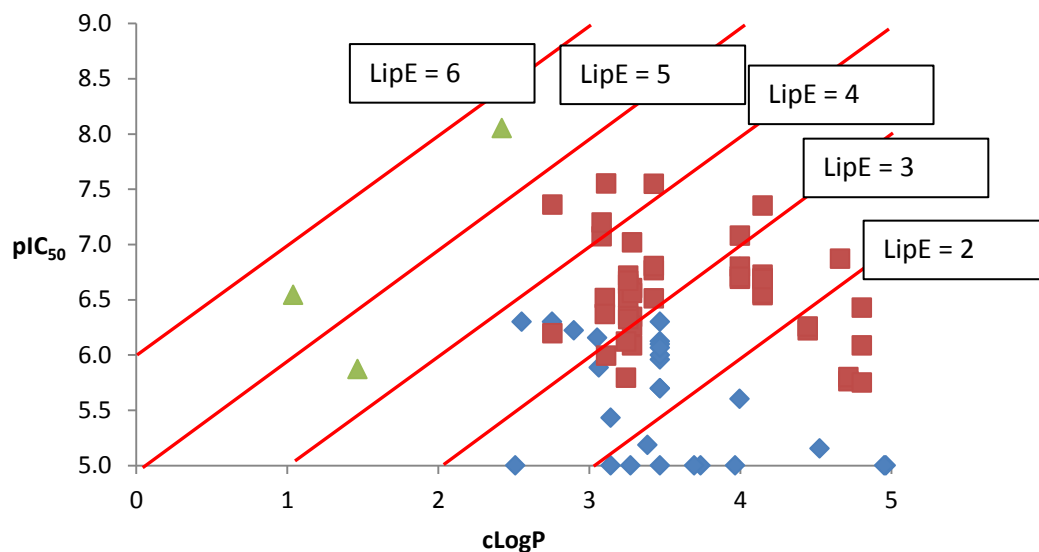


Figure 4.1. Comparisons of lipophilic efficiency (LipE) values of inhibitors with respect to ROCKII. Blue diamonds: the previous **BZD** inhibitor series, red squares: the current inhibitor series, green triangles: known ROCK inhibitors (Fasudil, SR3677, and Y-27632)¹³⁻¹⁶

Enantioselectivity of the current inhibitor series. It was noted that all compounds with ROCKII IC₅₀ values > 50x, relative to **BZD-29**, including (**S**)-**21**, (**S**)-**22**, (**S**)-**29**, and (**S**)-**30**, were significantly enantioselective for ROCKII as well; this indicates a requirement for enantioselectivity to improve activity to this degree. A linear relationship between inhibitory properties and enantioselectivity was not established however. A basic review of the data did highlight a general preference for the *S* enantiomer, and, as explored in Chapter 3, this was not simply a result of inhibitor conformation preference, but apparently an indication of a preferred orientation for the optimal arrangement of contacts with the target.

Assessment of the prediction quality of the computational workflows. In the course of the current project, two computational methods were applied (Computational Workflow A and B, described in Chapter 3). To determine the predictability of the results of the biochemical assays for the current analog series, the Glide Score of each compound designed by computational methods was compared to its relative IC₅₀ value (with respect to the IC₅₀ of **BZD-29**) for ROCKII (**Figure 4.2**).

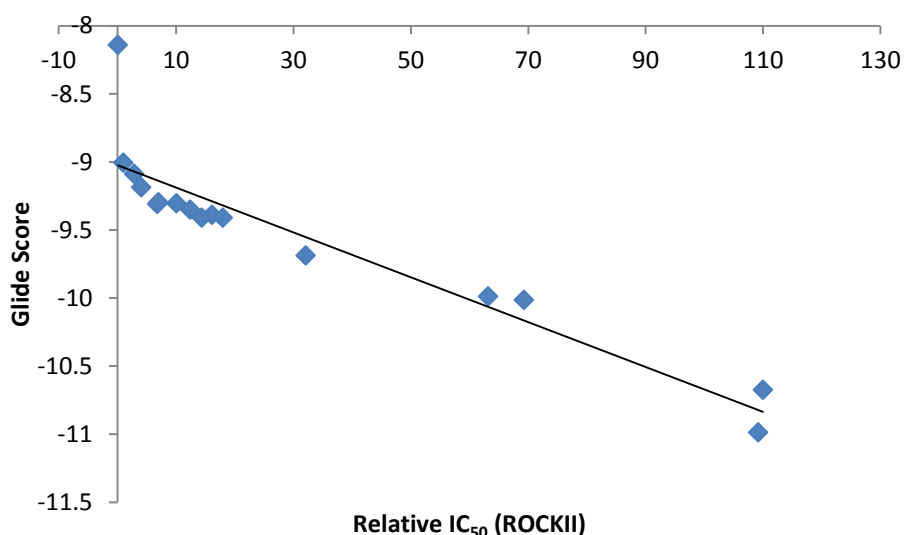


Figure 4.2. Relative IC₅₀ values (with respect to **BZD-29**) for ROCKII compared to the GlideScores of compounds designed by Computational Workflows A and B. $R^2=0.8469$, indicating that the data is well correlated.

From the R^2 value of > 0.8 , it is evident that these values are well correlated and, thus, Glide Score accurately predicted the relative binding affinity of this series of analogs. Therefore, these methods have been highly successful, especially considering that 14 out of the 16 compounds predicted from these approaches experienced significantly improved potency over **BZD-29** (defined as a relative IC₅₀ $>4x$).

Perspective of current progress and future directions. Currently, the most potent and most lipophilically efficient analogs, **(S)-22**, **(S)-30**, and **(S)-21** represent a 63x, 110x, and 109x improvement over **BZD-29**, respectively. The binding poses of these analogs indicates their similarity in orientation and suggests an analog including the correct arrangement of some combination of these substitutions, or electronic representations thereof, may improve affinity further (**Figure 4.3**).

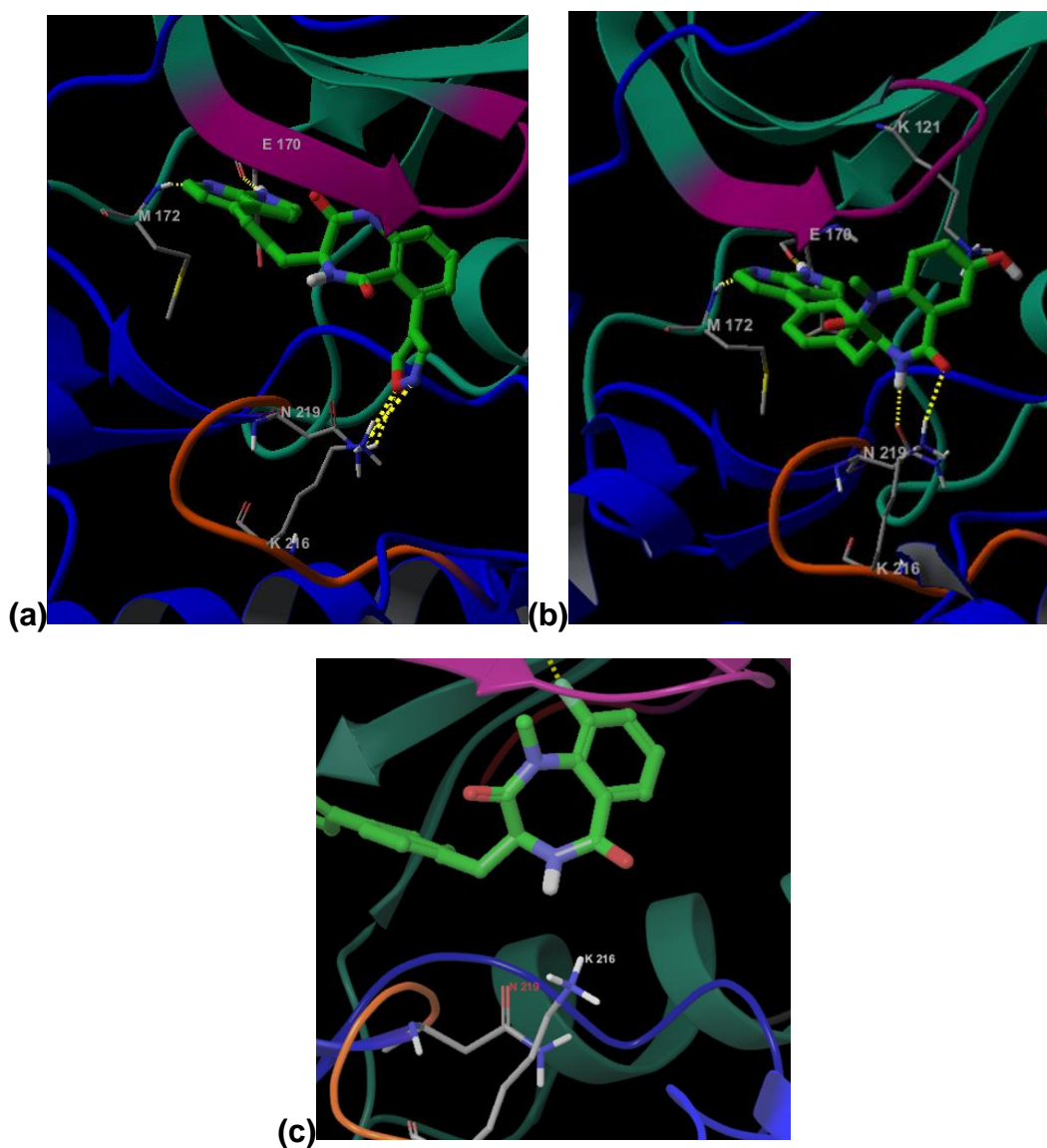


Figure 4.3. Binding poses of (a) **(S)-21**, (b) **(S)-22**, and (c) **(S)-30** in the ATP binding cleft of ROCKII.

One example of an examination of the proper placement of multiple substituents might begin with a comparison of the binding poses of **Figure 4.3**. Specifically, the contact between the **(S)-30** 9-fluorine substituent and Glu105 shifts the benzodiazepine ring toward the N-terminal lobe such that contacts with Asp219 and Lys216, made by **(S)-21** and **(S)-22 (Figure 4.3 (a) and (b))**, respectively) are no longer possible. By extending the 6-isoxazole substituent of **(S)-21** from the **(S)-30** scaffold (possibly with the inclusion of a linker if necessary), contacts with Asp219 and Lys216 might be restored while allowing the halogen bond between 9-fluorine and Glu105 to remain intact. In this manner, iterations of such substituents might be used to design future analogs for the improvement of potency and specific contacts.

The manual Hansch analysis, conducted in Chapter 2, has also provided fingerprints of the physicochemical properties of these inhibitors which confer potent inhibition and/or some degree of selectivity. As the number of azaindole-based analogs increases, it will be possible to apply quantitative SAR models (QSAR models) to this series since such models require larger analog populations than does the manual Hansch analysis^{18,19}.

The observation of PH-domain dependent ROCK isoform selectivity may point to a unique inhibitory mechanism to be exploited. As demonstrated by type II kinase inhibitors, the ability to block a kinase from entering an activated state has the potential to vastly improve the quality of inhibitors and, thus, increase the likelihood of the development of a clinical therapeutic. Firstly, the potency of such an inhibitor should be enhanced by the avoidance of competition with the high cellular concentration of ATP

(~1-10 mM)²⁰. Additionally, this inactive state may reveal additional binding sites, analogous to the allosteric site revealed during the inactive state of some kinases²¹. Essentially, no site of a kinase is more highly conserved than that of the ATP binding site due to its need to recognize a substrate (ATP) common to all kinases. Therefore, an alternative binding site should be less conserved, increasing the potential for an inhibitor to gain selectivity through interaction. Because Ser381 of ROCKII is predicted to be critically important to the selectivity for ROCKII by this inhibitor series, once a cellular isoform selectivity assay is available, it would be especially interesting to compare the selectivity of **BZD-29** for native ROCKII versus ROCKI with that of **BZD-29** for a Thr381 ROCKII mutant versus ROCKI. If this residue is in fact crucial to the optimal conformation of **BZD-29**, a high degree of selectivity should be observed for native ROCKII over ROCKI while equipotency would be expected against the ROCKII mutant compared to ROCKI.

The conformational change elicited in ROCKII, but not in ROCKI, through binding of **BZD-29** allows for comparison with the conformational effects induced by potential analogs. Unfortunately, without knowing the exact source of this transformation, the prediction of selective compounds must rely solely on the alignment of the conformation induced by **BZD-29** with the conformations which result from docking prospective analogs. An establishment of an RMSD cutoff will be necessary to define the limits of relatively good, acceptable, and poor alignments to predict the level of selectivity which might be experienced. However, once a cellular based ROCK isoform selectivity assay is available, the compounds of the current analog series may be assayed and their

results could then be compared to these RMSD values. The accuracy of this predictive method could then be determined.

In addition to binding affinity predictions, the docking results from the computational work, combined with existing ROCK literature, suggests that the current analog series should retain selectivity similar to that of **BZD-29** among the kinome as well as among the ROCK isoforms themselves. Due to its clinical success with minimal side effects reported, Fasudil has validated the Rho kinases as viable targets in the treatment of disease²². The most potent current inhibitor, **(S)-21** is > 10x more potent for ROCKII compared to Fasudil. Considering that the most successful recent analogs have IC₅₀'s near the "wall" of the currently employed biochemical assay (discussed in Chapter 2), the majority of future efforts will focus on enhancement of selectivity features of these inhibitors²³. These efforts will not only improve the quality of this inhibitor series, but with the current lack of quantitative information regarding isoform selectivity and the widespread problems of off-target binding which plague many kinase inhibitor projects, they will also aid in filling the gaps of current understanding of how different kinases are selectively modulated and how these specific differences may be exploited for inhibition of aberrant activation in human disease.

References

1. Keseru, G.M.; et al. Hit discovery and hit-to-lead approaches. *Drug Discov Today* **2006**, *11*, 741-748.
2. Bleicher, K.H.; et al. Hit and lead generation: beyond high-throughput screening. *Nat Rev Drug Discov* **2003**, *2*, 369-378.
3. Tsafnat, G; et al. Computational reasoning across multiple models. *J Am Med Inform Assoc* **2009**, *16*, 768-774.
4. Edwards, M.P.; Price, D.A. Role of physicochemical properties and ligand lipophilic efficiency in addressing drug safety risks. *Annual Reports in Medicinal Chemistry* **2010**, *45*, 381-391.
5. Leeson, P.D.; Springthorpe, B. The influence of drug-like concepts on decision-making in medicinal chemistry. *Nat Rev Drug Discov*. **2007**, *6*, 881-90.
6. Perola, E. An analysis of the binding efficiencies of drugs and their leads in successful drug discovery programs. *J Med Chem* **2010**, *53*, 2986-2997.
7. Zhang, N.; et al. Synthesis and SAR of [1,2,4]triazolo[1,5-a]pyrimidines, a class of anticancer agents with a unique mechanism of tubulin inhibition. *J. Med. Chem.* **2007**, *50*, 625.
8. Lamzin, V.S.; et al. How nature deals with stereoisomers. *Curr. Opin. Struct. Biol.* **1995**, *5*, 830.
9. Bergmann, M.; Fruton, J.S. On proteolytic enzymes. XII. Regarding the specificity of aminopeptidase and carboxypeptidase. A new type of enzyme in the intestinal tract. *J. Med. Biol. Chem.* **1937**, *117*, 189.

10. Mesecar, A.D.; Koshland, D.E., Jr. A new model for protein stereospecificity. *Nature* **2000**, *403*, 614.
11. Friesner, R.A.; et al. Glide: A New Approach for Rapid, Accurate Docking and Scoring. 1. Method and Assessment of Docking Accuracy. *J. Med. Chem.* **2004**, *47*, 1739-1749.
12. Halgren, T.A.; et al. Glide: A New Approach for Rapid, Accurate Docking and Scoring. 2. Enrichment Factors in Database Screening. *J. Med. Chem.* **2004**, *47*, 1750-1759.
13. Francis, T.M. Target identification and validation of a novel family of anti-inflammatory 1,4-benzodiazepine-2,5-diones. Ph.D. Dissertation, University of Michigan, Ann Arbor, Michigan, 2010.
14. Uehata, M.; et al. Calcium sensitization of smooth muscle mediated by a Rho-associated protein kinase in hypertension. *Nature* **1997**, *389*, 990-994.
15. Doe, C.; et al. Novel Rho kinase inhibitors with anti-inflammatory and vasodilatory activities. *J Pharmacol Exp Ther* **2007**, *320*, 89-98.
16. Feng, Y.; et al. Discovery of substituted 4-(pyrazol-4-yl)-phenylbenzodioxane-2-carboxamides as potent and highly selective Rho kinase (ROCK-II) inhibitors. *J Med Chem* **2008**, *51*, 6642-6645.
17. Ryckmans, T.; et al. Rapid assessment of a novel series of selective CB(2) agonists using parallel synthesis protocols: A Lipophilic Efficiency (LipE) analysis. *Bioorg Med Chem Lett* **2009**, *19*, 4406-4409.
18. Nantasenamat, C.; et al. A practical overview of quantitative structure-activity relationship. *Excli J* **2009**, *8*, 74-88.
19. Nantasenamat, C.; et al. Advances in computational methods to predict the biological activity of compounds. *Expert Opin Drug Discov* **2010**, *5*, 633-654.

20. Beis, I.; Newsholme, E.A. The Contents of Adenine Nucleotides, Phosphagens and Some Glycolytic Intermediates in Resting Muscles from Vertebrates and Invertebrates. *Biochemical Journal* **1975**, *152*, 23-32.
21. Mol, C.D.; et al. Structural basis for the autoinhibition and STI-571 inhibition of c-Kit Tyrosine kinase. *J Biol Chem* **2004**, *279*, 31655-31663.
22. Mueller, B.K.; et al. Rho kinase, a promising drug target for neurological disorders. *Nat Rev Drug Discov* **2005**, *4*, 387-398.
23. Klebl, B.; et al. Protein Kinases as Drug Targets. WILEY-VCH Verlag GmbH & Co.: Weinheim, 2011.